UNIVERSITY OF ALBERTA

Fiber Optic Transmission Using Optical Time Division Multiplexing

BY

© KENNETH ROBERT BENTERUD

A thesis submitted to the Faculty of Graduate Studies and Research in partial fulfillment of the requirements for the degree of **Master of Science**.

DEPARTMENT OF ELECTRICAL ENGINEERING

Edmonton, Alberta

Fall, 1993

National Library
of Canada

Acquisitions and
Bibliographic Services Branch

395 Wellington Street
Ottawa, Ontario
K1A 0N4

Bibliothèque nationale
du Canada

Direction des acquisitions et
des services bibliographiques

395, rue Wellington
Ottawa (Ontario)
K1A 0N4

Your file Votre référence

Our file Notre référence

The author has granted an irrevocable non-exclusive licence allowing the National Library of Canada to reproduce, loan, distribute or sell copies of his/her thesis by any means and in any form or format, making this thesis available to interested persons.

L'auteur a accordé une licence irrévocable et non exclusive permettant à la Bibliothèque nationale du Canada de reproduire, prêter, distribuer ou vendre des copies de sa thèse de quelque manière et sous quelque forme que ce soit pour mettre des exemplaires de cette thèse à la disposition des personnes intéressées.

The author retains ownership of the copyright in his/her thesis. Neither the thesis nor substantial extracts from it may be printed or otherwise reproduced without his/her permission.

L'auteur conserve la propriété du droit d'auteur qui protège sa thèse. Ni la thèse ni des extraits substantiels de celle-ci ne doivent être imprimés ou autrement reproduits sans son autorisation.

ISBN 0-315-88039-2

Canada

UNIVERSITY OF ALBERTA

RELEASE FORM

NAME OF AUTHOR:	**Kenneth Robert Benterud**
TITLE OF THESIS:	**Fiber Optic Transmission Using Optical Time Division Multiplexing**
DEGREE:	**Master of Science**
YEAR THIS DEGREE GRANTED:	**Fall, 1993**

Permission is hereby granted to the University of Alberta Library to reproduce single copies of this thesis and to lend or sell such copies for private, scholarly or scientific research purposes only.

The author reserves all other publication and other rights in association with the copyright in the thesis, and except as hereinbefore provided neither the thesis nor any substantial portion thereof may be printed or otherwise reproduced in any material form without the author's written permission.

Ken Benterud

4411-115 Street

Edmonton, Alberta, Canada

T6J 1P5

DATE: July 30, 1993

UNIVERSITY OF ALBERTA

FACULTY OF GRADUATE STUDIES AND RESEARCH

The undersigned certify that they have read, and recommend to the Faculty of Graduate Studies for acceptance, a thesis entitled **Fiber Optic Transmission Using Optical Time Division Multiplexing** submitted by **KENNETH ROBERT BENTERUD** in partial fulfillment of the requirements for the degree of **MASTER OF SCIENCE** in Electrical Engineering.

Dr. J. Conradi, Supervisor

Dr. R.I. MacDonald, Internal

Prof. U. Maydell, External

July 20, 1993

Dedication

To my parents, Ray and Julie,

who have provided constant support and always

encouraged me to do my best.

Abstract

This thesis presents simulation and experimental studies examining the performance of a 10 Gb/s optical time division multiplexing (OTDM) system. The theoretical aspects of optical switching are presented first, along with some consideration of multiple device integration issues. A computer model of the OTDM system is presented, and simulations using the model are analyzed. The OTDM experimental work conducted at TR Labs is reviewed and compared to the simulation results when possible. Finally, opportunities for improvements to the existing computer model and experimental systems are considered, and future directions for related research are discussed.

Acknowledgements

I would first like to thank my supervisor Dr. Jan Conradi for providing an excellent research environment for me at TR Labs. Completion of this work would not have been possible without his support in terms of both resources and time. His commitment to establishing a state of the art fiber research program is tremendous, and I consider it an honor and a privilege to have worked with such a dedicated individual.

I also would like acknowledge Dr. Ian MacDonald for his contributions in developing the Optical Time Division Multiplexing concept, and for his assistance during this project.

I thank the support staff and the other students at TR Labs for making my time here enjoyable and productive. Particularly I would like to recognize Dave Clegg, Jim Freeman, Terrance Rosadiuk, Greg May, Dave Moore, and Dave Vincent of Hewlett Packard for their assistance.

I would like to acknowledge the financial contributions by TR Labs, the University of Alberta, the Government of Alberta, and the National Science and Engineering Research Council which supported me during this work.

I also congratulate the University of Alberta, the Government of Alberta, and the industry sponsors for proceeding with a bold experiment in founding TR Labs six years ago. Investing in future technology is imperative if our province and our country as a whole are going to be competitive in global markets.

Finally, I would again like to thank my parents for their support, and especially for feeding me during the last stages of this work, when I had no time to do so on my own.

Table of Contents

1.0 Introduction 1

1.1 OTDM Overview 3

2.0 Electro-optic Switch and Modulator Theory 10

2.1 Electro-optic Devices in Lithium Niobate 10

2.2 Electro-optic Modulators 11

2.2.1 The Mach-Zehnder Interferometer 11

2.2.1.1 Interferometer Switching Voltage Calculation 12

2.2.1.2 Interferometer Bandwidth 16

2.2.1.3 Residual Phase Modulation in Interferometers 21

2.2.2 The Directional Coupler 23

2.2.3 The Mode Confinement or Cutoff Modulator 26

2.2.4 Modulator Selection for the OTDM System 27

2.3 Electro-optic Switches 29

2.3.1 The Balanced Bridge Interferometer 29

2.3.2 The Directional Coupler Switch 31

2.3.3 The Digital Switch 31

2.3.4 Switch Selection for the OTDM System 33

2.4 Integration Issues 34

2.4.1 An Example Integrated Substrate Layout 36

2.5 Summary 39

3.0 OTDM System Computer Simulations 40

3.1 Modelling Theory 40

3.1.1 Switch and Modulator Models 43

3.1.2 OTDM Transmitter Model 45
3.1.3 OTDM Receiver Model 45
3.1.4 Fiber Model 46
3.1.5 OTDM Link Model 49
3.2 Four Channel Transmitter Simulation Overview 50
3.3 Extinction Ratio Simulations 59
3.4 OTDM Simulations With Fiber Dispersion 61
3.5 OTDM System Operation Using $2V_\pi$ Switching 63
3.6 Summary 66

4.0 OTDM Experimental Setup and Component Analysis 68
4.1 Selecting the OTDM Implementation 68
4.2 OTDM Implementation Overview 69
4.3 Optical Source Characteristics 70
4.3.1 Laser Relative Intensity Noise Measurement 71
4.3.2 Laser Linewidth Measurement 73
4.4 OTDM Transmitter 77
4.4.1 Polarization Controller 78
4.4.2 Modulator and Switch Characteristics 78
4.4.2.1 Switch and Modulator Selection 78
4.4.2.2 DC Characteristics 81
4.4.2.3 RF Characteristics 82
4.4.2.4 Switch Chirp 86
4.4.3 Multiplexing Optical Signals 90
4.4.3.1 Variable Optical Delay 90
4.4.3.2 Coherence Problems 91
4.4.4 OTDM High Speed Electronics 96

4.4.4.1 Clock Filter 96
4.4.4.2 Delay Adjustment 96
4.4.4.3 Amplitude Adjustment 97
4.5 Fiber Characteristics 99
4.6 Receiver Characteristics 100
4.6.1 OTDM Receiver 100
4.6.2 Receiver Lightwave Converter 101
4.6.2.1 Erbium-Doped Fiber Amplifier 102
4.6.2.2 Optical Bandpass Filter 106
4.6.2.3 Photodetector Characteristics 107
4.6.2.4 Data Amplifier 112
4.6.2.5 Noise Limiting Lowpass Filter 113
4.6.2.6 Receiver Noise Considerations 116
4.7 Summary 122

5.0 OTDM System Experimental Results 123
5.1 Demonstrating the OTDM Concept 123
5.2 Two Channel OTDM Results 124
5.2.1 Transmitter Layout and Pulse Shapes 125
5.2.2 Receiver Layout and Pulse Shapes 132
5.2.3 Two Channel OTDM Bit Error Rate Measurements 135
5.3 Three Channel OTDM–Multiplexing Adjacent Channels 138
5.3.1 Transmitter Layout and Pulse Shapes 138
5.3.2 Receiver Layout and Pulse Shapes 141
5.3.3 Three Channel OTDM Bit Error Rate Measurements 143
5.4 Polarization Multiplexing of Adjacent Channels 145
5.4.1 Transmitter Configuration and Pulse Shapes 146

5.4.2 Receiver Configuration and Pulse Shapes 149
5.4.3 PDM Three Channel Bit Error Rate Measurements 152
5.4.4 Polarization Multiplexing Transmission Experiments 153
5.4.4.1 Transmission Experiments 154
5.4.4.2 Polarization Drift 156
5.4.4.3 Signal Spectral Properties Revisited 157
5.5 Summary 160

6.0 Summary and Conclusions 162
6.1 System Improvements 164
6.2 Further Work 165

References 168
Appendix 3A: BOSS Module Block Diagrams 172
Appendix 3B: Listing 3B.1 - Electro-optic Switch Frequency Response Calculation 'C' Code 177
Appendix 3C: Listing 3C.1 - Fiber Dispersion Calculation 'C' Code 180
Appendix 3D: Derivation of the Power Spectral Density of a Finite Length Pseudo-Random Binary Sequence 183
Appendix 4A: The Polarization Controller 185
Appendix 4B: Modulator and Switch Test Data 186
Appendix 5A: Erbium-Doped Fiber Amplifier Configurations 193
Appendix 5B: Polarization Multiplexing Transmission Experiments - Bit Error Rate Curves 194

List of Tables

Table 3.1 : Extinction Ratio Impact on OTDM Eye Closure 60

Table 3.2 : Dispersion Impact on OTDM Eye Closure 61

Table 4.1 : ETEK and UTP DC Performance Data 81

Table 5A.1 : Optical Bandpass Filter Parameters 193

Table 5A.2 : EDFA Operating Conditions 193

List of Figures

Figure 1.1 : Wavelength Division Multiplexed Transmission System 2

Figure 1.2 : Transmitter Block Diagram 4

Figure 1.3 : Receiver Block Diagram 6

Figure 2.1 : Z-Cut Mach-Zehnder Interferometer 12

Figure 2.2a : Lumped Element Electrode Structure 16

Figure 2.2b : Travelling Wave Electrode Structure 16

Figure 2.3 : Modulator Frequency Response 21

Figure 2.4 : Mach-Zehnder Interferometer 21

Figure 2.5 : Directional Coupler 23

Figure 2.6 : Mode Confinement Modulator 26

Figure 2.7 : Balanced Bridge Interferometer 29

Figure 2.8 : Digital Switch 32

Figure 2.9 : Example Integrated OTDM Transmitter Substrate Spacing Requirements .. 38

Figure 3.1 : Transmitter Block Diagram 41

Figure 3.2 : Receiver Block Diagram 42

Figure 3.3 : Simulated Waveform {i1} 51

Figure 3.4 : Simulated Waveforms {i2a} and {i2b} 51

Figure 3.5 : Simulated Waveform {i3a} 52

Figure 3.6 : Simulated Waveforms {i3a}, {i3b}, {i3c}, and {i3d} 52

Figure 3.7a : Simulated Waveform {v3a} 53

Figure 3.7b : Power Spectrum {v3a} 53

Figure 3.8 : Simulated Waveform {v3b} 55

Figure 3.9 : Simulated Waveform {v3c} 55

Figure 3.10 : Simulated Waveform {v3d} 56

Figure 3.11 : Simulated Waveforms {o3a}, {o3b}, {o3c}, and {o3d} 56
Figure 3.12 : Simulated Waveforms {o4a} and {o4b} 57
Figure 3.13 : Simulated Waveform {o5} 57
Figure 3.14 : Simulated Waveform {o5} 58
Figure 3.15 : Simulated Eye Diagram {o5} 58
Figure 3.16 : Power Spectrum {o5} 59
Figure 3.17 : Eye Diagram vs. Extinction Ratio 60
Figure 3.18a : 0 km Eye 62
Figure 3.18b : 20 km Eye 62
Figure 3.18c : 40 km Eye 62
Figure 3.18d : 60 km Eye 62
Figure 3.18e : 80 km Eye 62
Figure 3.18f : 100 km Eye 62
Figure 3.19 : Simulated 2 V_π Drive Signal {v1} 64
Figure 3.20 : Simulated Waveforms {i2a} and {i2b} 64
Figure 3.21 : Simulated 2 V_π Drive Signal {v5} 65
Figure 3.22 : Simulated Waveform {o5} 65
Figure 3.23 : Simulated Eye Diagram {o5} 66

Figure 4.1 : OTDM Experimental System Block Diagram 70
Figure 4.2 : CW Light Source Components 71
Figure 4.3 : Laser Relative Intensity Noise 72
Figure 4.4 : DSH Experimental Setup 74
Figure 4.5 : DSH Baseband Beat Spectrum 75
Figure 4.6 : Fujitsu DSH Baseband Beat Spectrum 76
Figure 4.7 : OTDM Transmitter 77
Figure 4.8 : ETEK 2 X 2 Switch Configuration 80

Figure 4.9 : UTP 1 X 2 Modulator Configuration 81
Figure 4.10 : Experimental Setup for Swept Frequency Modulator and Switch Frequency Response Measurements 83
Figure 4.11 : Modulator and Switch Frequency Responses Based on Network Analyzer S_{21} Measurement 83
Figure 4.12 : Single Tone Modulator and Switch Frequency Response Experimental Setup 84
Figure 4.13a : Single Tone and Swept Frequency Modulator Response 85
Figure 4.13b : Single Tone and Swept Frequency Switch Response 85
Figure 4.14 : Switch and Modulator Chirp Experiment 87
Figure 4.15 : Single Frequency Modulated Optical Spectrum 87
Figure 4.16 : DSH Baseband Spectrum 88
Figure 4.17a : UTP Chirp Baseband Spectrum 89
Figure 4.17b : ETEK Chirp Baseband Spectrum..... 89
Figure 4.18 : Pulse Overlap (2 Bit Separation) 92
Figure 4.19 : Pulse Overlap (1 Bit Separation) 93
Figure 4.20 : Amplifier Distortion of 2.5 Gb/s Data Signal 98
Figure 4.21 : MZ Modulator Ring Reduction 99
Figure 4.22 : OTDM Receiver 101
Figure 4.23 : Receiver Lightwave Converter 102
Figure 4.24 : Erbium Doped Fiber Amplifier Configuration 103
Figure 4.25 : Detector Frequency Response Measurement Setup Using EDFA Sp-Sp Beat Noise 107
Figure 4.26 : Detector Frequency Response (EDFA Sp-Sp Beat Noise Method) 109
Figure 4.27 : Detector Frequency Response Measurement Setup Using Single Tone Modulation Technique 111
Figure 4.28 : Detector Frequency Response (Single Tone Modulation Method) 112

Figure 4.29 : SHF90P Frequency Response 113
Figure 4.30 : OTDM and Target Pulse Shapes 115
Figure 4.31 : OTDM, Receiver, and Objective Pulse Spectrums 115
Figure 4.32 : Ideal Filter and Actual Implementation 116
Figure 4.33 : Noise Levels vs. EDFA Gain 119
Figure 4.34 : Composite SNR vs. EDFA Gain 120
Figure 4.35 : Noise Levels vs. EDFA Input Power 120
Figure 4.36 : SNR vs. EDFA Input Power 121

Figure 5.1 : 2 Channel OTDM Transmitter 125
Figure 5.2 : Waveform Acquisition Equipment 126
Figure 5.3 : ETEK #3 Switch Lower Output Waveform 127
Figure 5.4 : ETEK #3 Switch Upper Output Waveform 128
Figure 5.5 : ETEK #2 Switch Upper Output Waveform 129
Figure 5.6 : ETEK #2 Switch Lower Output Waveform 129
Figure 5.7 : UTP Modulator Eye Pattern 130
Figure 5.8 : 2 Channel Multiplexed Eye Pattern 131
Figure 5.9 : 2 Channel Receiver Configuration 132
Figure 5.10 : Received Eye Diagram–2 Channels Transmitted 133
Figure 5.11 : Received Eye Diagram–1 Channel Transmitted 134
Figure 5.12 : Filtered Eye Diagram 135
Figure 5.13 : 2 Channel OTDM Bit Error Rate Measurement Setup 135
Figure 5.14 : 2 Channel OTDM Bit Error Rate Measurements 136
Figure 5.15 : 3 Channel OTDM Transmitter Configuration 139
Figure 5.16 : 3 Channel Multiplexed Eye Pattern 140
Figure 5.17 : 3 Channel Receiver Configuration 141
Figure 5.18 : Received Eye Diagram–3 Channels Transmitted 142

Figure 5.19 : Received Eye Diagram–1 Channel Transmitted 142
Figure 5.20 : 3 Channel OTDM Bit Error Rate Measurements 144
Figure 5.21 : PDM Transmitter Configuration 147
Figure 5.22a : PDM 3 Channel Eye Diagram 148
Figure 5.22a : PDM 3 Channel Data Pattern 148
Figure 5.23a : PDM 3 Channel Eye Diagram–Narrow Data Pulse 150
Figure 5.23b : PDM 3 Channel Data Pattern–Narrow Data Pulse 150
Figure 5.24 : PDM Receiver Configuration 151
Figure 5.25 : PDM Receiver Eye Diagram 152
Figure 5.26 : PDM 1 and 3 Channel Receiver Sensitivity 153
Figure 5.27 : PDM Transmission Configurations 154
Figure 5.28 : PDM Transmission Receiver Sensitivities 155
Figure 5.29 : PDM 100 km Transmission Optical Crosstalk 156
Figure 5.30a : Receiver Pulse Shape–0 km 158
Figure 5.30b : Receiver Pulse Shape–25 km 158
Figure 5.30c : Receiver Pulse Shape–50 km 159
Figure 5.30d : Receiver Pulse Shape–75 km 159
Figure 5.30e : Receiver Pulse Shape–100 km 160

Figure 3A.1 : MZI 2X2 SWITCH Block Diagram 172
Figure 3A.2 : MOD SRC Block Diagram 172
Figure 3A.3 : 4 CHANNEL ENCODER Block Diagram 173
Figure 3A.4 : 4 CHANNEL TRANSMITTER Block Diagram 173
Figure 3A.5 : 4 CHANNEL DMUX Block Diagram 174
Figure 3A.6 : 4 CHANNEL RECEIVER Block Diagram 174
Figure 3A.7 : FIBER MODEL Block Diagram 175
Figure 3A.8 : OTDM SYSTEM Block Diagram 175

Figure 3A.9 : 4 CHANNEL TRANSMITTER OVERVIEW Block Diagram 176

Figure 5A.1 : Optical Amplifier Configurations 193

Figure 5B.1 : Bit Error Rates for 0 km Transmission 194

Figure 5B.2 : Bit Error Rates for 25 km Transmission 194

Figure 5B.3 : Bit Error Rates for 50 km Transmission 195

Figure 5B.4 : Bit Error Rates for 75 km Transmission 195

Figure 5B.5 : Bit Error Rates for 100 km Transmission 196

1.0 Introduction

Until the late 1970's, the attenuation characteristics of fiber optic cable made long-distance optical transmission impractical. Over the past 15 years, the development of relatively low-cost, low-loss optical fiber has made long-distance communication using optical carriers a viable alternative to copper wire or microwave based transmission systems.

Communication systems designers are interested in fiber optic transmission systems because of the enormous bandwidth available at optical frequencies. Relative to microwave or copper wire systems, optical systems offer a bandwidth advantage of several orders of magnitude. The current problem is to come up with transmission methods to take advantage of this available bandwidth.

Utilization of this bandwidth will likely involve wavelength division multiplexing of several optical carriers. Figure 1.1 shows a possible overall architecture of a multi-carrier optical transmission system. This method would first involve the generation of a set of relatively closely spaced carriers. Information in either analog or digital form would then be impressed on each carrier, and the carriers would be combined and sent down the fiber link. The receiver would separate the carriers by some filtering mechanism and extract the information from each carrier.

This thesis examines a carrier modulation scheme which attempts to maximize the amount of digital information impressed on a single carrier. There are two important problems in generating a high bit rate optical signal for long-haul transmission which this scheme addresses. The first major difficultly is modulating the optical carrier at multi-Gb/s data rates. Using a digital electrical signal to modulate the carrier directly is somewhat limiting since commercial high speed digital electronics are only now producing 10 Gb/s

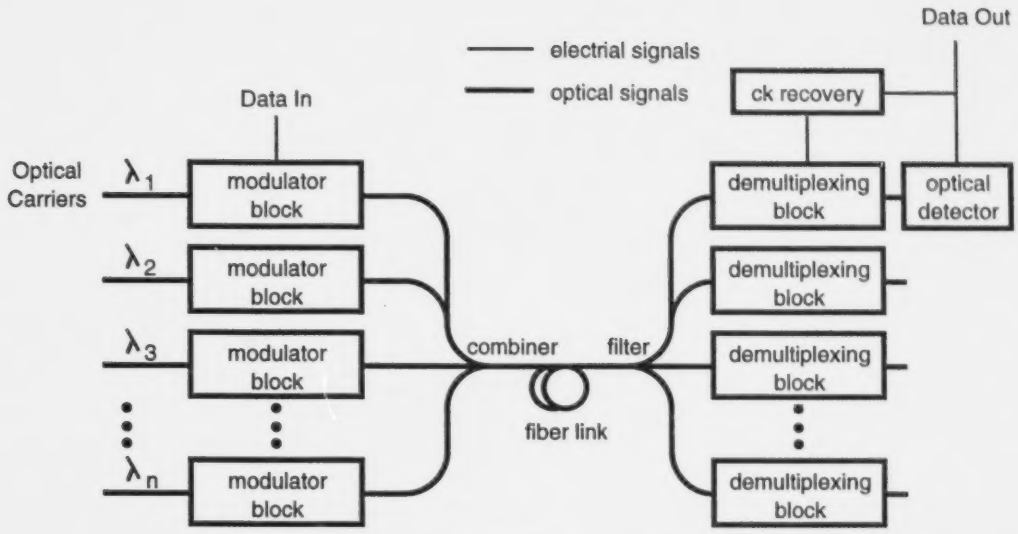

Figure 1.1 : Wavelength Division Multiplexed Transmission System

streams [1]. In addition, manipulating multi-Gb/s streams in electronic form is expensive as well as technically complex. The modulation scheme proposed here circumvents these bottlenecks by optically multiplexing a number of high-rate, digital, optical, data streams. This modulation scheme is classified as an optical time-division multiplexing, or OTDM technique.

Second, the spectral width of the optical signal must be kept as narrow as possible. A narrow spectral width is desirable because conventional silica fiber is dispersive. In other words, since fiber propagates different optical frequencies at different group velocities, a digitally encoded optical signal with a relatively large spectral width will have its pulses spread out as it propagates down the fiber. In effect then, spectral broadening increases inter-symbol interference. For long haul 1550 nm transmission at bit rates above a few gigabits per second, the inter-symbol interference due to chromatic dispersion significantly degrades the bit error rate of the system [2]. The modulation method suggested by this thesis attempts to minimize the spectral width of the transmitted signal by

externally modulating the carrier, as opposed to modulating the laser source directly. Direct modulation of the laser introduces laser 'chirp', or modulation of the laser wavelength, as the current drive to the laser varies [3].

These are by no means the only problems associated with long-haul high-speed optical transmission. There are a host of other concerns including maximizing optical power coupled into the fiber, minimizing and compensating for optical attenuation in the fiber, and maximizing receiver sensitivity to name just a few. However, these issues are common to all transmitted optical signals, and this thesis will emphasize the generation of a high-speed, narrow linewidth optical signal to be transmitted down the fiber.

1.1 OTDM Overview

The OTDM approach examined in this thesis involves the use of a continuous wave optical source to avoid the laser chirp associated with direct modulation of the laser light source. The signal modulation is done externally, using lithium niobate optical switches. Figure 1.2 shows the current design of the modulator/multiplexer block used in the transmitter. This OTDM architecture was conceived by Dr. Jan Conradi and Dr. Ian MacDonald of TR Labs in late 1991, and is similar to a two channel OTDM structure suggested by Anders Djupsjöbacka in 1988 [4]. In addition, Nick Jaeger, an independent researcher at University of British Columbia, filed a patent in mid-1992 for a 'commutator switch'. In a related application description file [5], he suggests that the switch can be used as a building block for multiple-stage OTDM, and this is almost identical to the concept examined in this thesis.

The input to the block is a continuous wave optical carrier generated by a laser operating under dc conditions. The first stage of the transmitter in Figure 1.2 simply divides the optical beam into four time interleaved pulse streams on separate waveguides using the optical switches numbered 1,2a, and 2b. The ideal optical switch can be

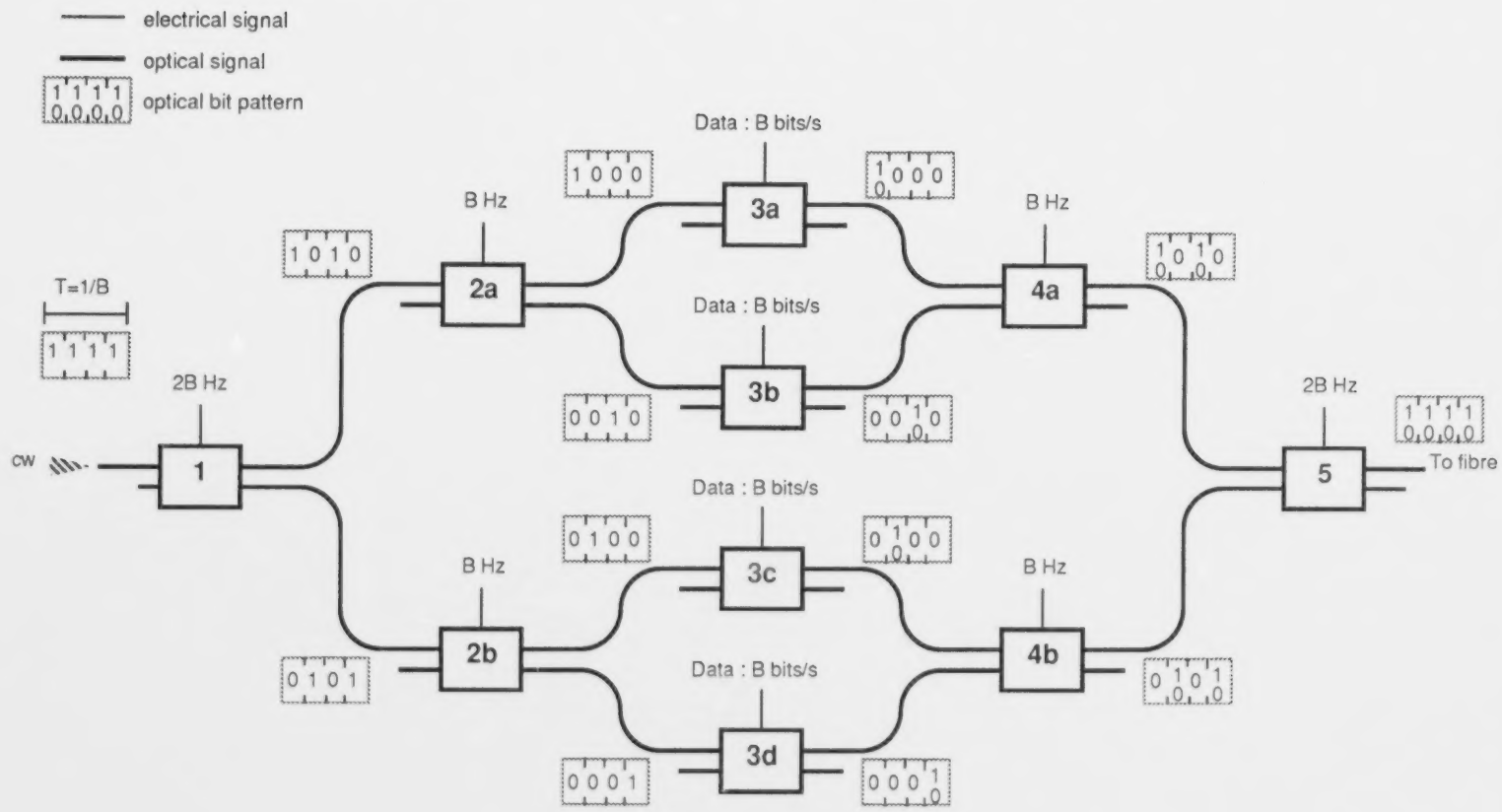

Figure 1.2 : Transmitter Block Diagram

conceptualized as a black box with two inputs and two outputs. The switch is driven by an electrical signal which routes the input signals to one output port when a positive electrical signal is applied and to the other output port when a negative signal is applied. To point out the relative timing of the pulses created on each input or output, a four bit 'frame' is displayed above each waveguide. One input to the first switch is a continuous optical beam. The other input is not used. If the desired bit rate is 4B bits per second, then the first switch is 'clocked' with a sinusoidal electrical signal at a frequency of 2B Hz. The output at one port is a sequence of the type 1010, and the output at the other port is the complement, or 0101. Similarly, switches 2 and 3 are operated at a frequency of B Hz and serve to divide the beam again to produce 1/4-duty-cycle pulse streams on each waveguide.

The information is impressed on the pulse stream by the second stage of the transmitter block. Switches 3a through 3d are the modulators, and each receives an input of optical pulses at rate B with a duty cycle of 1/4. The other input is closed off. The switches are driven by the electrical information signal at a rate of B bits/s. The output of each switch is then either an optical pulse (1) or no optical pulse (0) for that portion of the 4 bit frame.

The third set of switches, which is composed of blocks 4a, 4b, and 5, multiplexes the optical data streams. Now each switch utilizes two inputs and only one output. Switches 4a and 4b interleave two bit positions each, and are driven with sinusoidal electrical signals at frequency of B Hz. Switch 5 performs the final multiplex and operates at a frequency of 2B Hz. The output signal from switch 5 is a stream of modulated optical pulses at bit rate of 4B bits/s, and is ready for transmission down the fiber medium.

Referring back to Figure 1.1, the information at each carrier wavelength is recovered in the receiver blocks, and then converted from optical pulses to electrical pulses by optical detectors such as PIN or APD devices. An expanded view of the OTDM

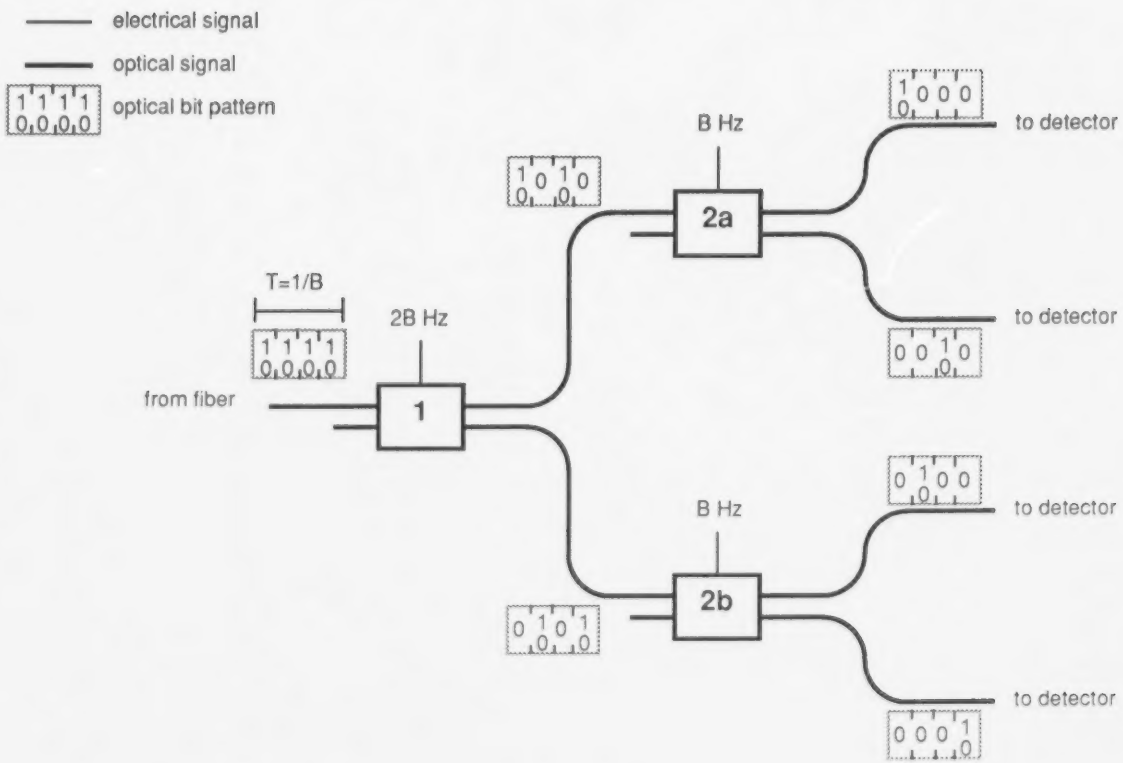

Figure 1.3 : Receiver Block Diagram

receiver configuration is shown in Figure 1.3. Switch 1 is driven by an electrical sinusoidal signal of frequency 2B Hz, and divides the arriving optical signal of bit rate 4B bits/s into two 2B bits/s streams. Switches 2a and 2b are driven at a frequency of B Hz and divide the signals down to the original B bits/s rate. Essentially, the structure of the receiver is identical to that of the first section of the transmitter composed of switches 1, 2a and 2b.

With the basic operation of the modulation and demultiplexing blocks now described, one may well wonder why such a 'complex' architecture is used. After all, it would appear to be much simpler to use a single switch with continuous wave optical input and use an electrical bit stream at a rate of 4B bits/s as the drive signal. At lower bit rates this is certainly true. However, as indicated previously, it becomes difficult to generate an electrical digital stream at high bit rates, and the optical multiplexing function serves to extend the bit rate capability of the system.

Therefore, considering only the generation of a high rate optical stream, if the maximum possible digital stream rate is B bits/s, we can use N stages of optical switches to achieve a final optical signal pulse rate of 2^N*B bits/s. We are limited then by the minimum of the bandwidth of the optical switch or the bandwidth of the electrical sinusoid required to drive the switch. The upper frequency limit of electrical sinusoidal signal generation is significantly greater than that of square wave signals. If the maximum electrical sinusoidal frequency is S and the maximum electrical bit rate is B, then a maximum of

$$N = \log_2\left(\frac{2S}{B}\right) \tag{1.1}$$

switch stages can be used to achieve an optical output bit rate of 2^N*B bits per second. For our purposes, two stages of optical switches were chosen to keep the analysis simple and still demonstrate that this architecture can operate with multiple multiplexing stages.

Another advantage of demultiplexing in the optical domain is that the electrical noise bandwidth at the detector is limited. For example, in a 10 Gb/s direct detection system, the equivalent noise bandwidth at the receiver may be 6 to 7 GHz. If the same 10 Gb/s optical signal is optically demultiplexed into four 2.5 Gb/s streams prior to detection, the electrical noise bandwidth can be reduced by a factor of four. In general then, optical demultiplexing reduces the electrical noise bandwidth of the system by a factor of 2^N. The exception to this generalization is systems in which the fundamental limit set by the number of photons per bit is encountered. This may be the case in systems which use optical amplifiers.

The goal of this thesis is to investigate the feasibility of the optical time division multiplexing concept through computer simulations and experimental demonstration. The computer simulation models the OTDM system with 4 input electrical data streams at the OC-48 or 2.48832 Gb/s rate resulting in a final optical throughput rate of 9.95328 Gb/s, or the OC-192 rate. The experimental work conducted at TR Labs involves implementing a scaled down version of the four channel system to demonstrate the OTDM concept.

With these objectives in mind, the optical switches should have bandwidths of at least 5 GHz with possible bandpass operation since the switches are driven with single frequencies at any given time. The modulators should be broadband devices with a bandwidth of at least 3-4 GHz, and must have linear phase response since they operate with a digital signal as input.

The operating wavelength of the system has been chosen to be in the 1550 nm region. This choice was made since the fiber attenuation minimum in conventional silica fiber occurs near this wavelength. In addition, a 1550 nm wavelength facilitates the use of erbium-doped fiber optical amplifiers which are efficient in that region of the spectrum.

With the basic operation of the OTDM transmission scheme now described, we move on to discuss theoretical and practical considerations of optical switches and modulators in Chapter 2. Several architectures are analyzed and evaluated concerning their suitability for use in the overall OTDM system. In Chapter 3, we present computer simulation results of the entire OTDM system from transmitter to receiver, and discuss the performance of the system as a function of various device parameters. In Chapter 4, we examine the experimental setup and provide an analysis of the individual components of the system. The experimental results obtained operating the OTDM system as a whole are presented in Chapter 5. As well, an alternative multiplexing technique, namely polarization division multiplexing, is briefly examined because it deals with some of the shortcomings of OTDM. Finally, Chapter 6 concludes this work with a short review and explores some possible avenues for further research.

2.0 Electro-optic Switch and Modulator Theory

The basic functioning of the OTDM transmitter and receiver blocks were introduced on a fairly high level in Chapter 1. In Chapter 2, we discuss in some detail the physical and mathematical theory behind the electro-optic switching elements which were only shown as blocks in the previous chapter. The electro-optic switch is really the most critical element in the proposed system and is used to switch, modulate, multiplex, and demultiplex optical streams. As was shown in Figures 1.2 and 1.3, all blocks can be implemented with 2x2 switches. However, it may be advantageous to use two different electro-optic element designs to accomplish the distinct switching (chopping, multiplexing and demultiplexing) and modulating (or encoding) functions. Therefore, after some preliminary remarks concerning lithium niobate based devices, this chapter will concentrate first on modulator designs, which are in general more simple structures to analyze, and then move on to examine four port, 2x2 switches.

2.1 Electro-optic Devices in Lithium Niobate

The technology of fabricating various optical devices using lithium niobate as a substrate is currently in an advanced state [6]. Lithium niobate, or $LiNbO_3$, is preferred as the substrate material for a number of reasons. First, $LiNbO_3$ possesses a high electro-optic coefficient, which means that a relatively low voltage is required to induce a given refractive index change in the material. In addition, the material is commercially available in up to 7.5 cm diameter wafers. Finally, the properties of lithium niobate have been quite thoroughly investigated, and a number of laboratories have optimized the processing procedure of the material.

Waveguiding channels are formed at the surface of a $LiNbO_3$ wafer by first depositing thin titanium films on the substrate. The substrate and film are heated to about

1000°C to allow the titanium to diffuse into the substrate and create a waveguiding region having a slightly higher refractive index than the surrounding material. Afterwards, a thin film of silicon oxide is usually placed on top of the substrate to insulate the guides from any metal which may be placed above. Metal electrodes are then deposited beside or on top of the waveguides. As is explained in more detail later, an electric field applied across the electrodes will penetrate down into the waveguides and alter their refractive indices. Several problems accompany this fabrication process [7]. Outdiffusion of O_2/Li_2O at the surface usually results in a thin parasitic film waveguide at the surface. Also, the heating environment must be carefully controlled with respect to temperature (within 0.5°C) and purity to ensure reproducible fabrication. In addition, precise mask widths and mask alignment are required. Finally, deposition thicknesses of the electrodes and especially the titanium films must be kept uniform. Once the diffusion process is completed, waveguide I/O ports must be cut and polished and connected to fiber pigtails to achieve low loss at the fiber/waveguide junction.

2.2 Electro-optic Modulators

Having briefly examined the rationale for choosing lithium niobate based devices and identifying some associated problems, we will now move on to take an in-depth look at several optical modulator designs.

2.2.1 The Mach-Zehnder Interferometer

The Mach-Zehnder interferometer is conceptually the most elementary modulator structure. In its simplest form, a single input waveguide is symmetrically split into two branches which are then separated sufficiently to avoid mode coupling between them. After continuing for a short distance of typically millimeters or centimeters , the branches are then recombined to form the output waveguide as shown in Figure 2.1.

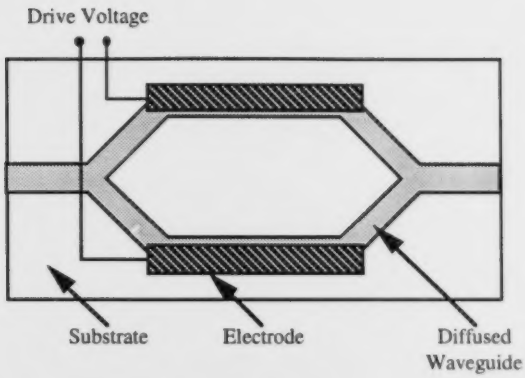

Figure 2.1 : Z-Cut Mach-Zehnder Interferometer

An important property of lithium niobate is that the electro-optic coefficient depends on the orientation of the crystal. The 'cut' of the crystal refers to the crystal axis which is perpendicular to the surface of the substrate. The strongest electro-optic coefficient is termed r_{33} (= 30.9 * 10^{-10} cm/V) and is parallel to the z-axis of the crystal which points up out of the page in Figure 2.1. The electrodes are almost always placed in such a way as to utilize the r_{33} coefficient. As shown in Figure 2.1, the electrodes are placed above the waveguides for the z-cut orientation to utilize r_{33}. For an x-cut crystal, the electrodes are placed beside the guides.

2.2.1.1 Interferometer Switching Voltage Calculation

Ideally, for no voltage applied across the electrodes, the input optical signal is symmetrically split and then recombined at the output in phase, and the transmitted intensity is maximum. Applying a voltage across the electrodes induces opposite changes in the refractive indices of the two underlying waveguides, and thus creates a phase shift between the optical signals in the two branches. The combined mode distribution at the output guide is no longer single mode and cannot propagate in the single mode output waveguide; instead, it is radiated into the surrounding substrate.

If sufficient voltage is applied to create π radians of phase difference between the arms, the transmission is minimal. Since the on and off states are tuned electronically, the extinction ratio of the device is quite good and is typically greater than 15 to 20 dB. The voltage required to achieve π radians of phase shift between the two arms of the interferometer is termed V_π. To determine V_π for the interferometer, we must relate the applied voltage to the induced index change in the material. The derivation of V_π contained in equations (2.1) to (2.8) is taken explicitly from Tamir's optoelectronics textbook [6]. For a uniform electric field along the z-axis of the crystal, the induced index change is:

$$\Delta n_{33} = -\frac{n^3}{2} r_{33} E_z \tag{2.1}$$

If the two electrodes were configured as a two plate capacitor with applied voltage V and gap width G, the electric field between them would be :

$$E_z = \frac{V}{G} \tag{2.2}$$

It is convenient to express the electric field as in (2.2) and add a correction factor Γ to account for the non-uniformity in both the electric field between the electrodes and the optical field in the waveguides :

$$E_z = \frac{V}{G}\Gamma \tag{2.3}$$

The correction factor Γ is called the overlap integral and in effect represents the efficiency of the overlap between the electric and optical fields and is expressed as :

$$\Gamma = \frac{G}{V} \int_{-\infty}^{\infty} \int_{-\infty}^{\infty} E_{(x,y)} \, |A_{(x,y)}|^2 \, dy \, dx \tag{2.4}$$

where E is the applied electric field, A is the normalized optical field in the waveguide and the x-y plane is the plane perpendicular to the waveguide. Substituting

(2.3) into (2.1) and dropping the axis subscripts we obtain the index change as a function of the applied drive voltage :

$$\Delta n = -\frac{n^3}{2} r \frac{V}{G}\Gamma \qquad (2.5)$$

The phase change in one arm over the length of interaction L is:

$$\text{phase shift} = \Delta\beta\, L = \Delta n\, \beta\, L$$

$$= -\pi n^3 r \frac{VL}{G\lambda}\Gamma \qquad (2.6)$$

β is the propagation constant and is equal to $2\pi/\lambda$. As indicated earlier, π radians of phase shift between the two arms of the interferometer is required for complete modulation. The phase change in each arm is $\Delta\beta L$ in opposite directions and therefore the total phase difference between the two arms is $2\Delta\beta L$. Setting the phase difference between the arms $2\Delta\beta L$ equal to π, we obtain the switching voltage V_π:

$$V_\pi = \frac{\lambda G}{2n^3 r \Gamma L} \qquad (2.7)$$

When comparing devices of different lengths and drive voltages, it is convenient to express (2.7) as a voltage length product :

$$V_\pi L = \frac{\lambda G}{2n^3 r \Gamma} \qquad (2.8)$$

From equation (2.8), we can see that to obtain a device with a low voltage length product, a narrow gap and good field overlap is required. For the z-cut interferometer, the narrow electrode gap is somewhat problematic, since the waveguides must be separated sufficiently to eliminate coupling. One method to reduce coupling is to fabricate waveguide branches of slightly different widths. Typical width differences are on the order of 1 μm [8]. This procedure reduces the separation required, and thus allows a narrower gap.

As indicated by (2.4), the overlap integral Γ depends on the geometry of the electrodes, the optical mode profile in the waveguides, and the relative position of the electrodes with respect to the waveguides. Several authors have investigated the optimization of the overlap integral as a function of various device configurations [9,10].

Using some typical parameter values, we can get an estimate of the required Mach-Zehnder modulator switching voltage using equations 2.7 and 2.8. For a 1550 nm operating wavelength, an optical index of 2.2, typical widths of 6 μm for the electrode gap and optical guide, and an overlap integral of 0.25 as approximated from published graphical results [11], we can calculate the voltage length product as $V_\pi L = 5.65$ V cm. For a 1 cm length device then, the switching voltage is 5.65 V. The accuracy of this figure depends strongly on the value of the overlap integral. Again, calculation of the overlap integral is quite a complex problem and depends on the physical geometry of the electrodes and optical waveguides. As well, the presence and thickness of a SiO_2 buffer layer which typically insulates the waveguides from the electrodes influences the overlap integral. The presence of a 0.2 μm thick SiO_2 buffer layer has been reported to increase the switching voltage by 30 to 40 percent [12,13]. Therefore we have not calculated the overlap integral directly here, and have instead used a calculated value from published results [11].

The output intensity η of the modulator is a function of the total phase shift between the waveguide arms, and is given by the squared magnitude of the vector sum of the electric fields of the optical signals at the modulator output [13]:

$$\eta = \cos^2\left[\Delta\beta L\right] \tag{2.9}$$

Equation (2.9) can also be conveniently expressed in terms of the applied drive voltage V and the required half-wave voltage V_π:

$$\eta = \cos^2\left[\frac{\pi V}{2 V_\pi}\right] \tag{2.10}$$

2.2.1.2 Interferometer Bandwidth

The bandwidth of the interferometric modulator depends on the type of electrode employed. For lumped element electrodes as shown in Figure 2.2a, the electrodes are structured as a terminating capacitor, with a shunt resistance R_{term} matched to the drive source impedance, typically 50 ohms. The bandwidth of the lumped element structure is determined by the minimum of either the RC time constant, $f_{RC}= 1/(\pi R_{term}C)$, or the electrical transit time cutoff frequency, $f_{tt}= c/(\pi L n_{eff})$, where L is the electrode length. Using an effective microwave index of $n_{eff} = 4.2$, $f_{tt}L$ is approximately 2.2 GHz cm for lithium niobate [13].

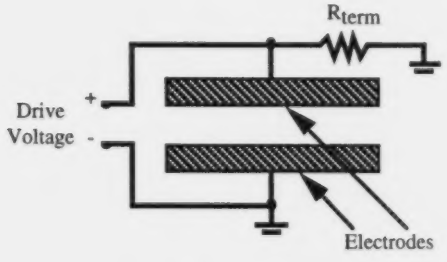

Figure 2.2a : Lumped Element Electrode Structure

Electrodes can also be structured in a travelling-wave configuration. In this case, the electrode acts as a continuation of the source transmission line as shown below in Figure 2.2b.

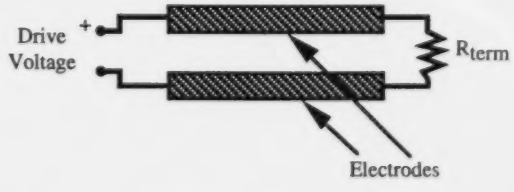

Figure 2.2b : Travelling Wave Electrode Structure

Again, the termination resistor R_{term} is matched to the impedance of the transmission line. Increased bandwidth can be achieved since the electronic and optical signals travel across the structure together. For travelling wave electrode designs, the bandwidth is limited by the microwave attenuation losses of the electrodes and the velocity mismatch between the optical and electrical signals. Consider a modulator of length L which has electrodes with exponential resistive losses of α/cm. If a voltage signal with amplitude V_o, phase $\varnothing_o$, and frequency f is applied to the electrodes, then the voltage seen by the optical signal at a distance z from the start of the electrode is given by :

$$V_{(z,\varnothing_o,f)} = e^{-\alpha z} V_o \cos\left[2\pi (n_m - n_o) \frac{f}{c} z - \varnothing_o\right] \qquad (2.11)$$

where c is the speed of light in a vacuum, and n_m and n_o are the effective microwave and optical indices of refraction, respectively. Substituting this frequency dependent voltage into equation (2.6), we integrate along the length of the device to obtain the phase change in one waveguide:

$$\Delta\beta L = \int_{z=0}^{z=L} \frac{-\pi n^3 r \Gamma}{G\lambda} V_{(z,\varnothing_o,f)}\, dz$$

$$= -\pi n^3 r \frac{V_o}{G} \Gamma \frac{L}{\lambda} \int_{z=0}^{z=L} \frac{e^{-\alpha z}}{L} \cos\left[2\pi (n_m - n_o) \frac{f}{c} z - \varnothing_o\right] dz$$

$$= \overline{\Delta\beta L}\ H(f) \qquad (2.12)$$

where

$$\overline{\Delta\beta L} = -\pi n^3 r \frac{V_o}{G} \Gamma \frac{L}{\lambda} \qquad (2.13)$$

and is virtually identical to equation (2.6) and represents the phase shift at low frequency due to the applied voltage of amplitude V_o. H(f) is then :

$$H(f) = \int_{z=0}^{z=L} \frac{e^{-\alpha z}}{L} \cos\left[2\pi (n_m - n_o) \frac{f}{c} z - \varnothing_o\right] dz \tag{2.14}$$

and is the frequency dependent term which reduces the effective drive voltage at higher frequencies. Performing the integration we can obtain the closed form solution for H[f] as [14]:

$$H(f) = e^{(-\alpha L/2)} \left[\frac{\sinh^2\left(\frac{\alpha L}{2}\right) + \sin^2\left(\frac{\xi L}{2}\right)}{\left(\frac{\alpha L}{2}\right)^2 + \left(\frac{\xi L}{2}\right)^2} \right]^{\frac{1}{2}} \tag{2.15}$$

where,

$$\xi = \frac{2\pi f (n_m - n_o)}{c} \tag{2.16}$$

and

$$\alpha = \frac{\ln 10}{10} \alpha_o \sqrt{f} \tag{2.17}$$

The parameter α_o in the above equation expresses the attenuation losses of the electrodes in the conventional units of dB/(cm $GHz^{1/2}$). Equations (2.15) to (2.17) comprehensively describe the decrease in the effective applied voltage as a function of frequency resulting from microwave attenuation and velocity mismatch effects. A study of equations (2.15) to (2.17) reveals several factors which determine the bandwidth of the device. Certainly, a lower attenuation factor, α_o, is desirable for high frequency performance. To achieve a small attenuation factor, the width of both the electrodes and the gap should be made relatively wide, as indicated by the published results of Chung and Chang [15]. For a typical value of α_o=1.0 dB/(cm $Ghz^{1/2}$) the electrode width and gap should be about 8 μm each. Note that this desire for large electrode and gap dimensions

conflicts with the earlier stated requirement for a small gap to achieve a low switching voltage.

The length of the device also plays an important role in the bandwidth of the interferometer, and of all electro-optic devices in general. As can be seen by inspection of the above equations, an increased device length results in faster high frequency roll-off of the device response. So, other factors remaining constant, a shorter device is a faster device. Note again, however, that a tradeoff exists between device length and drive voltage. From the voltage-length product equations (2.7) and (2.8) we can see that as the device length is decreased, the switching voltage V_π must increase proportionally.

A final important factor in determining the device bandwidth is the mismatch between the velocities of the electric wave which travels down the electrodes and the optical wave propagating in the waveguide. Intuitively one can appreciate the importance of velocity mismatch effects by considering an electrical pulse and an optical pulse which start out together at the beginning of the interaction region. If there is a difference in the propagation velocities of the two pulses, they will become less and less aligned as they travel across the device.

Several techniques have been introduced to try to overcome the velocity mismatch problem. Real velocity matching techniques attempt to speed up the typically slower electric wave. In general, little can be done to slow down the optical wave which propagates through the lithium niobate crystal which has a refractive index of $n_o \cong 2.2$. To speed up the electric wave, one can experiment with the electrode and gap dimensions to reduce the effective microwave index n_m which typically has a value of around 4 to 5. In general, the microwave index increases as electrode width and height increase, and decreases as the gap increases [15]. Another technique to lower the microwave index involves etching a groove in the electrode gap region to allow more of the electric wave to

propagate in the lower index air [16]. A shielding ground plane placed just above the electrodes has also been successfully used to speed up the microwave [17].

Artificial velocity matching techniques do not actually change the microwave index, but instead attempt to cancel out the effects of the velocity mismatch by periodically reversing the polarity of the electrodes. Extremely high frequency bandpass type devices have been demonstrated using this technique. Korotky and Veselka have reported experiments in which a bandpass interferometric switch was operated at 36 GHz [18]. Such devices are useful when extremely high frequency operation without broadband capability is required. At the expense of increased drive voltage, it is possible to flatten out the frequency response of the device using special electrode sequences. Dolfi and Nazarathy report operation of a lithium niobate modulator with a 13-bit Barker code electrode pattern with a 5 dB optical bandwidth of 40 GHz. Their theoretical predictions extend the frequency response out to 70 GHz [19]. If the phase response of such a device is linear, this type of design is more appropriate for use in high speed broadband digital applications.

To get some idea of the frequency response of a typical device, equations (2.15) to (2.17) will be used in a numerical example. For 1 cm long electrodes, and common experimental values of n_m=4.2, n_o=2.2, and microwave losses of α_o=1.0 dB/(cm $Ghz^{1/2}$), H[f] was calculated. Figure 2.3 graphically shows the theoretical frequency roll-off of a modulator with the stated parameters. The frequency at which the modulation depth η falls to one half of its low frequency value occurs when H(f) = 0.5 and is f= 7.0 GHz. Therefore, the 3 dB optical bandwidth of such a device is 7.0 GHz.

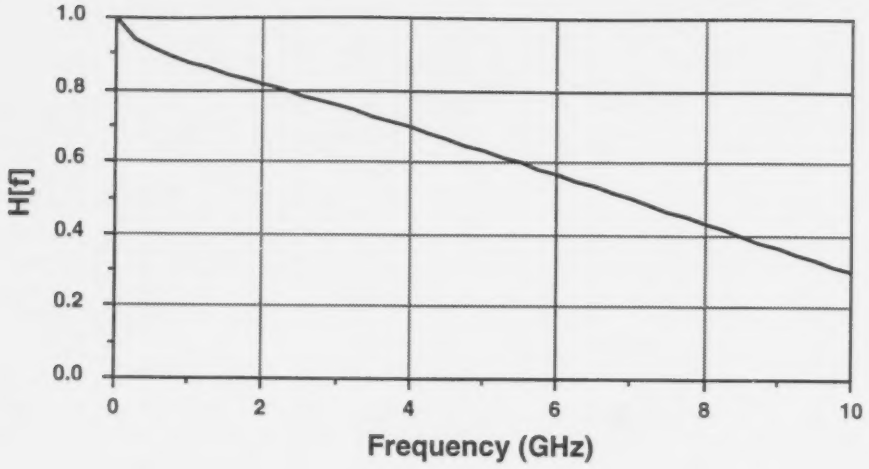

Figure 2.3 : Modulator Frequency Response

2.2.1.3 Residual Phase Modulation in Interferometers

A final aspect of the Mach-Zehnder interferometer that is briefly addressed in this section is residual phase modulation of the optical signal, which is often referred to as residual modulator chirp. This phenomenon may occur as a result of asymmetrical changes in the propagation constants of the two arms of the device. Consider again the Mach-Zehnder interferometer shown in Figure 2.4, which has an input optical electric field E_o and output optical electric field E_{out}. Let the two branches have length L and propagation constants $ß_1$ and $ß_2$.

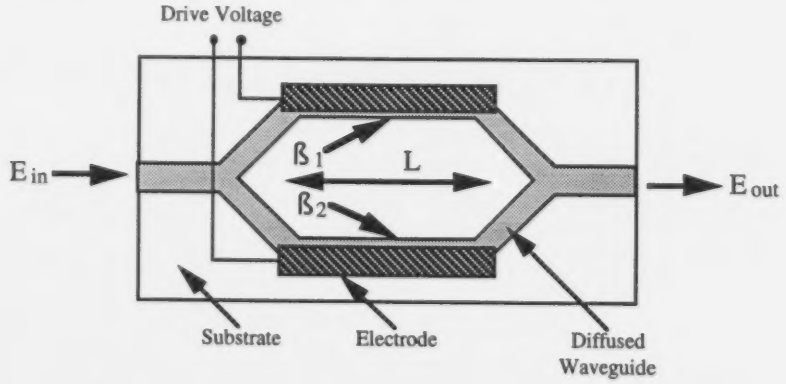

Figure 2.4 : Mach-Zehnder Interferometer

The output electric field is given by the sum of the two electric fields emerging from the two arms:

$$E_{out} = \frac{E_{in}}{2} e^{-j\beta_1 L} + \frac{E_{in}}{2} e^{-j\beta_2 L}$$

$$= \frac{E_{in}}{2} \left(e^{j\Delta\beta L} + e^{-j\Delta\beta L} \right) e^{-j\bar{\beta} L}$$

$$= E_{in} \cos(\Delta\beta L) e^{-j\bar{\beta} L} \qquad (2.18)$$

where $\Delta\beta = \frac{\beta_1 - \beta_2}{2}$ and $\bar{\beta} = \frac{\beta_1 + \beta_2}{2}$

The $\cos(\Delta\beta L)$ term in equation 2.18 reflects the electric field amplitude response of the modulator and squaring this term yields the intensity response $\eta = \cos^2(\Delta\beta L)$ as given in equation (2.9). The phase response is given by the $e^{-j\bar{\beta} L}$ term and is a function of both β_1 and β_2. During modulation, if β_1 and β_2 are altered by the same factor in opposite senses, then $\bar{\beta}$ is constant and there is in principle no phase modulation. This requires that a symmetric electrode structure is used, which in theory will produce equal and opposite index changes in the two interferometer arms. Of course in practice, due to fabrication tolerances concerning electrode and waveguide positioning and dimensioning, there will be slight differences in the index changes produced through the two arms, and thus some phase modulation may occur. Asymmetric electrode structures, and electrodes which alter the index in only one branch of the interferometer will also give rise to phase modulation.

The effect of phase modulation is to broaden the spectrum of the transmitted signal, and thus increase the distortion produced by fiber dispersion. Determining the penalty which modulator chirp imposes on transmitted signals is not a simple procedure and is not included in this section. Thorough, published analyses of chirp and transmission penalties [20,21] indicate that using symmetric electrode structures may degrade the square-root length times bandwidth product by perhaps a few percent. In addition, there are methods

by which chirp can be used to compensate for fiber dispersion and actually lower the dispersion penalty [20,22,23].

2.2.2 The Directional Coupler

Having introduced the fundamentals of electro-optic device operation in the context of the interferometer in the previous section, we will now move on to review quickly several other possible modulator structures. This section will examine the directional coupler and its use as a modulator. The general structure of the directional coupler is a 2x2 switch as shown in Figure 2.5:

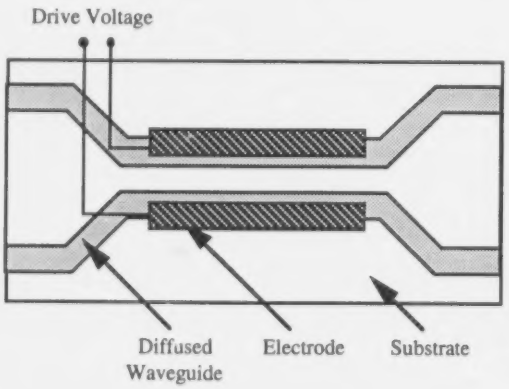

Figure 2.5 : Directional Coupler

Two widely spaced input waveguides are brought close enough together (typically 5-10 μm) so that light may be coupled between the guides. To use this device as a modulator, a single input guide is used, and light is either retained in that guide in what is called the bar state , or coupled out into the adjacent guide in the cross state. The switching, or modulation, is accomplished by the application of an electric field across the guides to alter their refractive indices. The transfer or crossover characteristic can be determined by solving the coupled mode equations. Equations (2.18) to (2.23) are taken directly from Tamir's text on optoelectonics [24]. The coupled mode equations are:

$$R' - j\delta R = -j\kappa S \tag{2.18}$$

$$S' - j\delta S = -j\kappa R \tag{2.19}$$

and

$$\delta = \frac{\Delta\beta}{2} = \frac{2\pi\ (n_2 - n_1)}{\lambda \quad 2}$$

where R and S are the complex amplitudes of the optical signals in the two waveguides and R' and S' are the spatial derivatives with respect to the direction of propagation. The parameters n_2 and n_1 are the refractive indices of the two waveguides and thus δ is proportional to the difference in the propagation constants between the two guides. The parameter κ is the coupling coefficient with units of cm^{-1} and depends on the geometry of the waveguides and the wavelength of operation. Solving the coupled mode equations (2.18) and (2.19), for unity input to one guide, the transfer characteristic which describes the intensity coupled into the second guide over a distance L can be determined as [24]:

$$\eta = \frac{1}{1 + (\delta/\kappa)^2} \sin^2 \kappa L \left[1 + (\delta/\kappa)^2 \right]^{\frac{1}{2}} \tag{2.20}$$

With no voltage applied to the electrodes, $\Delta\beta=0$, and $\eta = \sin^2 \kappa L$ so that complete crossover occurs for $\kappa L = n\pi/2$, where n is odd. In theory, one can fabricate a device of a single coupling length, $L = \pi/2\kappa$, and choose the cross state to be the off state of the modulator. The on or bar state is obtained by applying a voltage across the electrodes to adjust $\Delta\beta$ such that:

$$\sin^2 \kappa L \left[1 + (\delta/\kappa)^2 \right]^{\frac{1}{2}} = 0 \tag{2.21}$$

To satisfy this condition, $\Delta\beta L = \pi\sqrt{3}$, which is a factor of $\sqrt{3}$ higher than that for the interferometer.

It is important to note that the bar state can always be realized electronically by adjusting $\Delta\beta$ such that equation (2.21) is satisfied. However, the cross state may only be perfectly achieved for $\Delta\beta L = 0$ and a device of exactly n (odd) coupling lengths. Thus, the extinction ratio of the simple directional coupler device in the cross state is determined by the ability to fabricate devices of precise coupling lengths. To overcome this fabrication sensitivity, the reversed $\Delta\beta$ directional coupler architecture has been used [25]. With this structure, both the cross and bar states may be realized electronically, which relaxes the fabrication tolerances considerably.

The drive voltage of the directional coupler is found by setting the total phase difference $2\Delta\beta L$ equal to the required $\pi\sqrt{3}$. The switching voltage V and the voltage length product VL are the same as the expressions (2.7) and (2.8) for the interferometric modulator except for the factor of $\sqrt{3}$:

$$V_\pi = \frac{\sqrt{3}\ \lambda G}{2n^3 r \Gamma L} \tag{2.22}$$

$$V_\pi L = \frac{\sqrt{3}\ \lambda G}{2n^3 r \Gamma} \tag{2.23}$$

As with the interferometer, the bandwidth of the directional coupler is limited by microwave transmission loss and velocity mismatch effects. However, with respect to the velocity mismatch loss, a correction factor is required to account for the fact that mismatch is less critical at the ends of the directional coupler than in the center region. Equations (2.15) to (2.17) can be used with an effective length of approximately $L/\sqrt{3}$ to account for the integrated effect of the mismatch [26]. So we see that the increased requirement in drive voltage for the directional coupler is compensated for by an increase in the device bandwidth.

Determination of chirp in the directional coupler is also an analytically involved process and will not be included in this discussion. Published results [20] show that unlike the interferometer, the directional coupler is by definition a chirp-inducing structure. However, as was the case for the interferometer, proper utilization of chirp may be employed to reduce the dispersion penalty from the chirp-free case.

2.2.3 The Mode Confinement or Cutoff Modulator

A third modulator structure briefly considered here is the mode confinement modulator. The physical layout of the device is shown below in Figure 2.6:

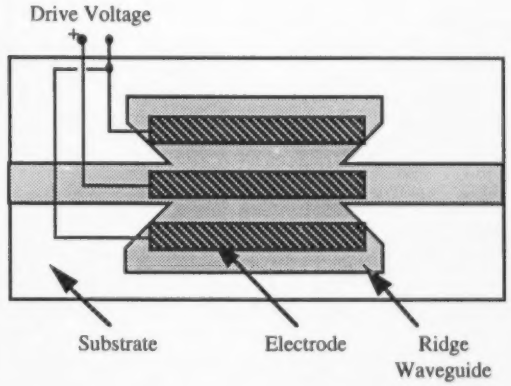

Figure 2.6 : Mode Confinement Modulator

The waveguide layout can be obtained by titanium indiffusion [27,28] and by etching the surrounding substrate to leave the 'butterfly' waveguide pattern. With no voltage applied between the drive electrodes, light entering the input ridge waveguide is partially scattered in the wider center-slab section, with a portion of the light passing through to the output ridge guide. With the correct applied voltage, a channel of higher index is induced in the center of the slab section, and most of the light is transmitted to the output guide. With a drive signal of the opposite polarity, the index in the center of the slab

is lowered and the input light is scattered significantly, with negligible light intensity passing to the output guide.

The intensity transfer characteristic is not trivial and cannot be conveniently expressed in closed form as was possible for the Mach-Zehnder interferometer and the directional coupler. Published results to date include the use of mode matching techniques [27] and the beam propagation method [28] to solve for the mode field distribution within the relatively complex waveguide structure.

As was the case for the directional coupler, chirp calculations for the mode confinement modulator are not trivial and will not be included in this discussion. Published results [20] show that for a similarly structured loss-modulator, chirp-free operation is not possible since the index change is brought about in a single waveguide only.

Advantages of the mode confinement modulator include its simplicity of design, good linearity, and relatively short length of around 2 to 3 millimeters. Disadvantages include considerable drive voltages, reported from 16 to 40 V, high loss in the on state (> 1 dB), the inability to trade off device length for drive voltage, and non-trivial device characterization. In addition, the device contributes chirp to the modulated signal. Finally, other important specifications such as device bandwidth, process repeatability, and ease of integration with devices of other fabrication methods, were not reported in the publications.

2.2.4 Modulator Selection for the OTDM System

Preliminary analysis suggests that the Mach-Zehnder type device might be best suited to satisfy the modulator performance requirements.

Too little is known about the cutoff or mode confinement modulator at this point to completely rule it out. However, a first pass indicates that it might not be suitable. The good linearity of the device is not required for digital applications. While the short length is

attractive, the drive voltage required is several times that for an interferometric or directional coupler type device. In addition, device length cannot be sacrificed for drive signal level. The high frequency applications of the device have not been explored in current literature, and integration with other modulators and switches on the same substrate may not be simple. For the OTDM application, a well-characterized, repeatable, integratable element is required. The purpose of the system is not to develop new or better single electro-optic devices, but to use the best existing elements to build up a rather novel multiplexing architecture.

The Mach-Zehnder structure is preferred over the directional coupler design for several reasons. First, although the directional coupler has increased velocity mismatched bandwidth of perhaps 30%, it also requires about a 70% increase in drive voltage. For 2.5 Gb/s operation, the modulator requires a 3 dB bandwidth of perhaps 2.5 GHz, and therefore it would be beneficial to trade off some extra bandwidth for decreased drive voltage. In addition, in practice it is possible that microwave loss and electrical packaging effects may limit the bandwidth of both devices to a greater extent than the velocity mismatch factor [29]. As well, the fabrication dependent coupling length problem of the directional coupler design is avoided. Finally, both chirp-free and chirping operation are possible with the interferometer design. Chirp-free operation is not possible with the directional coupler design.

One factor in favor of the directional coupler design is that directional coupler switches with a good response to ~5 GHz are required in the switching elements. If these switches have flat magnitude and linear phase response to 2.5 GHz, then they may be used as modulators. Cost may be reduced through the design and fabrication of a single type of building block. Another factor against the use of the Mach-Zehnder design is that in the z-cut configuration, it is somewhat difficult to design electrodes with a small gap, since the underlying waveguides must be separated by at least 20μm to eliminate coupling [14].

Again, this problem can be partially solved by using waveguide arms of slightly different widths (~1μm) which can reduce the required separation to about 6μm [7].

As far as DC drift is concerned, none of the three devices appears to offer an advantage over the rest. DC drift is a change of the required switching voltage observed over a period of time. This phenomenon has been investigated and has been attributed to several factors, including current leakage through the insulating SiO_2 buffer layer [30]. Drift has been reportedly reduced by etching away the buffer in the electrode gap [31], or by annealing the SiO_2 layer [14,32].

2.3. Electro-optic Switches

Having examined the operation of lithium niobate modulators in some detail, we will now move on to discuss several possible electro-optic switch structures.

2.3.1 The Balanced Bridge Interferometer

One type of switching structure similar in nature to the Mach-Zehnder modulator is the balanced bridge interferometer switch whose layout is shown in Figure 2.7 below :

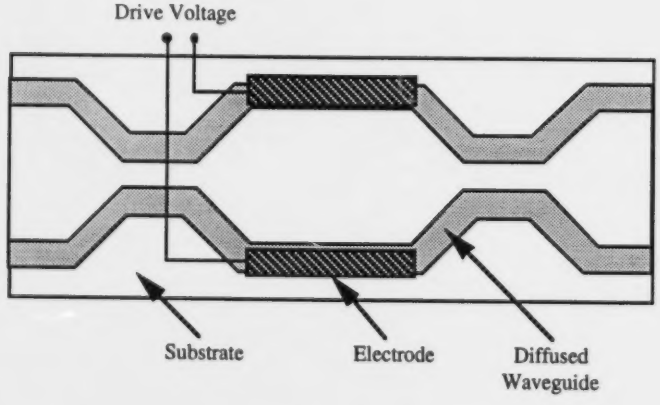

Figure 2.7 : Balanced Bridge Interferometer

Optical signals enter the two input waveguides which are brought close together to form a 3 dB coupler. The waveguides are then separated into a non-coupling Mach-Zehnder style phase-shift section, where the relative phase between the optical waves may be altered by the application of an electric field. Finally, the guides are brought together again through another 3 dB coupler, and then separated to yield the two output ports.

The bar state is achieved with no applied voltage, so each optical signal will remain in its guide and pass through to the output ports. The cross state is achieved by introducing π radians of phase shift between the two guides in the phase-shift section. The switching characteristic is identical to the interferometer modulation characteristic given by equation (2.9). In the balanced bridge context, η describes the intensity transferred between the guides, and L is the length of the phase-shifting electrode section.

Note that the switching characteristic of the Mach-Zehnder modulator or switch described by (2.9) is periodic with respect to drive voltage. In the OTDM system, this property can be exploited to produce optical modulation at higher frequencies than that of the electric drive signal by simply increasing the amplitude of the drive signal. For example, in the OTDM system, the first 5 Gb/s train of optical pulses may be produced by driving the first switch with a 5 GHz, V_π amplitude signal. Alternately, the 5 Gb/s pulse train may be produced using a 2.5 GHz drive signal with an amplitude of 2 V_π. This feature of the Mach-Zehnder type switch is examined later in the simulation work of Chapter 3.

The bandwidth of the balanced bridge device is also the same as for the interferometer, and is therefore given by equations (2.15) to (2.17).

Achieving perfect cross and bar states with the balanced bridge switch depends on the ability to fabricate 3 dB coupling sections at either end of the phase-shifter. If passive 3

dB couplers cannot be accurately produced, electronically tunable 3 dB couplers may be constructed.

With the cross and bar states tunable electronically, the fabrication dependencies of the device are greatly reduced, making it attractive for use in integrated optics applications. The tradeoff, however, is the substantial length required for the two 3 dB coupling sections and their associated converging and diverging waveguide sections.

2.3.2 The Directional Coupler Switch

One possible switching structure is the 2x2 directional coupler switch. The structure of the directional coupler switch was previously shown in Figure 2.3 and its operation described in Section 2.2.2. As indicated earlier, 2x2 switching is accomplished by using both input and both output waveguides.

The switching characteristic of the directional coupler described by equation (2.20) is non-periodic with respect to drive voltage. Thus, the $2V_\pi$ switching technique which was possible using the balanced bridge switch is not possible using the directional coupler.

2.3.3 The Digital Switch

Another possible 2x2 switch is the so-called digital switch, introduced by Silberberg et al. in late 1987 [33]. Its operation is digital in the sense that its response to increased drive voltage is not sinusoidal, but steplike. This type of device allows many devices to be driven at the same switching voltage, thereby eliminating different sources for each switch. The performance of the device is relatively insensitive to fabrication inconsistencies, and thus it is well suited for integration in multi-element configurations.

An example of a digital switch in the z-cut configuration is displayed in Figure 2.8:

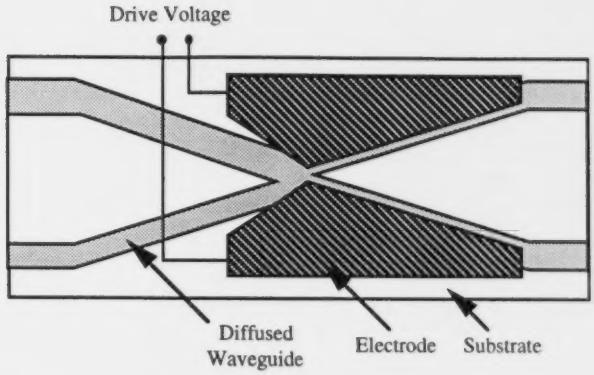

Figure 2.8 : Digital Switch

The input section on the left consists of two waveguides of slightly different widths. The center section is wide enough to support the second mode, and the output waveguides on the right are formed by symmetrically branching the center section. The symmetry of the output branch can be altered in either direction by the application of an electric field. With no field applied, the optical signal in either input branch is divided equally at the output branch. In the presence of an applied field, the output branch is made asymmetric, and the optical signals in the wide and narrow branches at the input are transmitted to the wide and narrow branches at the output through mode sorting. Switching is accomplished by reversing the polarity of the applied field [33].

Silberberg reports a 30V ($\Delta\beta L = 2\pi$ radians) switching voltage and -15 dB crosstalk level for experiments with an experimental z-cut device. Design improvements to lower the switching voltage are suggested. As well, it is indicated that the structure can be configured with travelling wave electrodes for high speed operation. Simulations by another researcher, W.K. Burns, predict complete switching for $\Delta\beta L = 1.23\pi$ rad for a similar x-cut device [34].

2.3.4 Switch Preference for the OTDM System

A preliminary review of the available devices seems to indicate that the balanced bridge interferometric type device might be best suited to satisfy the switch performance requirements.

As was the case with the mode confinement modulator, too little is known about the digital switch at this point to completely rule it out. However, the drive voltages reported to this date are not low enough to meet the approximately 10-15 volt limitations of available electronic drive amplifiers. More importantly, the high frequency design and performance of the device has not been investigated.

The balanced bridge switch design is preferred over the directional coupler for several reasons. First, a balanced bridge design enables similar device design and characterization for both the modulators and switches if the interferometric type is chosen. Second, the fabrication dependent coupling length problem of the directional coupler design is avoided. The problem of increased device length for the balanced bridge switch due to the 3 dB coupling sections is somewhat mitigated since the design can be tailored for 1x2 and 2x1 operation. A 1x2 balanced bridge device would have one input waveguide and two output waveguides, while a 2x1 device would have two input waveguides and one output waveguide. The 1x2 and 2x1 designs only require one 3 dB coupling section each instead of the two required for the full 2x2 configuration. Third, both chirp-free and chirping operation are possible with the interferometer design. Chirp-free operation is not an option with the directional coupler design. Finally, the periodicity of the switching characteristic of the interferometric switch allows generation of modulated optical signals with frequency multiples of the electronic drive signal frequency. As mentioned earlier, a 5 Gb/s type pulse train may be generated using a 2.5 GHz sinusoidal drive signal with an amplitude of $2V_{\pi}$. The directional coupler does not have this capability.

2.4 Integration Issues

Having examined several modulator and switch designs in some detail, we will now turn to look at the problem of building up the OTDM system using those devices. There are two ways to go about constructing the system. The first choice is to fabricate separately and package the individual switches and modulators and link them together with fiber. The second alternative is to integrate the devices on a single substrate.

There are several problems associated with linking together individual devices with fiber patchcords. First, fiber to fiber optical insertion loss for a single packaged device can be from 5 to 7 dB. The transmitter consists of five stages and therefore the total loss of the transmitter block would be 25 to 35 dB!

Second, the lengths of the interconnecting fibers are important for operation at high bit rates. For a final output bit rate of 10 Gb/s, and assuming a fiber optical index of 1.44, each bit consists of a pulse of light about 2 cm long in the fiber. Therefore, to ensure proper re-multiplexing of the data streams, optical path lengths must be controlled to within a few millimeters. In addition, since the electro-optic devices are polarization sensitive, the polarization of the light must be maintained between the connected devices.

Finally, there is a concern with the coherence of the optical signals which are re-combined in the multiplexing stages. Since the optical waveforms generated by the sinusoidally driven switches are not perfectly rectangular in shape, there is some overlap between adjacent pulses. If the frequencies of the recombined signals differ by less than the information bandwidth, then detectable interference will occur in the overlapping regions of the pulses.

On the positive side, using individual devices allows easier characterization of the sub-blocks within the system, and enables the blocks to be moved around to investigate the performance of different configurations.

There are also several issues involved with integrating the devices on a single substrate. Typical individual electro-optic elements have lengths of about 1 to 1.5 cm each and therefore, a 7.5 cm long substrate must be available. Waveguide propagation losses must not be too large since the optical signals will travel several centimeters through the substrate. The waveguides must be designed to be single mode, provide good mode confinement, and have mode profiles well matched to the fiber mode profile at the substrate edge. The mode profiles of titanium diffused waveguides are a function of the diffusion parameters selected in the fabrication process [35]. These parameters include the pre-diffusion titanium width and thickness, the diffusion temperature, and the diffusion time. Models exist for calculating the theoretical mode profile based on the above parameters. However, waveguides with optimized mode profiles are usually determined experimentally. Published results indicate propagation losses around 0.5 dB/cm [36].

A second consideration for component integration is that waveguide bends are required for appropriate spacing of the switches and modulators. Discrete, circular, or s-shaped curves may be used, depending on their relative losses, and their length to width offset proportions. Discrete bends are perhaps the easiest to fabricate. However, since discrete bends are limited to perhaps 1 degree for acceptably low loss (<0.2 dB/bend), the length required for large adjacent spacing of components may become excessive. While more difficult to implement, circular and s-shaped bends can reduce the length required for a lateral offset.

A third factor influencing the layout is that switches and modulators must be spaced sufficiently far apart so that optical coupling and electrical crosstalk are acceptably low.

Optical coupling is basically eliminated with spacings of around 20-30 μm [14]. Electrical crosstalk, however, may require much larger component separation. Veselka et al. report electrical crosstalk down to -45 dB (electrical) for a 300 μm lateral spacing of directional coupler switches [37].

Fourth, a large number of components on a single substrate may introduce thermal problems. Since each switch or modulator typically requires from 0.2 to 1.0 W of power for complete switching. The heat generated by ten high powered elements on a single substrate would be substantial, and special cooling arrangements would likely be required. In addition, it is important that the substrate be kept at a uniform temperature since the properties of lithium niobate including the switching voltage are thermally dependent [35].

Finally, even though the devices are integrated on a single substrate, ensuring phase matching for constructive interference of the multiplexed signals may be a problem in the transmitter. The phases of the optical signals in a single modulator or switch can be matched or mismatched by tuning the bias voltage to the device. In the integrated approach, the phases of the optical signals at the multiplexing switches of the transmitter must be matched. Since the optical wavelength is 1.55 μm, it is unlikely that good phase matching can be obtained through matching waveguide path lengths. Therefore, phase modulators will probably be required in one of each of the paths of the optical inputs to the multiplexing switches. Referring back to Figure 1.2, the phase modulators could be inserted between switches 3a and 4a, 3c and 4b, and 4a and 5.

2.4.1 An Example Integrated Substrate Layout

To get an idea of how an integrated OTDM system might be laid out, an example single-substrate system was designed. The single-substrate system addressed the first three integration considerations in the previous section, and is shown in Figure 2.9. Lateral spacing of the devices is set to 250μm between the modulator elements to reduce

electrical coupling and to permit fiber attachment for the demultiplexing structure or for a two-stage multiplexer/modulator. Waveguide bends were designed according to the s-shaped curve proposed by Minford, Korotky, and Alferness [38]:

$$y(x) = \frac{h}{L}x - \frac{h}{2\pi}\sin\left(\frac{2\pi}{L}x\right) \tag{2.24}$$

where h is the lateral offset, and L is the length in the direction of propagation. The advantage of this type of curve is that its first and second derivatives are continuous, which will in theory reduce the bend losses. Using this formula, and keeping L^2/h to $1.5*10^5$ μm to keep losses acceptably low [22], the required lengths L_1 and L_2 in terms of the modulator separation h are:

$$L_1 = \sqrt{1.5*10^5\, h} \tag{2.25}$$

$$L_2 = \sqrt{1.5*10^5 \frac{h}{2}} \tag{2.26}$$

The total length is given by:

$$L_{total} = 2(L_1 + L_2) = 1322\sqrt{h}\ \mu m \tag{2.27}$$

For h=250μm, we can calculate L_{total} = 2.09 cm. Thus, with five elements lengthwise on a 7.5 cm circular substrate, the maximum element length can be about 1 cm if integration on a single wafer is to be achieved. If the structure is split into two sections just before the modulators, the elements may be as long as perhaps 2 cm. If the insertion loss of a pigtailed device is not excessive, this may be an acceptable alternative. As well, since the design of the OTDM receiver is identical to the initial three-switch pulse generation stage of the transmitter, no new design would be required for the receiver substrate. Furthermore, longer element lengths will permit lower drive voltages, and a two-part construction will allow easier monitoring of the finished device.

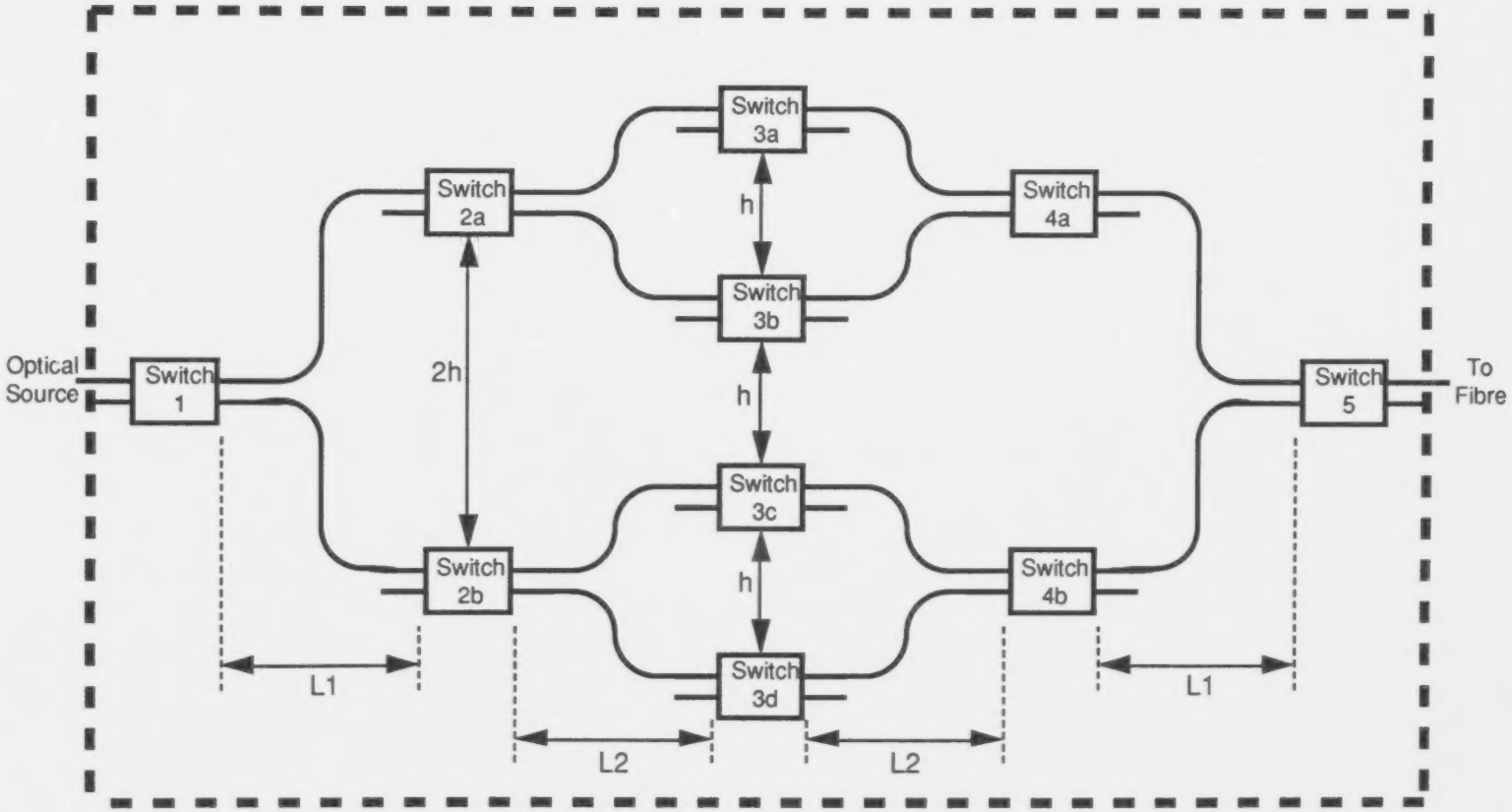

Figure 2.9 : Example Integrated OTDM Transmitter Substrate Spacing Requirements

Considering only the waveguide layout, the total width required on the substrate is only 750μm. With this relatively small width, even after making cutting and polishing allowances, several devices may be patterned on one substrate.

As noted in the previous section, however, a fairly sophisticated cooling circuit and packaging scheme would be required to meet the thermal stability requirements of a lithium niobate substrate. Providing adequate cooling may take up additional real estate on the wafer. In addition, insertion of three phase modulators for optical phase matching purposes would increase either the total length or width required for the integrated OTDM circuit.

2.5 Summary

In Chapter 2, we have investigated the theory behind the operation of the modulator and switch building blocks of the OTDM system. As well, the issues involved in integrating the devices to build up the more complex OTDM structure were discussed. The computer simulations which are presented in Chapter 3 are based directly on the theory examined in this chapter. These simulations are used to examine the performance of the OTDM system as a whole.

3.0 OTDM System Computer Simulations

The theoretical models for individual switch elements of the OTDM system were introduced in Chapter 2. However, we are also interested in the operation and behavior of the entire system of cascaded switch elements shown earlier in Figures 1.2 and 1.3. This section describes a computer model which was developed to examine such a system. The model was implemented using the Block Oriented Systems Simulator (BOSS) software package running on the SPARC 2 workstations at TR Labs. BOSS is a waveform based simulator, not a formula based analysis tool. This means that in BOSS simulations, waveforms are discretized and transferred between blocks which operate on waveform samples in the time domain.

Block diagrams of the system are located in Appendix 3A and are referred to throughout this chapter. The BOSS model permits analysis of the OTDM system optical and electrical waveforms as a function of several switch and modulator parameters. As well, a fiber model and a demultiplexer model similar in structure to Figure 1.3 are included to allow simulation of a complete transmission link.

In this chapter, we investigate the waveforms generated by the OTDM system as a whole. The effects of switch and modulator extinction ratios on the OTDM waveforms are examined. Simulations of the complete transmitter-fiber-receiver link are presented and the effects of fiber dispersion are discussed. Finally, operation of the OTDM system employing 2 V_π amplitude drive voltages for the final rate multiplexing and demultiplexing switches are considered.

3.1 Modelling Theory

Figures 3.1 and 3.2 display the block diagrams for the OTDM transmitter and receiver. As was discussed previously, blocks 1,2a,2b,4a,4b and 5 are optical switching,

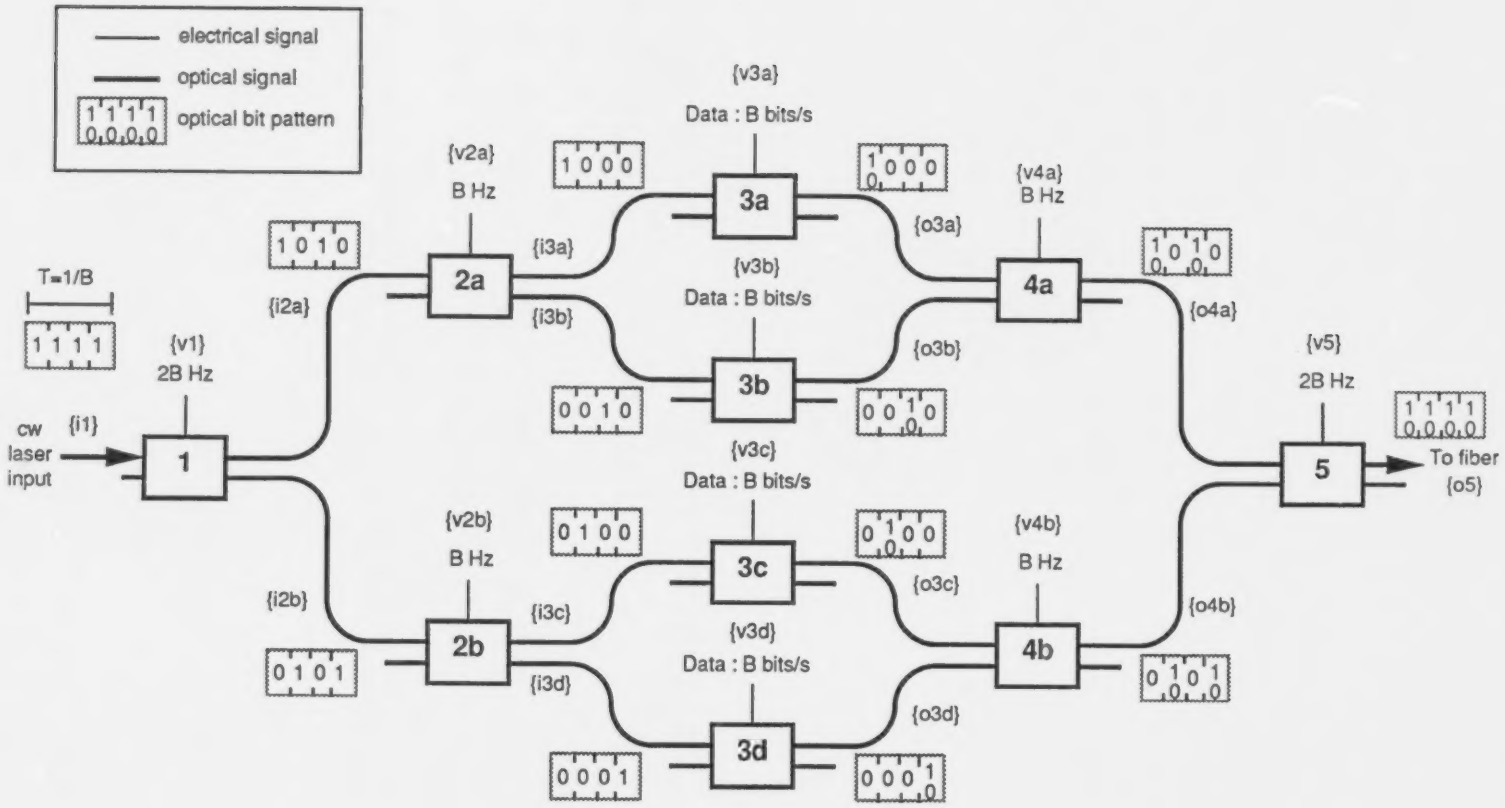

Figure 3.1 : Transmitter Block Diagram

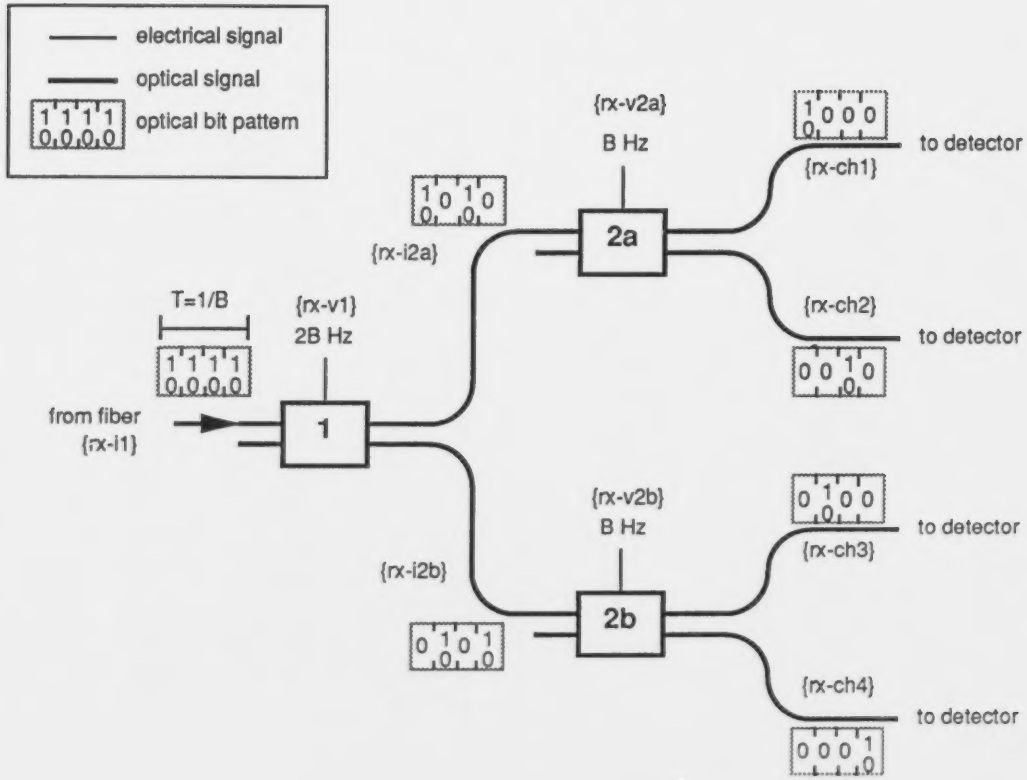

Figure 3.2 : Receiver Block Diagram

or multiplexing and demultiplexing elements, and blocks 3a-3d are optical modulating elements. The optical bit patterns are identified as before, and each signal is labelled with a name in parentheses (eg. {v3a}). These signal names correspond to the names used in the BOSS simulation blocks which will be presented later. The 'i' prefix denotes an optical input signal, and the 'o' prefix denotes an optical output signal. Electrical drive voltages are denoted with a 'v' prefix. The suffix of each name indicates the associated switch.

3.1.1 Switch and Modulator Models

For these simulations, the interferometric 2 x 2 switch model was chosen for both the switches and modulators. The transfer or crossover characteristic which describes the intensity transferred from one guide to the other in terms of the applied voltage is given by equation (2.10) :

$$\eta = \cos^2\left[\frac{\pi V}{2 V_\pi}\right]$$

where V_π is the required half-wave, or switching voltage, and V is the applied voltage. Thus, for an applied voltage of $V = V_\pi$, complete switching from one guide to the other takes place. In practice, perfect switching is not realized, and some finite crosstalk exists between the guides. In the BOSS model, the transfer characteristic was modified such that the crosstalk in either switching state was symmetric:

$$\eta = \chi + (1-2\chi)\cos^2\left[\frac{\pi V}{2 V_\pi}\right] \qquad (3.1)$$

where χ denotes the extinction ratio of the switch. Recall from Section 2.2.1.1 that the switching voltage V_π is the voltage required to achieve $\Delta\beta L=\pi$. V_π is a complex function of the physical waveguide and electrode structures, and also of the frequency of operation. Therefore, V_π in equation (3.1) refers to the switching voltage at the particular frequency of operation. Since the multiplexing and demultiplexing switches are driven at a single

frequency, V_π is a constant for these switches. The BOSS block representation of equation 3.1 was named MZI 2x2 SWITCH and is shown in Figure 3A.1 of Appendix 3A. In the Figure, the two optical inputs enter from the left hand side, while the two outputs exit from the right hand side. The electrical drive voltage is applied from the top.

The difference between the switch and the modulator is that the drive voltage applied to the modulator is not a sinusoidal signal, but a digital signal. The effective drive voltage applied to the modulator as a function of frequency must be modified by the H[f] rolloff characteristic as discussed in section 2.2.1.2. Thus the switching characteristic for the modulators was modified such that :

$$\eta = \chi + (1-2\chi)\cos^2\left[\frac{\pi V}{2 V_{\pi DC}} H[f]\right] \tag{3.2}$$

where,

$$H(f) = e^{(-\alpha L/2)}\left[\frac{\sinh^2\left(\frac{\alpha L}{2}\right) + \sin^2\left(\frac{\xi L}{2}\right)}{\left(\frac{\alpha L}{2}\right)^2 + \left(\frac{\xi L}{2}\right)^2}\right]^{\frac{1}{2}}$$

as determined in Chapter 2. Note that the switching voltage $V_{\pi DC}$ in equation (3.2) is the required switching voltage at dc, and not at some arbitrary frequency of operation.

Again, the BOSS block representation employed for the modulators was the same as that for the switches, and only the electrical drive signal to the modulators was altered. Figure 3A.2 in Appendix 3A contains the block diagram of the modulator signal generator which is composed of a data generator and the H[f] filter. In Figure 3A.2, the PN_SEQUENCE GENERATOR simply generates a sequence of TRUE and FALSE values with a sequence length of 2^7-1 bits. A sequence length of 2^7-1 was chosen to follow the requirements for the Synchronous Optical Network (SONET) optical transmission format. The LOGICAL TO NUMERIC block converts the TRUE and

FALSE values to 1 and 0 levels. The last part of the data generator is the DELAY block which allows an arbitrary delay to be introduced. This data sequence then passes through the rolloff function block H[f] which has the frequency characteristic of equation (2.15). The H[f] frequency response curve was calculated by a computer program written in 'C' and is included as listing 3B.1 in Appendix 3B. The microwave (N_m) and optical (N_o) indices used in calculating H[f] were 4.2 and 2.2, respectively. The assumed length of the device (LENGTH) was 1.0 cm, and the resistive losses of the electrodes (ALPHAo) were 1.0 dB/(cm $GHz^{1/2}$).

3.1.2 OTDM Transmitter Model

The modulator/multiplexer structure for the OTDM system was built up using the MZI 2X2 SWITCH elements. Figure 3A.3 in Appendix 3A contains the BOSS block diagram structure for the 4 CHANNEL ENCODER. The continuous wave optical input is applied from the left side, and the modulated four channel multiplexed optical signal exits from the right side. The drive signals to the switches and modulators are applied from inputs at the top and bottom. Optical outputs are also provided from each switch and serve as monitoring points.

The 4 CHANNEL ENCODER is a component of the larger 4 CHANNEL TRANSMITTER shown in Figure 3A.4. The transmitter includes the continuous wave, or dc laser source, the electronic drive signals for the switches and modulators, and data monitoring points.

3.1.3 OTDM Receiver Model

The demultiplexer is also built up from the MZI 2X2 SWITCH blocks. Figure 3A.5 in Appendix 3A shows the structure of the 4 CHANNEL DMUX. The received optical signal enters from the left side, and the four demultiplexed optical data streams

emerge from the right side. The electronic drive signals applied to the switches enter from the top and bottom.

The 4 CHANNEL RECEIVER as shown in Figure 3A.6 incorporates the 4 CHANNEL DMUX building block and adds the electrical drive signals for the switches and the data monitor points.

3.1.4 Fiber Model

As stated in the introduction, the modulation scheme adopted in this thesis attempts to minimize the spectral width of the transmitted signal by externally modulating the carrier, as opposed to modulating the laser source directly. The reason for this was to minimize the dispersive effects of standard fiber which has a dispersion minimum at around the 1300μm wavelength. Using external modulation, the spectrum of the transmitted or modulated signal is determined by convolving the cw laser spectrum with the data spectrum. If the laser source spectrum is much wider than the imposed information spectrum, then the spectral width of the transmitted signal will be on the order of width of the laser spectrum. On the other hand, if the information bandwidth is much greater than the source bandwidth, the spectral width of the transmitted signal will be on the order of the width of the information spectrum.

Since we were interested in minimizing the spectral width of the transmitted signal it was assumed that the width of the continuous wave laser spectrum is negligible compared to that of the imposed information. Therefore, the fiber dispersion model implemented here assumed that the spectral characteristics of the transmitted signal are determined solely by that imposed information. The experimental setup to be described later in Chapter 4 used a distributed feedback laser with a 3 dB spectral width of approximately 150 MHz. This linewidth was in fact almost negligible compared with the 10 GHz bandwidth of the information being transmitted. Fiber attenuation was considered to be a constant over the

1.55 μm transmission window, and was omitted from the model since it affects only the relative amplitude of the signals and does not change the pulse shapes. If a noise model or other fixed amplitude process is incorporated into a future version of the system, then fiber attenuation effects should be included.

With the above assumption that the optical spectral characteristics were identical to those of the the baseband data signal, fiber dispersion was modelled using the dispersion equation for standard fiber with a dispersion minimum at the 1300 nm wavelength. The dispersion experienced by a spectral component at wavelength λ is given to second order by [39]:

$$D = \sqrt{\left(\frac{d\tau}{d\lambda}\right)^2 + \frac{1}{2}\beta^2\left(\frac{d^2\tau}{d\lambda^2}\right)^2} \qquad (3.3)$$

where λ is the wavelength, β is the source spectral width, and τ is the wavelength group delay given by:

$$\tau(\lambda) = a + b\lambda^2 + c\lambda^{-2} \qquad (3.4)$$

For standard dispersive fiber with a dispersion minimum at 1300 nm:

a=-34.68 ns/km,
b=10.504 ns/(km μm^2)
c=29.988 (ns μm^2)/km.

If the operating wavelength is assumed to be around 1.55 μm, and the laser source is assumed to have a linewidth less than 0.1 nm, we may neglect the second order dispersion term. With this simplification, the dispersion is linear with respect to wavelength around the 1550nm wavelength, and expression (3.3) becomes:

$$D = \frac{d\tau}{d\lambda} = 2b\lambda - 2c\lambda^{-3} \qquad (3.5)$$

The units of D are often expressed in ps/(km nm) since units of km and nm are convenient units for fiber and wavelength respectively. Evaluating the fiber dispersion for a 1550 nm operating wavelength using the silica fiber constants specified above we obtain D = 17 ps/(km nm).

Elrefaie's derivation of the phase distortion due to fiber dispersion [39] is reproduced below in equations (3.6) to (3.9). The absolute delay in the fiber experienced by an optical signal with frequency ν is:

$$\tau(\nu) = \tau(\nu_c) + (\nu - \nu_c)\frac{d\tau}{d\nu}L$$

$$= \tau(\nu_c) + (\nu - \nu_c)\frac{d\tau}{d\lambda}\frac{d\lambda}{d\nu}L$$

$$= \tau(\nu_c) + (\nu - \nu_c)\, D\, L\frac{\lambda^2}{c} \qquad (3.6)$$

where ν_c is the optical carrier frequency and L is the fiber length.

The optical phase $\phi(\nu)$ is given by :

$$\phi(\nu) = 2\pi\int_0^{\nu} \tau(\nu')\ d\nu'$$

$$= 2\pi\nu\tau(\nu_c) + 2\pi DL\frac{\lambda^2}{c}\left[\frac{(\nu - \nu_c)^2}{2} - \frac{(\nu_c)^2}{2}\right] \qquad (3.7)$$

and the relative phase difference introduced between the carrier and any other frequency is :

$$\Delta\phi(\nu) = \phi(\nu) - \phi(\nu_c) = \pi DL\frac{\lambda^2}{c}(\nu - \nu_c)^2 \qquad (3.8)$$

As stated earlier, the relative phases between the information spectral components are the same at the carrier frequency as they are at baseband. Therefore, we may calculate

the relative phase shift of the information spectral components due to dispersion at the optical frequency, and apply the same relative phase shifts to the spectral components of the baseband signal to obtain the dispersed signal envelope. The constant delay term, or the equivalent linear phase term, was omitted from the model since only the relative phase difference contributes to signal distortion. The distortion producing baseband transfer function of the fiber is therefore given by:

$$H_{fiber}(f) = e^{-j\,\Delta\phi(\nu)} = \exp\left[-j\pi DL\frac{\lambda^2}{c} f^2\right] \qquad (3.9)$$

where $f = \nu - \nu_c$

The BOSS model for the fiber is simply a filter with unity magnitude response and phase response calculated according to equation (3.9). Figure 3A.7 in Appendix 3A contains the block diagram for the FIBER MODEL. Note that since the transmitter and receiver operate on the intensity of optical signals, the FIBER MODEL also expects an optical intensity signal as input. For the dispersion calculations, the electric field is required, and this is calculated by taking the square root of the input intensity signal. After multiplication with the fiber transfer function $H_{fiber}[f]$, the dispersed output intensity signal is obtained by squaring the magnitude of the electric field. The $H_{fiber}[f]$ frequency response is calculated by a computer program written in 'C' and is included as listing 3C.1 in Appendix 3C. The computations were performed using a 1550nm carrier wavelength and a fiber dispersion constant of D = 17 ps/(km nm).

3.1.5 OTDM Link Model

The complete OTDM system model is composed of the 4 CHANNEL TRANSMITTER, FIBER MODEL, and 4 CHANNEL RECEIVER blocks. Figure 3A.8 in Appendix 3A contains the BOSS representation of the system and is named OTDM SYSTEM. Monitor points are provided at both the transmitter and receiver for each of the four data channels.

3.2 4 Channel Transmitter Simulation Overview

To illustrate the operation of the model, this section steps through the functioning of the 4 CHANNEL TRANSMITTER in detail for a particular set of device parameters and particular data streams to encode and multiplex. This example assumed that all switches and modulators operated with a 15 dB extinction ratio. It was assumed that the switches were driven at the full V_π switching voltage required for operation at the particular frequency of operation. Each of the four modulators encoded data at a rate of 2.48832 Gb/s, for a final multiplexed data rate of 9.95328 Gb/s. The modulators were driven with four independent 2^7-1 pseudo-random bit sequences.

The modulator and switch bandwidth determining parameters were chosen to be consistent with the examples provided in Chapter 2. The device interaction length was assumed to be 1 cm, and the microwave and optical refractive indices were assumed to be 4.2 and 2.2, respectively.

The BOSS system used for this simulation example was the 4 CHANNEL TRANSMITTER OVERVIEW system shown in Figure 3A.9 of Appendix 3A. It differs slightly from the 4 CHANNEL TRANSMITTER of Figure A.4 in that monitor points were provided for the optical outputs of each switch or modulator.

We will now proceed step by step through the functioning of the transmitter and examine the optical and electrical waveforms at each point in the system. The signal names referred to throughout this section correspond to those introduced earlier in Figures 3.1 and 3.2. Figure 3.3 shows the continuous wave laser light intensity envelope {i1} which is the input to switch 1 of the transmitter. Switch 1 is driven by the electrical sinusoidal signal {v1} which has amplitude V_π and a frequency of twice the bit rate, or 4.976 GHz. Figure 3.4 shows the optical intensity waveforms {i2a} and {i2b} obtained at the two output ports

of switch 1.

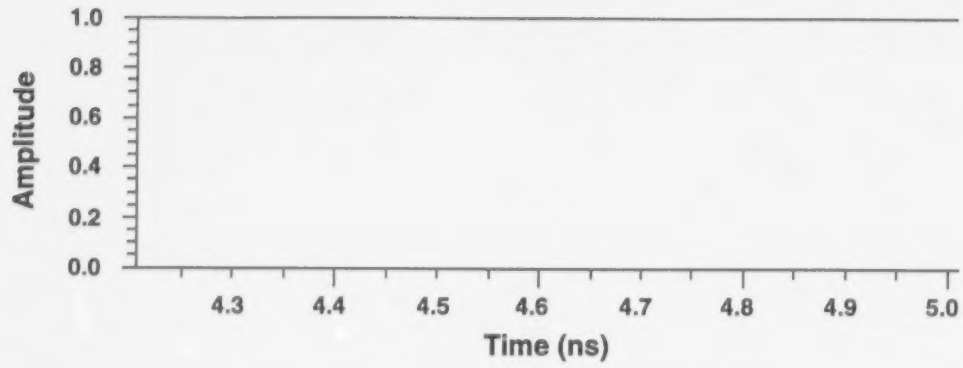

Figure 3.3 : Simulated Waveform {i1}

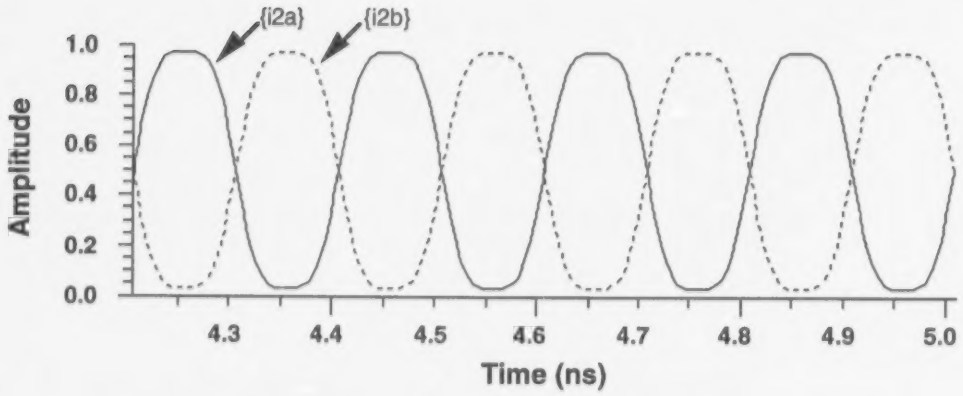

Figure 3.4 : Simulated Waveforms {i2a} and {i2b}

The vertical axis represents the light intensity normalized to the input intensity, and the horizontal axis represents time. Figure 3.4 displays two 4-pulse frames for a total of eight pulses. Signal {i2a} contains pulses in slots 1 and 3 of each of the two frames, and signal {i2b} contains pulses in slots 2 and 4. These patterns are also indicated on the output branches from switch 1 in Figure 3.1.

Switches 2a and 2b further demultiplex the two pulse streams into four time-interleaved streams. Switches 2a and 2b are driven with the electrical signals {v2a} and

{v2b} which have amplitudes of V_π and frequencies of 2.488 GHz. The phases of the elecrical signals are set to match up the peaks of the electrical signal with the peaks of the incoming optical pulse streams. Figure 3.5 shows the optical intensity signal {i3a} at the input to modulator 3a, and Figure 3.6 overlays the intensity inputs to all four modulators. Notice that the pulses to the four modulators are interleaved in time. As well, note that the cascading of the finite extinction ratio switches reduces the peak intensity of the pulses during the '1' slot, and increases the minimums in the '0' slots.

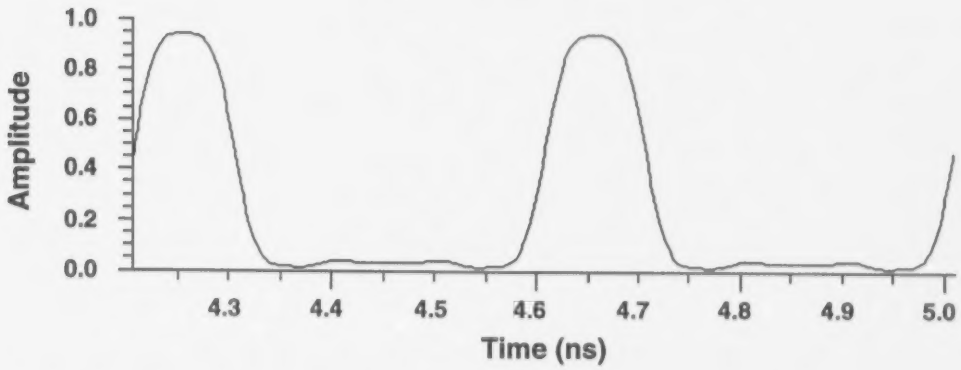

Figure 3.5 : Simulated Waveform {i3a}

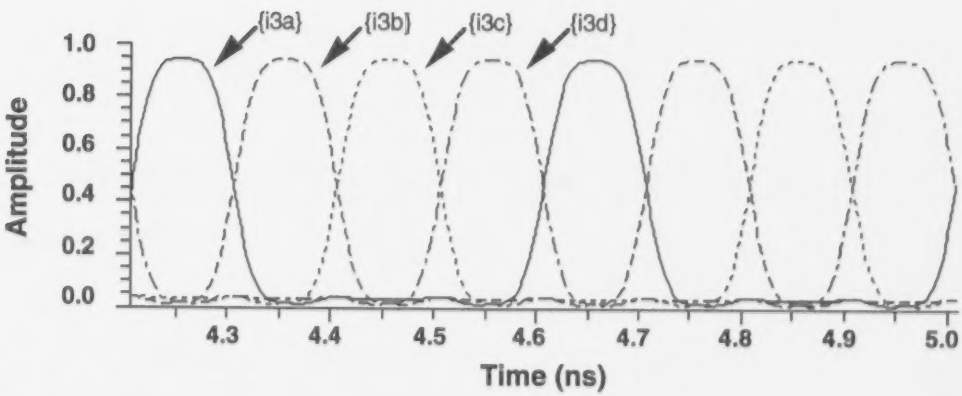

Figure 3.6 : Simulated Waveforms {i3a}, {i3b}, {i3c}, and {i3d}

Moving on to the modulator section, Figure 3.7a shows the modulator drive voltage {v3a} applied to modulator 3a. The waveform shown is two full bit periods in length, with a partial '1' followed by a complete '0', followed by another partial '1'. This waveform represents the effective drive voltage waveform applied to an ideal modulator with flat frequency response.

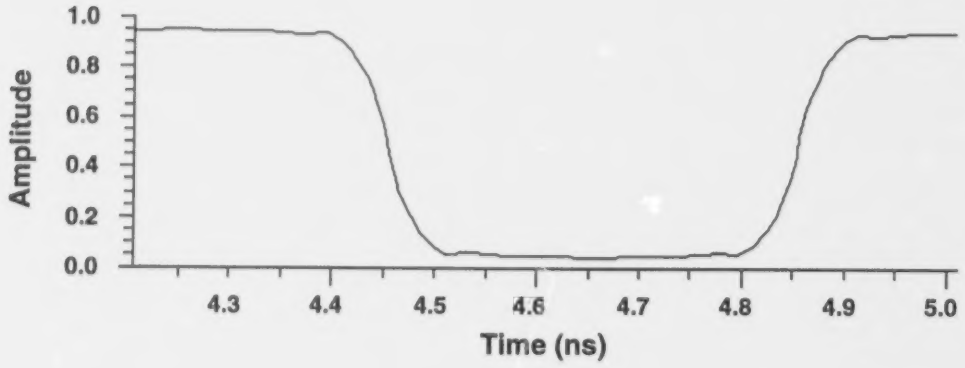

Figure 3.7a : Simulated Waveform {v3a}

Notice that the drive signal is shifted in time so that the centers of the data bits are located at the same time position as the peaks of the incoming optical pulses of Figure 3.5. The power spectrum of the data signal is displayed in Figure 3.7b.

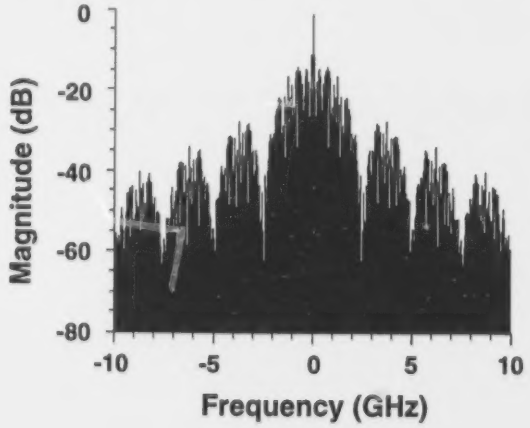

Figure 3.7b : Power Spectrum {v3a}

The spectral plot in Figure 3.7b is a simulation result. The same result can be arrived at analytically and is given by the power spectrum of the ideal data signal X[f] multiplied by the velocity mismatch and attenuation loss function of the modulator H[f]:

$$X_{effective}[f] = X[f]\, H[f]$$

where,

$$X[f]= \frac{A^2}{M}\left(\frac{\sin \pi fT}{\pi fT}\right)^2 \sum_{k=-\infty}^{\infty} \delta\left(f-\frac{k}{TM}\right) \quad [1] \qquad (3.10)$$

A is the amplitude scaling factor, T is the bit period, M is the length of the pseudo-random sequence, and H[f] is given by equation (2.15). From equation (3.10) we can see that the spectrum is composed of discrete spectral lines with frequency spacing 1/TM following the envelope of $\text{sinc}^2(\pi fT)$. Excluding the dc component, the minimum frequency component of the signal is given by $f_{min}=1/TM$.

Plots for the 3 remaining drive voltages are shown in Figures 3.8 to 3.10. The bit patterns are '11' on {v3b}, '01' on {v3c}, and '11' on {v3d}. Figure 3.11 displays overlaid plots of the optical intensity outputs from the four modulators. Notice that the data applied to each modulator have been correctly impressed on each of the outputs.

The four encoded 1/4 duty cycle bit streams are then multiplexed by switches 4a,4b, and 5. Switches 4a and 4b are driven with the electrical signals {v4a} and {v4b} which have amplitudes of V_π and frequencies of 2.488 GHz. The phases of the electrical signals are set to align the peaks of the electrical signals with the peaks of the incoming

---

[1] The power spectral density of a pseudo-random bit sequence of arbitrary length can be determined using autocorrelation analysis. A short derivation of equation (3.10) is included in appendix 3D.

modulated optical pulse streams. Figure 3.12 shows the optical output intensity signals {o4a} and {o4b} from switches 4a and 4b. Switch 5 is driven with the electrical signal

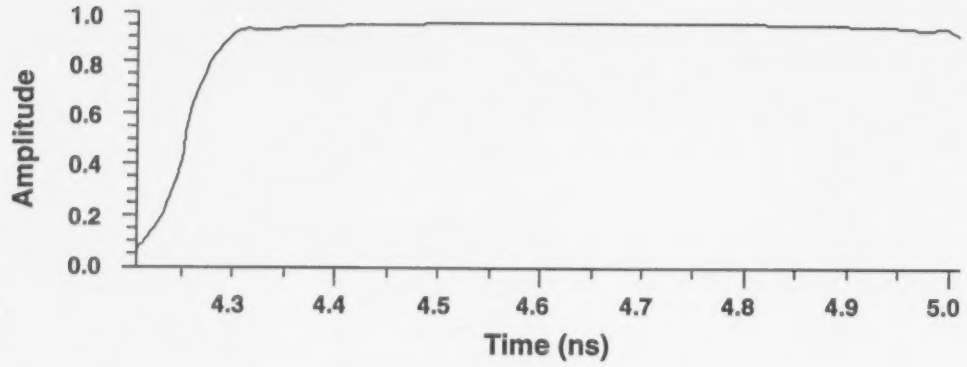

Figure 3.8 : Simulated Waveform {v3b}

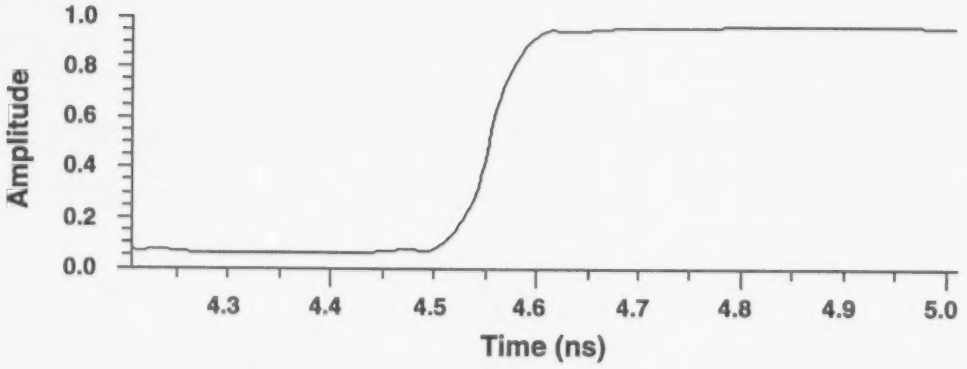

Figure 3.9 : Simulated Waveform {v3c}

{v5} which has an amplitude of V_π and a frequency of 4.976 GHz. The final multiplexed bit stream {o5} is shown in Figure 3.13 and a larger window of the {o5} signal is presented in Figure 3.14.

Note, that although the input data streams were true non-return-to-zero (NRZ) signals, the multiplexed output signal is no longer of that form. Instead, the signal has

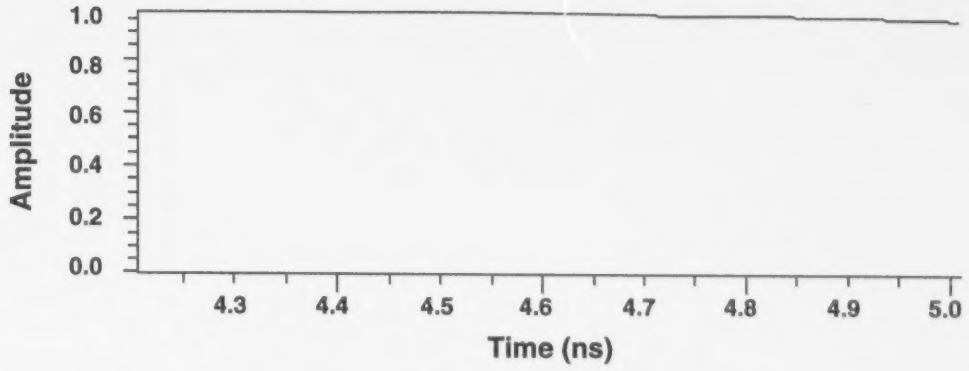

Figure 3.10 : Simulated Waveform {v3d}

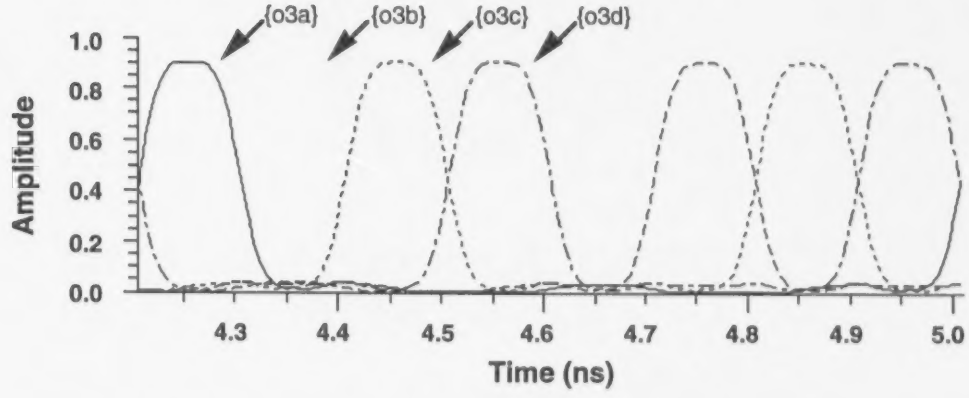

Figure 3.11 : Simulated Waveforms {o3a}, {o3b}, {o3c}, and {o3d}

been converted to a quasi-return to zero format. This effect is caused by the multiplexing action of switches 4a, 4b, and 5. The excess light is switched out of the system by way of the second optical outputs of each switch. Also, the cascaded effect of the 15 dB switch extinction ratio can be clearly seen now as it reduces the logical '1' level from the original unity to around 0.85. In addition, the logical '0' level is decidedly non-zero. The effects of switch extinction ratio will be explored further in the next section.

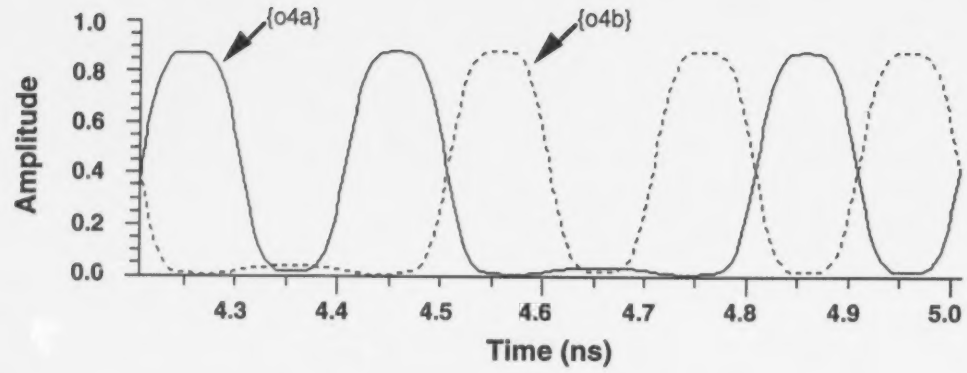

Figure 3.12 : Simulated Waveforms {o4a} and {o4b}

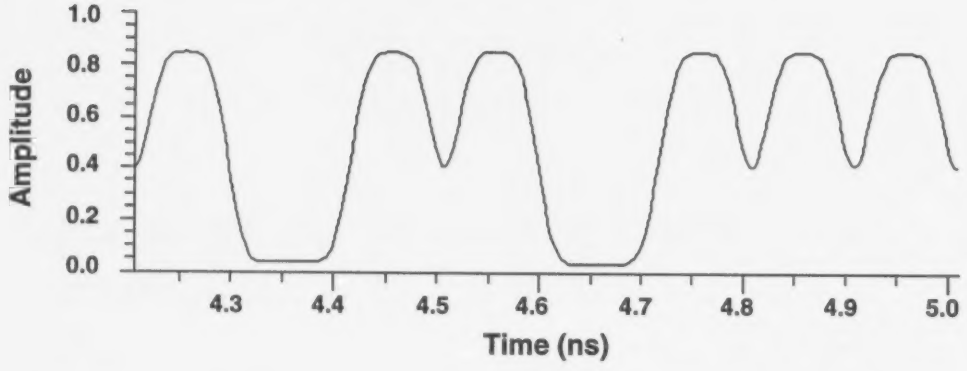

Figure 3.13 : Simulated Waveform {o5}

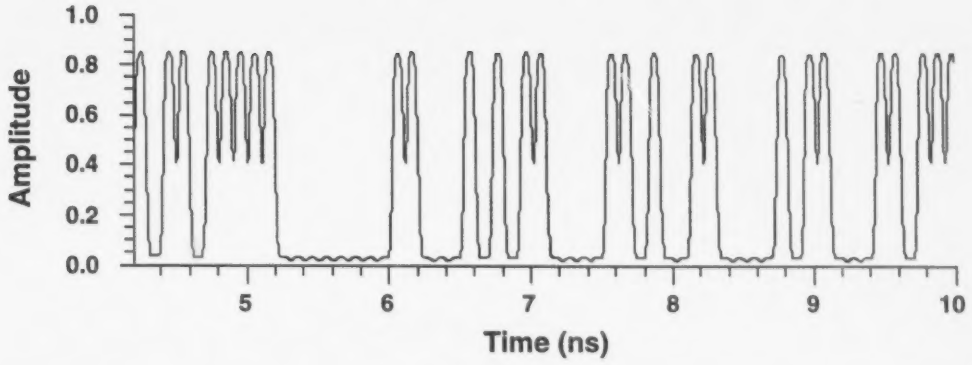

Figure 3.14 : Simulated Waveform {o5}

Figure 3.15 presents the {o5} waveform result from Figure 3.14 in the form of an eye diagram.

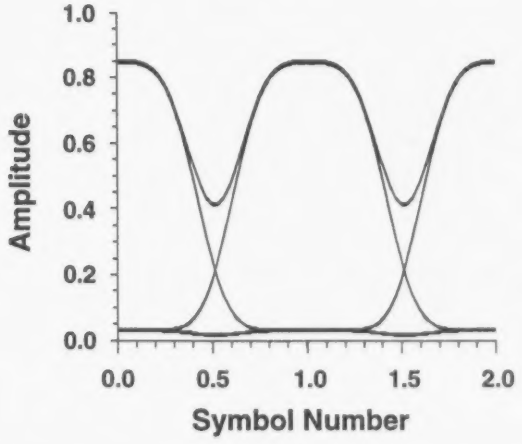

Figure 3.15 : Simulated Eye Diagram {o5}

Again, we can see the quasi-RZ format clearly, and observe the eye closure due to the finite extinction ratio. The baseband spectral content of the {o5} signal is shown in Figure 3.16.

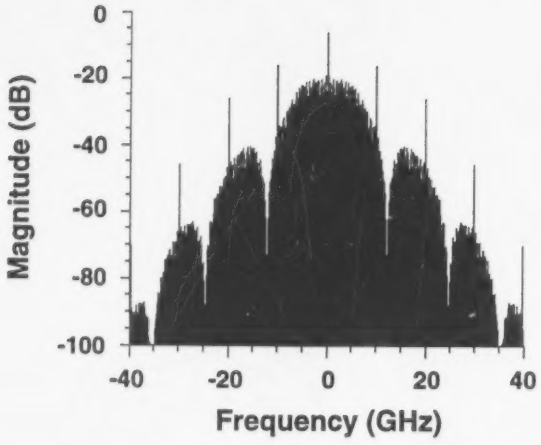

Figure 3.16 : Power Spectrum {o5}

As one might expect, the quasi-RZ characteristic shows up in the frequency content of the signal as spectral spikes at multiples of the output 9.95328 GHz bit rate. This slight RZ characteristic of the output signal may be useful in clock recovery at the receiver.

This concludes the overview of the example using the BOSS transmitter model. In the next several sections, simulations dealing with more specific aspects of the system will be presented.

3.3 Extinction Ratio Simulations

The extinction ratio parameter as defined here refers to the optical intensity crosstalk in the switches, or the optical intensity leakage in the off state of the modulators. It is defined as the ratio of the maximum intensity to the minimum intensity at the output of the modulator or switch. As stated previously, the simulations here assumed equal extinction ratios for the 'on' and 'off' states. However, due to fabrication sensitivity and structural differences between the switch and modulator components, in practice the extinction ratios may well be somewhat different for the 'on' and off' states, and the extinction ratios will vary somewhat from device to device.

Eye diagrams were generated for the optical intensity signal at the output of stage 5 using switch/modulator extinction ratios of ∞, 25 dB, 15 dB, and 10 dB. The eye patterns are overlaid in Figure 3.17. The vertical axis scale is normalized to the input optical intensity, and the horizontal axis is the normalized symbol number.

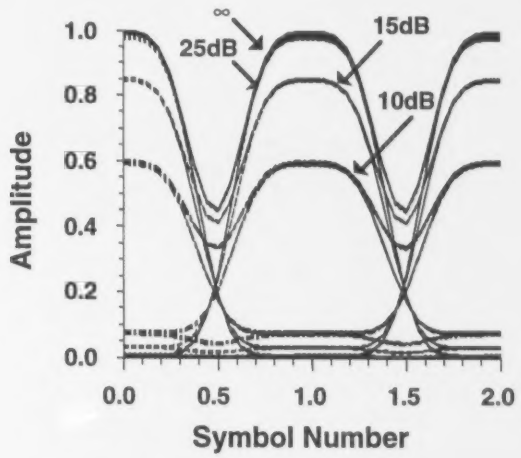

Figure 3.17 : Eye Diagram vs. Extinction Ratio

Examining the infinite extinction case result from Figure 3.17, we see that the peak normalized optical intensity is unity for a transmitted 1, and the minimum intensity is zero for a 0, as we would expect. For the finite extinction ratio cases we see that the effect of lowering the extinction ratio is to lower the peak intensity and raise the minimum intensity in the eye diagram. This effective eye closure is summarized in Table 3.1.

extinction ratio(dB)	normalized maximum	normalized minimum	normalized eye height
∞	1.00	0.00	1.00
25	0.99	0.005	0.985
20	0.95	0.01	0.94
15	0.85	0.03	0.82
10	0.60	0.07	0.53

Table 3.1 : Extinction Ratio Impact on OTDM Eye Closure

3.4 OTDM System Simulations With Fiber Dispersion

The impact of fiber dispersion was briefly investigated to observe the signal eye degradation as a function of conventional fiber transmission distance. Ideally, we would like to know at what distance the bit error rate rises above some established threshold level. However, the answer to this question depends on the receiver noise characteristics and for simplicity we will deal exclusively with the received optical eye pattern for now. Chapter 4 will explore bit error rates and noise for the OTDM system in a more quantitative manner. The measure of signal degradation used here is simply the optical eye closure relative to the zero transmission distance eye.

The system was simulated using four electrical input channels at bit rates of 2.48832 Gb/s each. The extinction ratio of the switches and modulators was set to 15 dB. Attenuation of the signal due to fiber losses was not considered, since the relative geometry of the eye diagram is in principle not affected by these losses. Figures 3.18a-3.18f display the received optical eye diagrams for channel 1 {ch1 out} for transmission distances of 0 to 100 km in steps of 20 km. Table 3.2 summarizes the approximate eye closure as a function of distance.

Distance (km)	Normalized Eye Height	Eye Closure (dB)
0	0.76	0.0
20	0.83	0.4
40	0.55	-1.4
60	0.43	-2.5
80	0.23	-5.2
100	0.09	-9.3

Table 3.2 : Dispersion Impact on OTDM Eye Closure

The Figures indicate that the eye becomes closed by 3 dB after about a 60 km transmission distance. The degradation of the eye diagram results from intersymbol

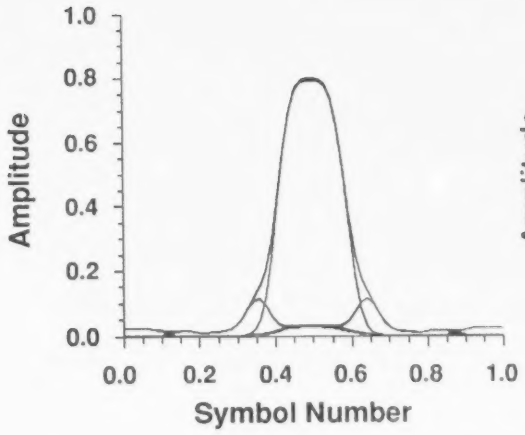

Figure 3.18a : 0 km Eye

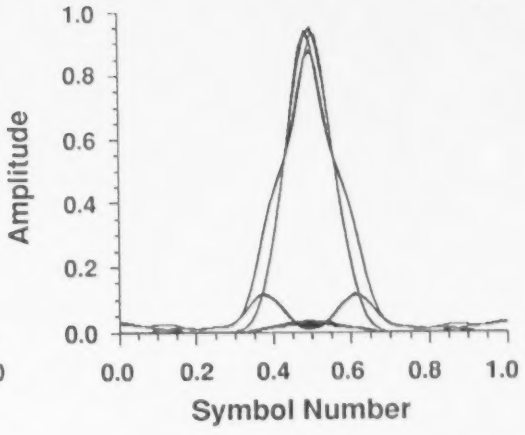

Figure 3.18b : 20 km Eye

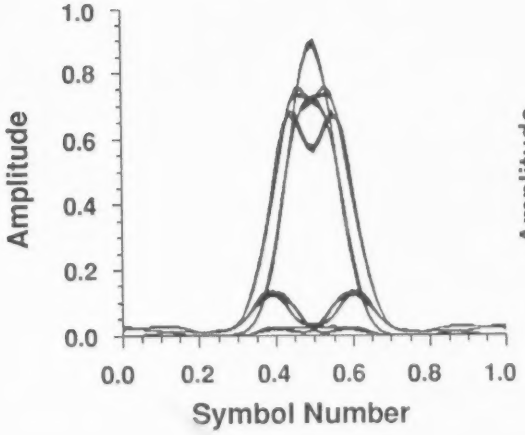

Figure 3.18c : 40 km Eye

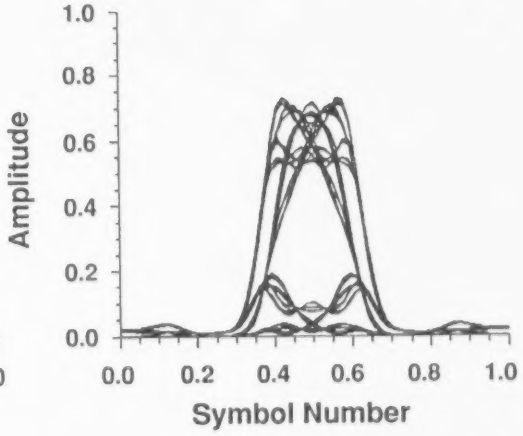

Figure 3.18d : 60 km Eye

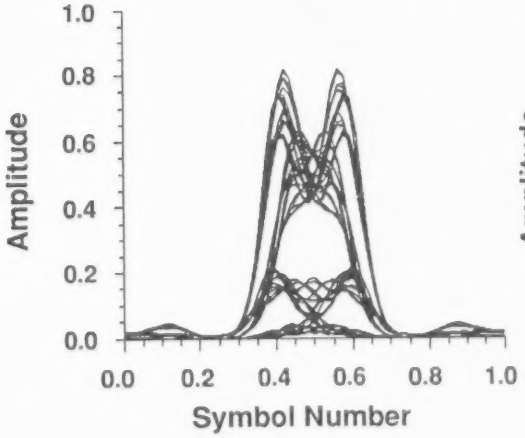

Figure 3.18e : 80 km Eye

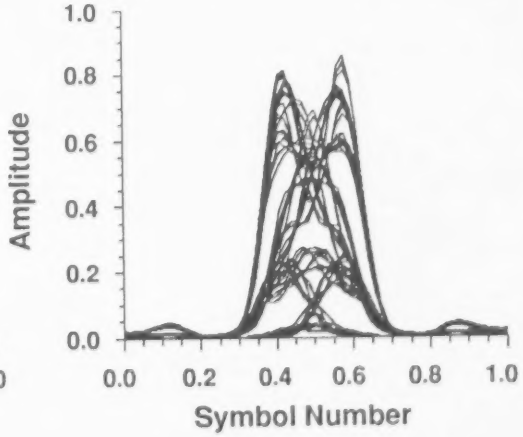

Figure 3.18f: 100 km Eye

interference as the pulses of the composite OTDM signal are spread out further and further with increased transmission distance. Later, Chapter 5 will re-examine the effects of dispersion on OTDM pulses and compare the BOSS simulated waveforms with experimental results.

3.5 OTDM System Operation Using $2V_\pi$ Switching

The switches used in the experimental system were of the balanced bridge interferometric variety. As suggested in Section 2.3.1, the periodic switching behavior of this type of switch can be exploited to generate optical pulse streams at multiples of the electrical drive signal frequency by simply increasing the drive signal amplitude. This section will briefly present simulation results obtained by using this concept in the OTDM system.

The 2 V_π switching technique was demonstrated using the standard OTDM model. Only the sinusoidal drive signals applied to switches 1 and 5 were altered. Switch 1 was driven by the electrical signal {v1} which was modified to have an amplitude of 2 V_π and a frequency of 2.488 GHz. Recall that previously, the {v1} signal had an amplitude of V_π and a frequency of 4.976 GHz. Figure 3.19 shows the {v1} drive signal which had the bias level set to zero.

This type of drive signal applied to switch 1 produced the optical 5 Gb/s pulse streams as shown in Figure 3.20.

Notice that the 2 Vπ switching creates a wide pulse stream {i2a} and a narrow pulse stream {i2b}. The {i2a} pulse stream is created by the slowly varying maximum and minimum points of the drive signal, and thus the pulses are wide. The {i2b} pulse stream is created by the more rapidly sloped zero crossings of the drive signal and so the pulses are narrow.

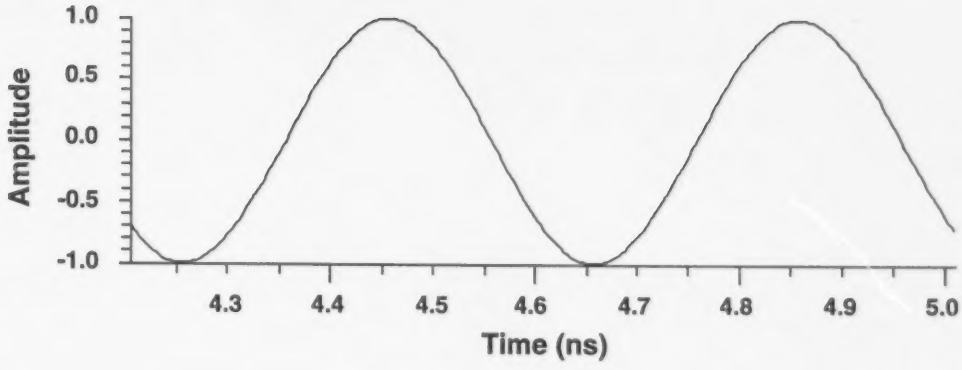

Figure 3.19 : Simulated 2 V_π Drive Signal {v1}

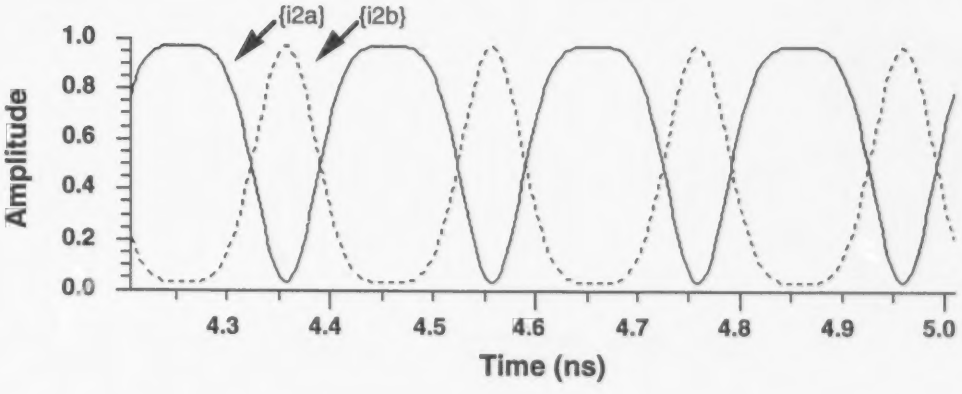

Figure 3.20 : Simulated Waveforms {i2a} and {i2b}

The second, third, and fourth banks of switches operate as previously described, and the waveform patterns are not included here. The pulse differentiation is reversed by operating switch 5 to gate the wide pulses with the zero crossings of the drive signal, and gate the narrow pulses with the extremities of the drive signal. Figure 3.21 shows the {v5} drive signal applied to switch 5.

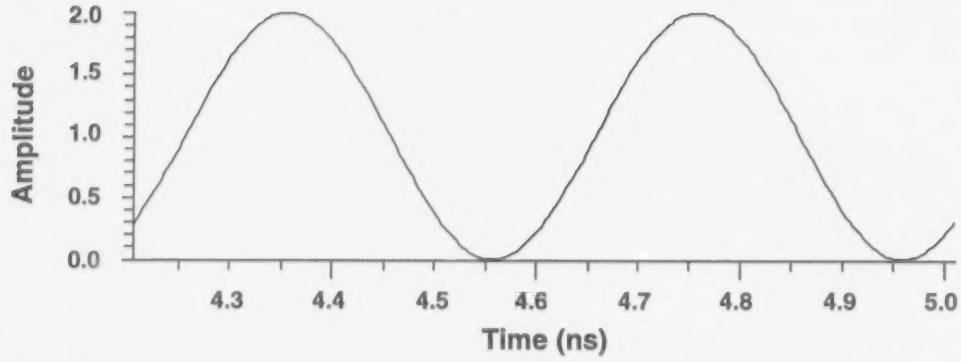

Figure 3.21 : Simulated 2 V_π Drive Signal {v5}

To multiplex the signals properly and reverse the pulse shape differences, the drive signal bias level is shifted to 1. In addition, the phase of the {v5} drive signal is adjusted to line up the zero crossings with the wide optical pulse stream. Figure 3.22 shows the multiplexed signal at the output of switch 5.

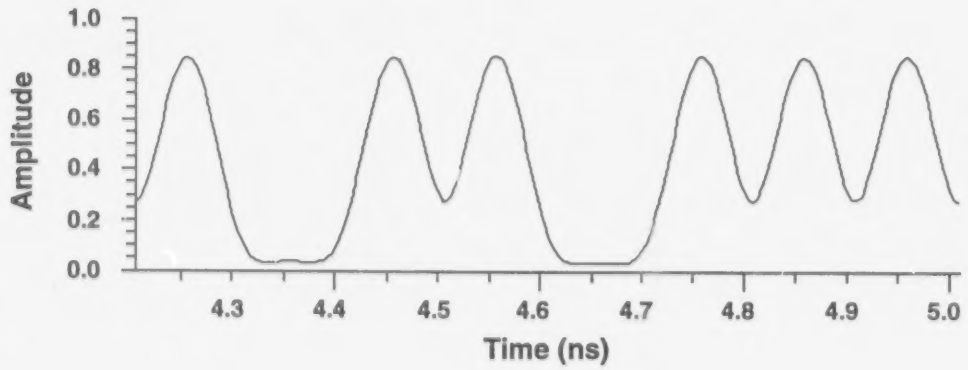

Figure 3.22 : Simulated Waveform {o5}

With the proper bias, amplitude, and phase adjustment to {v5}, similar pulse shapes are produced on all four channels. Comparing Figures 3.13 and 3.22, we can see that the pulse shape for the 10 Gb/s output signal has changed significantly by introducing

2 V_π switching at the first and last switching stages. Figure 3.23 shows this as well in the form of an eye diagram for the {o5} optical signal.

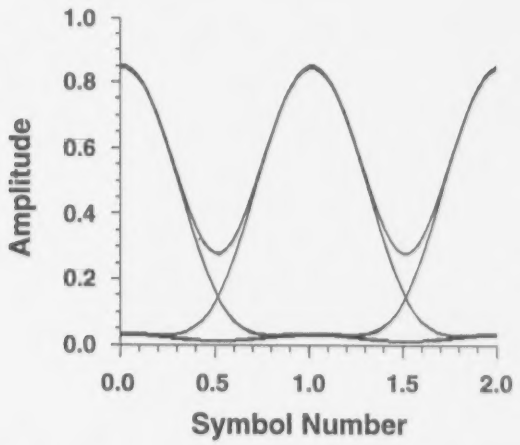

Figure 3.23 : Simulated Eye Diagram {o5}

Comparing Figures 3.15 and 3.23, we note that 2 V_π switching narrows the data pulses somewhat and slightly increases the return-to-zero characteristic of the composite OTDM signal. Chapter 5 presents experimental results obtained using the 2 V_π switching technique in the OTDM system and compare them with the analogous simulation results.

3.6 Summary

In Chapter 3, we have presented the BOSS computer simulations used to model the operation of the OTDM system. The modelling theory was presented first along with the BOSS block diagrams of the system. An overview of the simulations was presented, and the optical and electrical waveforms were examined at selected points in the OTDM model. The impacts of both switch extinction ratios and fiber dispersion on the eye diagram were examined. Finally, simulations of the OTDM system utilizing 2 V_π switching in the first and last switching stages were discussed. In Chapters 4 and 5, we will move on to

examine the OTDM experimental set up and results and make comparisons with the simulation results wherever possible.

4.0 OTDM Experimental Setup and Component Analysis

In Chapter 3, we examined the operation of the OTDM system using computer simulations. The purpose of this chapter is to describe and characterize the experimental setup used to implement the system physically. First, an overview of the general system will be presented, along with a discussion of the factors which determined the choice of the experimental design. The rest of this chapter will concentrate on the component characteristics of the optical source, the OTDM transmitter, and the OTDM receiver along with their impact on the OTDM system as a whole.

4.1 Selecting the OTDM Implementation

Earlier, section 2.4 discussed two methods for implementing the OTDM structure. One option considered was to obtain individual modulators and switches and link them together with fiber patchcords. The other option was to integrate the entire transmitter and receiver configurations on single substrates.

The discrete component approach was selected to demonstrate the OTDM concept for several reasons. First, the cost of designing and fabricating the integrated versions of the opto-electronic circuits was found to be prohibitively expensive. Second, the four channel OTDM concept can be demonstrated to a satisfactory degree with only five switching elements. The exact switch configurations to accomplish this will be described later in Chapter 5. Third, the discrete approach allows the switches to be disconnected and re-arranged. In a laboratory environment, this modular capability is valuable since it provides a cost effective way to investigate many topics involving electro-optic modulation and switching.

As indicated in section 2.4, there are several problems associated with the discrete approach which must be resolved. A major concern is that the insertion loss of 5 to 7 dB

for the individual switches is relatively high. For demonstration purposes, the transmitter and receiver will employ at most five concatenated switches, and thus the total excess loss in the link may be as high as 35 dB. These extreme losses will limit the transmission distances possible, even with the use of erbium-doped fiber amplifiers to boost the optical signal. While this discrete approach would not be practical for commercial systems, the laboratory objective of showing the functioning of the OTDM system should still be possible in spite of these losses.

The second problem involves controlling the optical path lengths. As mentioned earlier, the 10 Gb/s OTDM system requires variable optical path delays to ensure proper time-interleaving in the multiplexing process.

Finally, there is a concern with the coherence of the optical signals which are re-combined in the multiplexing stage. Since the optical waveforms are not perfectly rectangular in shape, there is some overlap between adjacent pulses. If the frequencies of the recombined pulse streams are the same, or differ by less than the information bandwidth, then detectable interference will occur in the overlapping regions of the pulses. These problems and potential solutions will be discussed in more detail as the experimental setup is detailed in the subsequent sections.

4.2 OTDM Implementation Overview

Figure 4.1 shows the general block diagram of the experimental setup. This high level structure is common to all the experimental work conducted using the OTDM system. The OTDM transmitter takes as inputs a continuous wave optical signal, a 2.5 GHz clock signal, and a 2.5 Gb/s data signal. The OTDM transmitter encodes the data optically and multiplexes it with three other 'dummy' data streams. In the experimental work presented here, only one of the four data channels is actually used to transmit data. The resulting pseudo-10 Gb/s OTDM signal is then sent through the fiber medium. The OTDM receiver

optically demultiplexes the true data channel from the three other channels and converts the optical signal back into an electrical signal. The bit error rate test set compares the transmitted data stream with the received data stream to determine the error rate performance of the link.

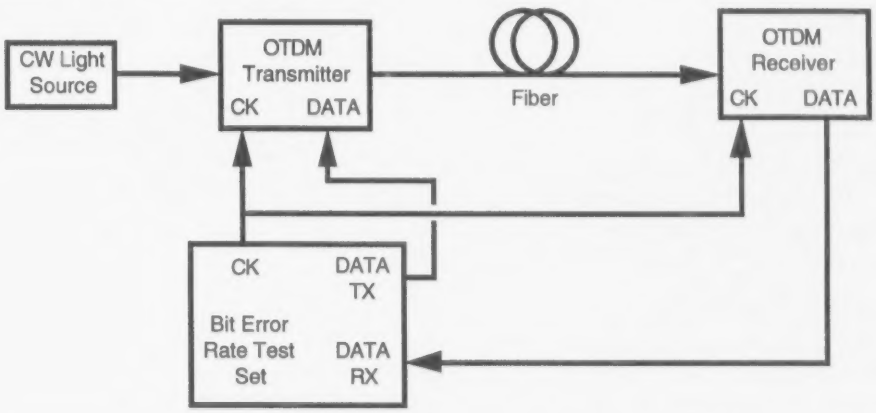

Figure 4.1 : OTDM Experimental System Block Diagram

To provide a framework in which to analyze the individual components of the system, more specific configurations of the OTDM optical source, transmitter, and receiver sub-blocks will be considered in the subsequent sections of this Figure. Section 4.3 will investigate the characteristics of the optical source. Section 4.4 will present a specific arrangement of the switches and modulator and examine the transmitter components in detail. Section 4.5 will briefly describe characteristics of the optical fiber, and section 4.6 will investigate the components of the OTDM receiver.

4.3 Optical Source Characteristics

The continuous wave optical source in the system is simply composed of a laser and an optical isolator as shown in Figure 4.2. The laser source used for all the experimental work was the Fujitsu distributed feedback laser model #FLD150F3CJ. The maximum optical output power from the laser was +6 dBm, and the operating wavelength

was 1551.0 nm. This particular laser was chosen because its output power was high, and its DFB structure yields a narrow spectral linewidth.

Figure 4.2 : CW Light Source Components

An optical isolator was placed immediately after the laser to minimize reflections to the source. It is important to limit reflections since the spectral width of the laser is broadened by reflections. If reflections to the laser can be eliminated or at least substantially reduced, then a relatively narrow spectral width can be achieved. Since a main concern of the OTDM system was to obtain a narrow spectral width for the transmitted signal, the unmodulated laser linewidth should be much smaller than the approximately 10 GHz information bandwidth of the imposed 10 Gb/s data. The optical isolator used to reduce the feedback to the laser was an OFR model #IO_F_IR2 polarization independent isolator. This device provided at least 33 dB of isolation and had a return loss in excess of 60 dB. The insertion loss of the isolator was about 2.0 dB and so the maximum power available at the isolator output was about +4.0 dBm.

4.3.1 Laser Relative Intensity Noise Measurement

All lasers are inherently noisy due to the quantum nature of light. Spontaneous emission is the primary source of both phase and intensity noise in lasers [40]. Phase noise, or frequency fluctuation in the spontaneous emission is the root cause for the finite spectral width of lasers. Intensity fluctuations of the spontaneous emission determine the laser intensity noise.

The relative intensity noise (RIN) parameter of a laser describes the ratio of the laser intensity noise to the average output power of the laser. The RIN of a laser is in general a

function of several parameters, including the physical structure of the laser and operational factors such as the bias level and output power of the laser. RIN is also a function of frequency with a RIN peak occurring at the relaxation resonance frequency of the laser.

Laser RIN is an important noise consideration in any lightwave system. For digital systems in particular, such as the OTDM system, noise limits the bit error rate performance of the system. For a digital system a signal to Gaussian noise ratio of about 15.5 dB will yield a standard acceptable bit error rate of 10^{-9} [41]. Therefore, in order to avoid RIN limitations, a laser with a RIN level of somewhat less than -15.5 dB should be used to make 10^{-9} error rate performance possible.

The RIN of the Fujitsu laser was measured using a Hewlett Packard model 71400 Lightwave Signal Analyzer and associated RIN software. Figure 4.3 displays the laser RIN as a function of frequency from 0 to 22 GHz. The worst case value of the RIN occurs at approximately 11 GHz and was measured to be -134.5 dB/Hz after subtracting out the thermal and shot noise contributions.

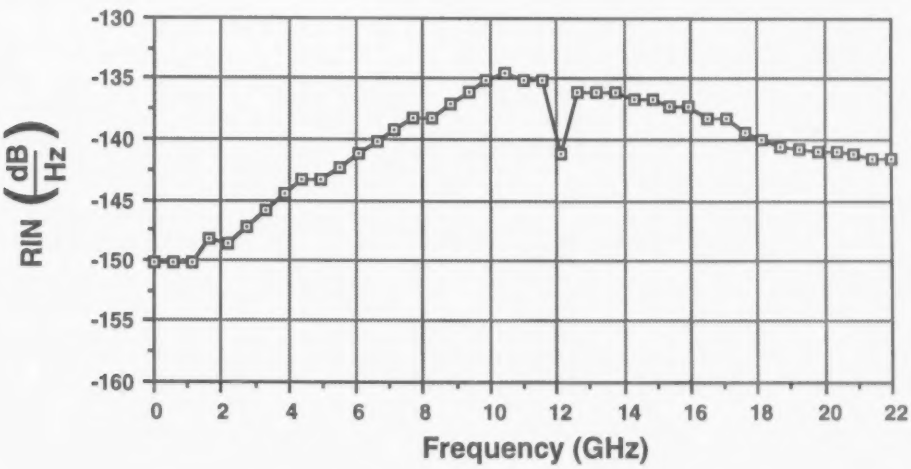

Figure 4.3 : Laser Relative Intensity Noise

The electrical bandwidth of the OTDM signals at the receiver will be approximately 2.5 GHz per channel. Using the worst case value for the RIN of -134.5 dB/Hz, the total RIN in a 2.5 GHz bandwidth is :

$$\begin{aligned} RIN_{2.5GHz} &= -134.5 \text{ dB/Hz} + 10*\log10(2.5*10^9 \text{ Hz}) \\ &= -40.5 \text{ dB} \end{aligned}$$

Thus the maximum RIN related signal to noise ratio after detection will be 40.5 dB. A more accurate value for the total RIN is obtained by integrating the RIN from 0 to 2.5 GHz. Performing the integration under the curve in Figure 4.3, a RIN level of approximately -55 dB is obtained. Since the signal to noise ratio as a result of laser RIN is 25 to 40 dB greater than that required for a 10^{-9} bit error rate, we can safely conclude that the RIN from the Fujitsu laser used the OTDM system will not be the limiting noise factor in the system. A more thorough examination of the various noise sources and their relative significance in the OTDM system will be presented later in section 4.6.2.6.

4.3.2 Laser Linewidth Measurement

To avoid excessive dispersion penalties, one of the objectives of this work was to ensure that the optical linewidth of the transmitted OTDM signal was primarily determined by the information imposed on the optical carrier. To meet this objective, the unmodulated laser light must have a linewidth that is significantly narrower than the information bandwidth since the overall spectral width is determined by the convolution of the laser lineshape with the data spectrum. For 10 Gb/s transmission requiring approximately 10 GHz of bandwidth, we would like the unmodulated laser to have a spectral width of no more than perhaps 1 GHz.

The spectral width of the Fujitsu laser source was experimentally determined by using the standard self-delayed homodyne (DSH) measurement technique [42]. Figure 4.4 below shows the experimental setup used to perform the measurement :

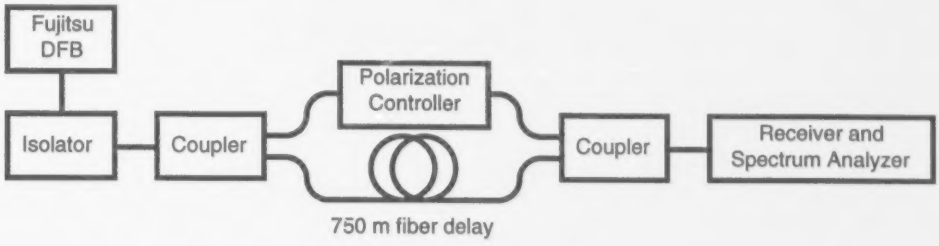

Figure 4.4 : DSH Experimental Setup

A qualitative explanation of how the technique works will be presented here. The mathematical details can be found in the cited reference.

The isolated laser light is first split into two branches using a standard coupler. The light in one branch is delayed by a section of fiber, and the light in the other passes through a polarization controller. The light in the two branches is then recombined in the second coupler and detected by the receiver. If the length of the delay fiber is much longer than the coherence length of the optical source, then the recombined optical signals are incoherent. When the two signals are mixed in the photodetection process, one signal may be thought of as an independent local oscillator which mixes the other incoming signal down to baseband. The frequency resolution obtained using this system is given by [42]:

$$\Delta f = \frac{c}{2\,n\,L} \qquad (4.1)$$

where $c = 3*10^8$ m/s is the speed of light in a vacuum, $n = 1.4$ is the refractive index of the fiber, and L is the length of the fiber delay line. For a 750 m fiber delay as shown in Figure 4.4, the measurement resolution is roughly 140 kHz. The laser under test

is expected to have a linewidth on the order of MHz, and so this 140 kHz resolution should be sufficient.

It can be shown that if the lineshape of the laser spectrum is Lorentzian, then the lineshape produced at baseband is also Lorentzian with double the original laser linewidth [43]. The mixing process in effect convolves the Lorentzian laser spectrum with itself. This process reproduces the same Lorentzian lineshape at baseband with twice the spectral width as shown in Figure 4.5 below:

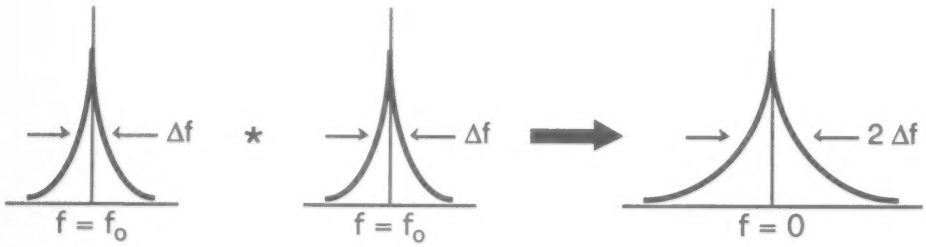

Figure 4.5 : DSH Baseband Beat Spectrum

The polarization controller is included in one branch of the interferometer to allow the polarizations of the two signals to be aligned so that the baseband noise is maximized. The single-sided lineshape produced at baseband can be observed on a conventional spectrum analyzer.

The DSH experiment was carried out using the 1551 nm Fujitsu DFB as the optical source operated at a +4 dBm optical output power level. Figure 4.6 displays the beat spectrum which was observed at baseband using a spectrum analyzer. The data points in the Figure have been adjusted to factor out the contributions of thermal noise and shot noise.

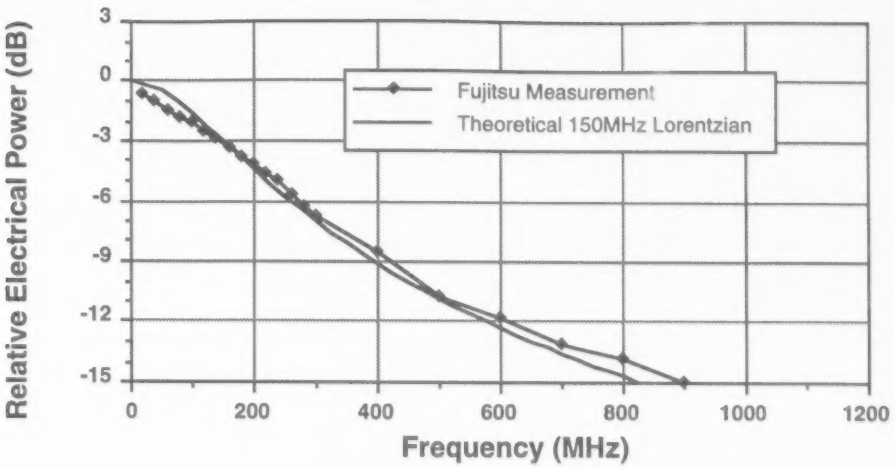

Figure 4.6 : Fujitsu DSH Baseband Beat Spectrum

From Figure 4.6, we can see that the 3 dB electrical half width of the beat spectrum is approximately 150 MHz. Since this baseband spectrum is twice the width of the original laser linewidth, the full-width 3 dB electrical linewidth of the Fujitsu laser is 150 MHz. Figure 4.6 also shows that the experimentally determined DSH baseband lineshape agrees well with the Lorentzian lineshape which would theoretically result from the DSH process using a 150 MHz wide Lorentzian source.

The 150 MHz linewidth of the source is almost two orders of magnitude less than the 10 GHz information which will be impressed on the carrier. The spectral width of the signal at the output of the OTDM transmitter is given by the convolution of the laser lineshape with the spectral envelope of the data. Therefore, the inherent optical linewidth of the Fujitsu laser source chosen for the OTDM experiments will not significantly broaden the spectrum of the transmitter output signal. There is, however, residual switch or modulator chirp to consider which may also contribute to spectral broadening. This phenomenon will be investigated later in section 4.4.2.

4.4 OTDM Transmitter

Having completed our investigation of the optical source characteristics, we now turn our attention to the OTDM transmitter block of Figure 4.1. This section examines a specific configuration of the OTDM transmitter in order to provide a setting for the analysis of its typical components.

Figure 4.7 shows the experimental setup used to accomplish optical time division multiplexing on two 2.5 Gb/s channels.

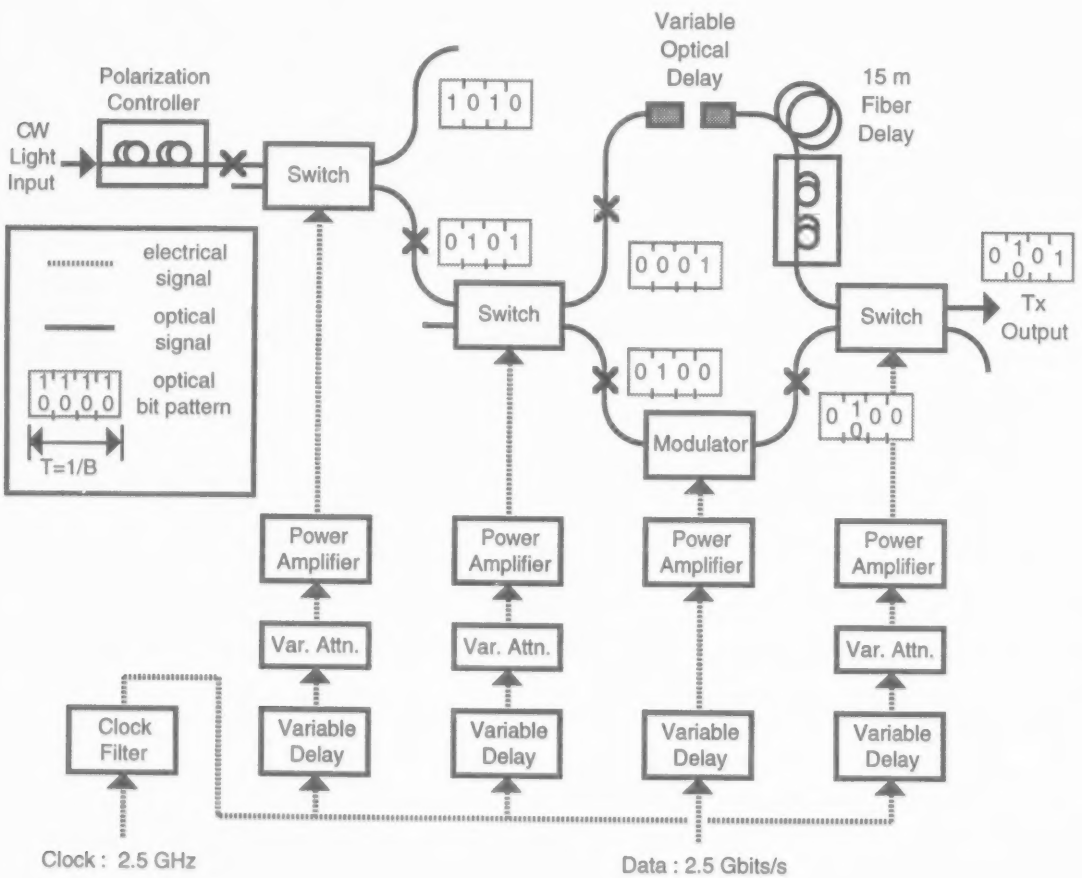

Figure 4.7 : OTDM Transmitter

This configuration is a subset of the the full-blown four channel OTDM architecture examined previously in Chapters 2 and 3. As shown in the optical timing frames in the diagram, the data channel is interleaved with the continuously pulsed channel which is offset by two bit positions. This configuration demonstrates the OTDM principle from 2.5 Gb/s up to 5 Gb/s using pulses ultimately intended for 10 Gb/s transmission. The various OTDM system configurations and their performance is dealt with later in Chapter 5.

4.4.1 Polarization Controller

A polarization controller was placed prior to the first switch to adjust the polarization of the light entering the switch. Appendix 4A describes in more detail the theory and physical implementation of the polarization controller. The controller was used to adjust the polarization of the light to a linear state and to orient it in the direction which maximized the electro-optic effect of the switch. The insertion loss of the device was approximately 1 dB.

4.4.2 Modulator and Switch Characteristics

Key elements in the OTDM concept are the electro-optic switches and modulators. This section will concentrate on examining the performance characteristics of these devices. A brief description of the switches and modulator used in the OTDM configuration will be presented, along with a discussion of the rationale for their selection. Specific dc and radio frequency (rf) measurements of the devices will then be presented. Finally, experimental determination of the residual chirp associated with the switches will be investigated.

4.4.2.1 Switch and Modulator Selection

As discussed earlier in Chapter 2, the switching and modulating functions in the OTDM system may be performed by a single type of 2 x 2 switch. However, the two

functions are distinctly different, and under closer examination of the requirements for each function, it becomes apparent that using different devices for the two functions is advantageous. The switches should have a low drive voltage at the particular frequency of operation. The low voltage requirement is especially important in this particular experimental setup since the first switch will be driven at twice the switching voltage. Recall from section 3.5 of Chapter 3 that driving the switch with a 2.5 GHz sinusoidal electrical signal with an amplitude of 2 V_π can be used to generate 5 Gb/s pulse streams. Since the switches are driven at single frequencies, the actual frequency and phase response of the switches is not so important. For the modulator, on the other hand, relatively flat wideband phase-linear performance is required since the modulator is driven by a 2.5 Gb/s digital signal.

In view of the distinct requirements for the switching and modulating functions, different electro-optic devices were selected for the two purposes. The ETEK 2 x 2 switch model #EOSW-0202-1550 was selected for the switching function. Four switches were obtained to facilitate the OTDM work. The switches were of the balanced-bridge class examined in Chapter 2. A simple layout of the device is shown in Figure 4.8. The input and output fibers consisted of Corning 1550 nm polarization maintaining single mode fiber with a mode field diameter of 6 to 7 μm. All fibers were connectorized with FC/PC type optical connectors which were keyed identically to facilitate cascading switches without a need for intermediate polarization controllers.

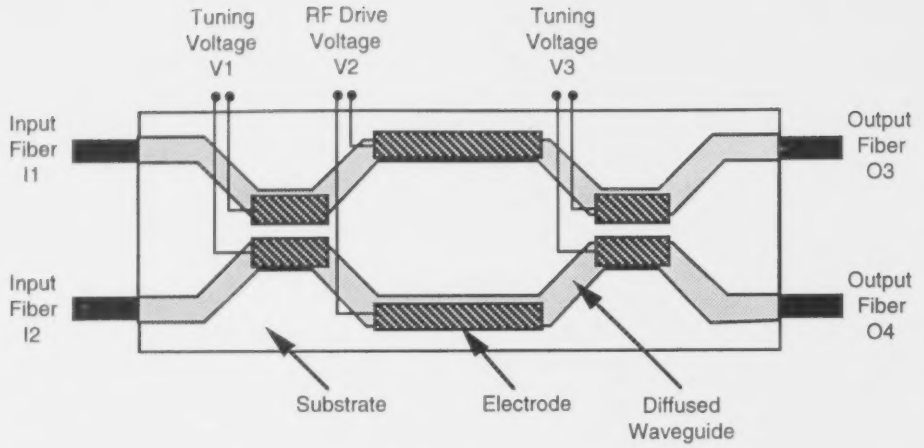

Figure 4.8 : ETEK 2 x 2 Switch Configuration

The switches typically required a dc switching voltage of about 5 volts, and had a specified 3 dB electrical bandwidth of 4-5 GHz.

The United Technologies Photonics modulator #APE-YBBM-1.5-12.T-02 was selected to perform the modulating function. This particular modulator was a 1 x 2 balanced bridge type device, where the single input was split into a standard interferometric section and followed by a 50/50 coupling stage at the output to provide complimentary outputs. The layout of the modulator is shown in Figure 4.9. The input and output fibers consisted of Fujikura 1550 nm polarization maintaining single mode fiber with a mode field diameter of about 10 μm. Again, the fibers were connectorized with FC/PC type optical connectors and keyed in the same manner as the ETEK 2 x 2 switches.

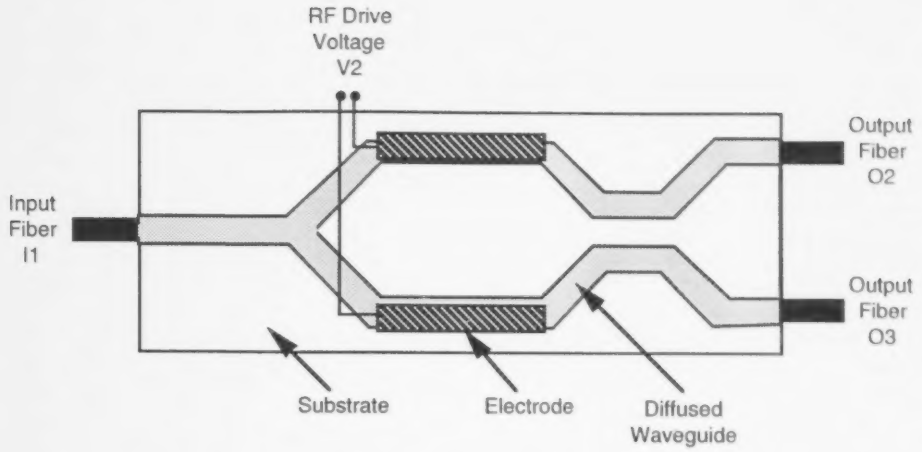

Figure 4.9 : UTP 1 x 2 Modulator Configuration

The modulator switching voltage was approximately 6 volts and the specified 3 dB electrical bandwidth was 12 GHz. The wide bandwidth of this device makes it useful for any experiments involving multi-gigahertz external modulation.

4.4.2.2 DC Characteristics

The dc operating characteristics of the switches and modulators were confirmed experimentally. All of the measured parameters fell within the stated specifications. The table below summarizes the dc performance of the electro-optic devices. More complete details on the performance of the switches and modulator are provided in appendix 4B.

Parameter	Typical ETEK	UTP
Insertion Loss*	6-8 dB	5 dB
Extinction Ratio*	22-40 dB	24-32 dB
DC Vπ	4.3-5.3 volts	5.8 volts
I/O Coupler Tuning Bias	0-15 volts	not applicable

* Parameter varies depending on input or output selected.

Table 4.1 : ETEK and UTP DC Performance Data

These results were obtained by using the isolated laser source, an optical power meter, and variable dc voltage sources to test each device. Note that the optical patchcords

used in these tests were standard single mode SMF28 fiber with a mode field diameter of about 10 μm. Since the mode field diameter of the Corning fiber pigtails on the ETEK switch is 6-7 μm, there is an excess coupling loss due to mode mismatch when the Corning fiber is connected to the SMF28 fiber. The theoretical mode mismatch splice loss $L_{(r)}$ is given by [44]:

$$L_{(r)} = -10 \log_{10} \left[\frac{4 r^2}{(1 + r^2)^2} \right] \qquad (4.2)$$

where r is the ratio of the mode field diameters for the two fibers. For the connection of standard fiber and ETEK fibers, using a factor of r=10/6.5=1.53 yields a theoretical loss of about 0.8 dB per connection. The insertion loss reported for the ETEK switches in the appendix and in the preceding table includes mismatched connections at both the input and output fibers, and thus 1.6 dB of that loss is attributable to mode mismatch alone. Note however, that there will be no mismatch when the ETEK switches are cascaded since the fibers will be of the same type. In addition, there is essentially no mode mismatch loss when using the UTP modulator in conjunction with SMF28 fiber since the Fujikura and SMF28 fibers have comparable 10μm mode field diameters.

4.4.2.3 RF Characteristics

Two techniques were used to determine the frequency responses of the switches and modulators. The first method involved measuring the small-signal swept-frequency response of the electro-optic device cascaded with a photodetector as shown in Figure 4.10 below:

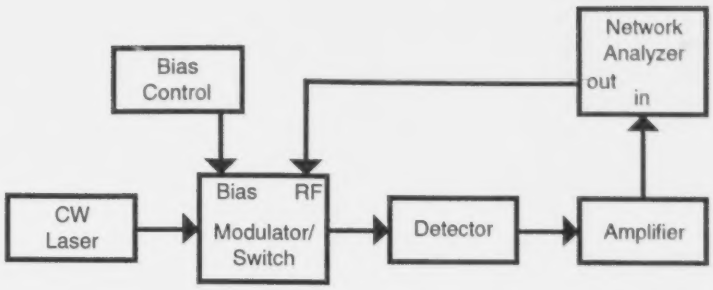

Figure 4.10 : Experimental Setup for Swept Frequency Modulator and Switch Frequency Response Measurements

The response of the switch or modulator and the detector is isolated from the rest of the electrical setup in the network analyzer calibration step. Then, the frequency response of the electro-optic device cascaded with the photodetector is measured. If the frequency response of the photodetector is known, then the response of the switch or modulator can be obtained by subtracting the detector response from the cascaded response. Isolating the frequency response of the photodetector will be discussed later in section 4.6.2.3. Figure 4.11 shows the frequency responses of the typical ETEK switch and the UTP modulator as measured using the swept frequency technique.

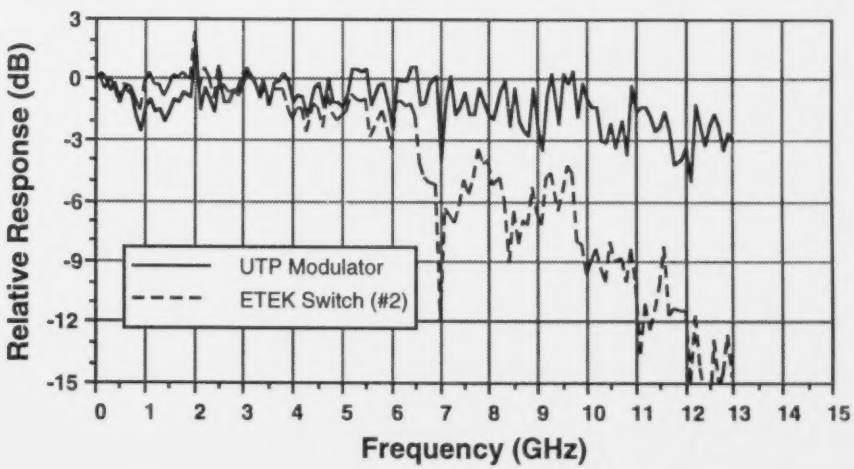

Figure 4.11 : Modulator and Switch Frequency Responses Based on Network Analyzer S_{21} Measurement

A second technique was used to confirm the swept-frequency measurements of the switch and modulator RF performance. This method involved driving the electro-optic devices with single tones as shown in Figure 4.12 below :

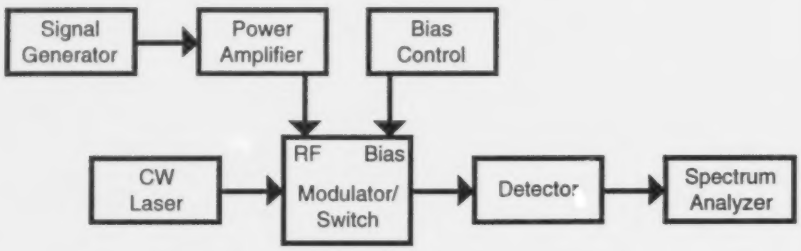

Figure 4.12 : Single Tone Modulator and Switch Frequency Response Experimental Setup

In section 4.6.2.3 dealing with photodetector frequency response measurements, it will be shown that the frequency responses of both the detector and switch can be determined independently. When the switch is biased at the midpoint and driven with a single frequency, the maximum power in the fundamental is achieved at the receiver when the drive voltage amplitude to the switch is 1.17 V_π. To determine the switching voltage or power of the switch at a particular frequency, the drive voltage is increased until the power observed in the fundamental is maximum. At this point, the drive voltage is equal to 1.17 V_π. The frequency response of the switch can be determined by carrying out the procedure at selected frequencies and noting the frequency dependence of V_π. Figures 4.13a and 4.13b show the frequency responses for the typical ETEK switch and UTP modulator using the single-tone technique. For comparison purposes, the results from the swept-frequency measurements are superimposed in both Figures.

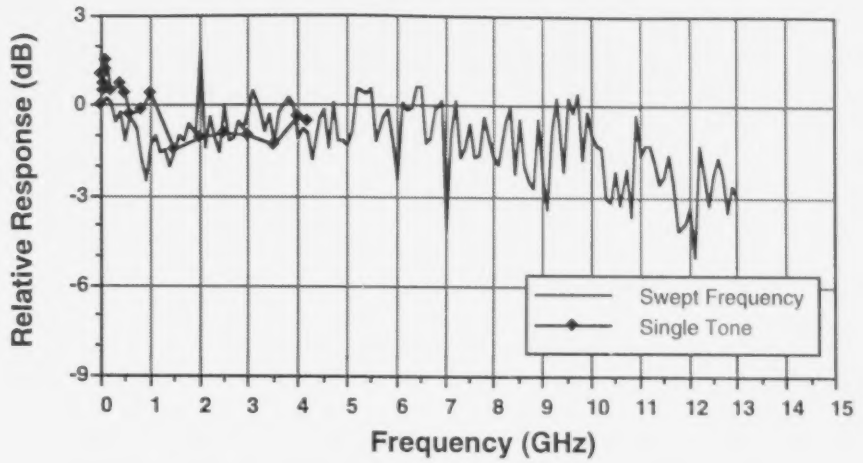

Figure 4.13a : Single Tone and Swept Frequency Modulator Response

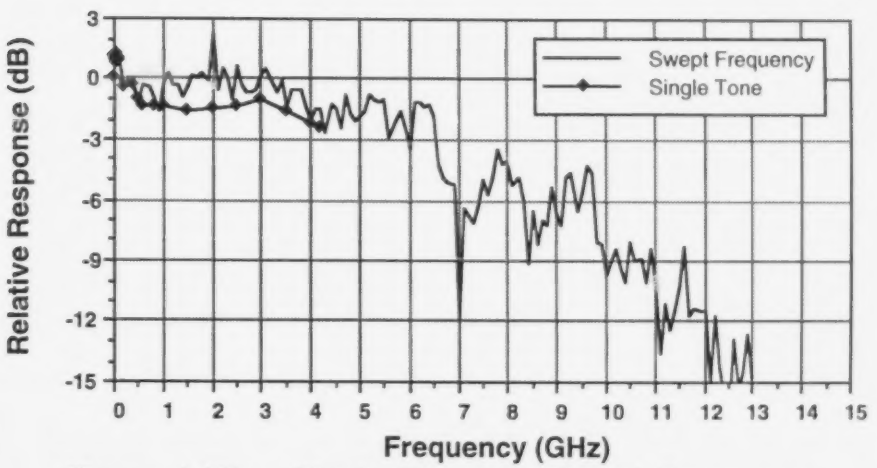

Figure 4.13b : Single Tone and Swept Frequency Switch Response

As Figure 4.13a shows, the 3dB electrical bandwidth of the UTP modulator was approximately 12 GHz, which conforms with the specification. With this relatively wide bandwidth, the UTP modulator can be safely driven with the 2.5 Gb/s digital data signal. The low frequency (ie: < 50 MHz) full switching rf power required for the UTP modulator was approximately +27 dBm. This level is within the +29 dBm 1 dB compression limit of the power amplifier which drives the modulator.

The 3dB electrical bandwidth for the typical ETEK switch was approximately 6 GHz, which also meets the device specifications. The typical low frequency full switching power required for the ETEK switch was about +22 dBm, and thus the switches can be driven with the available amplifier. $2V\pi$ switching requires 6 dB more power and thus +28 dBm is required for low frequencies. At 2.5 GHz, approximately +29.5 dBm is required for $2V\pi$ switching which means that the power amplifier gain will be compressed by greater than 1 dB. Operating the amplifier in the gain compressed region should not pose a problem since the amplifier introduces no distortion at single frequencies.

4.4.2.4 Switch Chirp

In section 4.3.1.2 it was determined that the inherent spectral width of the optical source was about 150 MHz. It was also concluded that this inherent linewidth would not significantly broaden the approximately 10 GHz spectrum of the data carrying signal at the OTDM transmitter output. There is one more factor which may contribute to spectral broadening of the transmitted signal. As discussed theoretically in section 2.2.1.3, the electro-optic switches and modulators may introduce residual phase modulation or chirp which will also broaden the optical spectrum.

As far as chirp is concerned, the electro-optic device which has the greatest potential impact on the OTDM system is the first switch in the transmitter. Chirp is essentially wavelength shifting on the edges of pulses. The first transmitter ETEK switch creates the narrow 10 Gb/s pulses. The second switch stage and the modulator serve only to 'gate' the pulse, and do not introduce new pulse edges. Since the first switch creates the pulse edges, chirping will be greatest at that point.

Both the ETEK switches and the UTP modulator are of the balanced bridge design. Since the design incorporates a symmetric electrode structure, these devices should in

theory produce no residual chirp. In reality, however, there will be some asymmetries due to the fabrication processes and therefore the devices will not operate perfectly chirp-free. This section will qualitatively assess the severity of the residual chirp in the electro-optic devices and estimate the impact of this chirp on the performance of the OTDM system.

Figure 4.14 shows the experimental setup used to investigate chirp in the modulator and switch.

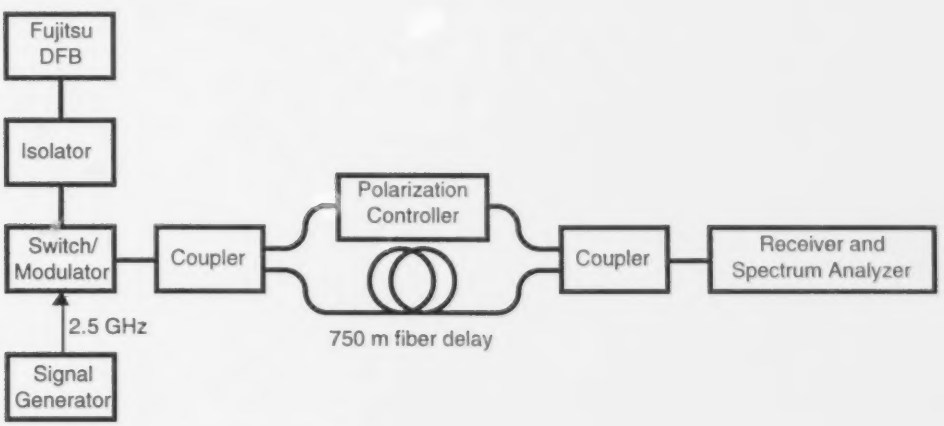

Figure 4.14 : Switch and Modulator Chirp Experiment

The experiment involves external single frequency modulation of the optical source in conjunction with a delayed self-homodyne mixing stage. If the electro-optic switch or modulator is driven with an electrical tone of frequency f_m, then the optical spectrum at its output will contain dc and f_m components as shown in Figure 4.15 below :

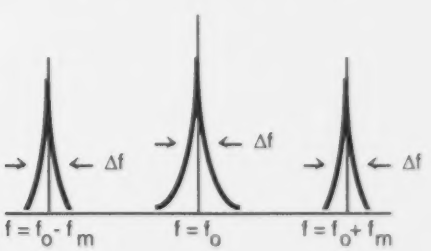

Figure 4.15 : Single Frequency Modulated Optical Spectrum

If the external modulator is chirp-free, then the linewidth of each of the spectral components is the inherent laser linewidth Δf as shown in the Figure. After the delayed self-homodyne mixing stage, the spectrum analyzer will display at baseband the convolution of this optical spectrum with itself. In the case of chirp-free operation, the linewidth of each of the spectral components will be 2Δf as shown in Figure 4.16.

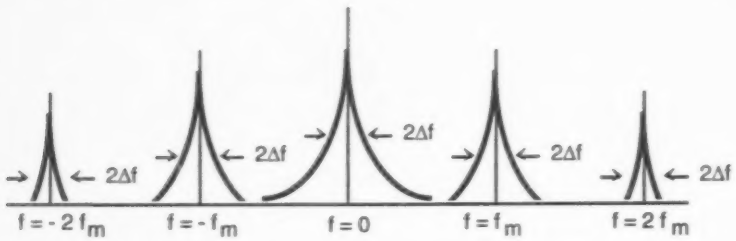

Figure 4.16 : DSH Baseband Spectrum

If the electro-optic device introduces significant chirp into the signal, the optical spectral components will be much wider than Δf, and the DSH-produced electrical baseband spectral components will be much wider than 2Δf. In addition, the lineshapes of the spectral components at both optical frequencies and at baseband will not be Lorentzian since chirping will modify the lineshape as well as the linewidth.

The DSH chirp experiment was carried out using the ETEK switch driven with a full-V_π 2.5 GHz electrical signal. Note that full-V_π drive of the switch produces higher order harmonics in the modulated optical output due to the nonlinear switching characteristic of the Mach-Zehnder type switch. The electrical power in the third harmonic was calculated to be 18dB less than the power in the fundamental. The additional spectral components introduced in the DSH process as a result of the presence of even the third harmonic are not significant, and for qualitative purposes the higher order harmonics may be ignored.

Figures 4.17a and 4.17b display the single-sided baseband spectrum observed on the spectrum analyzer using the ETEK switch and the UTP modulator in the DSH chirp experiment.

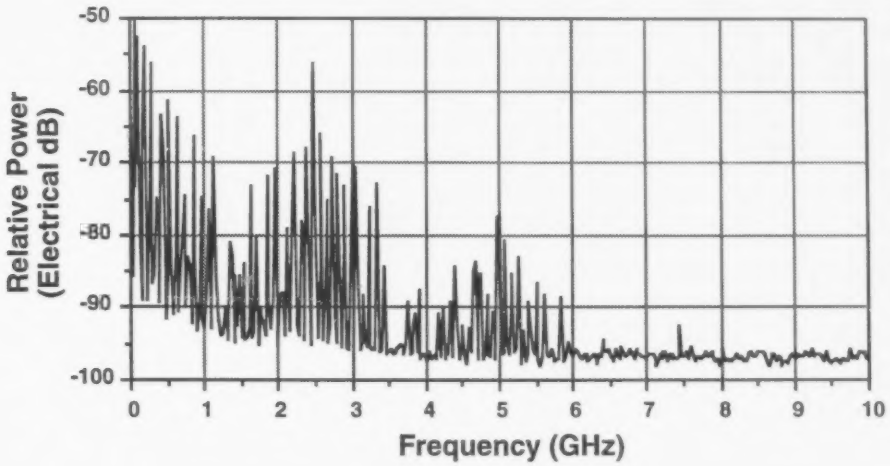

Figure 4.17a : UTP Chirp Baseband Spectrum

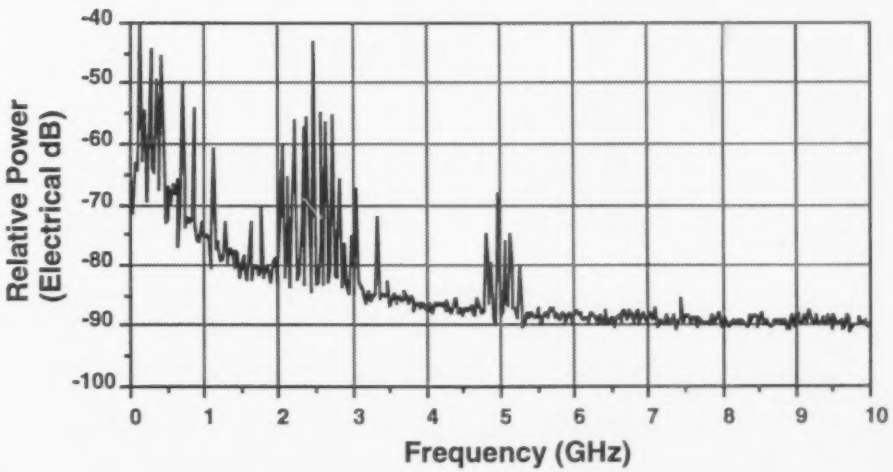

Figure 4.17b : ETEK Chirp Baseband Spectrum

The dc, 2.5 GHz, and 5 GHz spectral components are readily distinguished in both Figures. In addition, the full-width half-maximum linewidth at any of the peaks appears to

be no wider than perhaps 200 MHz. This figure is close to the 150 MHz spectral width of the laser itself. Therefore, the additional spectral broadening due to residual switch and modulator chirp is qualitatively insignificant.

It has now been determined that the combined line-broadening effects of both the laser itself and residual chirp are substantially less than the 10 GHz information bandwidth to be imposed on the carrier. It can now be stated with confidence that the spectral width of the optical signal at the OTDM transmitter output will be primarily information limited.

An interesting feature of Figures 4.17a and 4.17b is the somewhat discrete nature of the spectral scans. This characteristic probably warrants further exploration. For now, it is hypothesized that the discrete components of the Figures arise from the fixed relative phase introduced between the two modulated signals in the self-homodyne experimental set up. It is thought that to obtain a more continuous plot, the phases of the modulated signals could be adjusted through a full 360 degrees during the spectral measurement using some sort of variable optical delay component. Alternatively, one could modulate the optical signal in one branch only. This would remove the fixed phase condition altogether since only one of the recombined signals would be modulated.

4.4.3 Multiplexing Optical Signals

Having examined the operation of the electro-optic switches and modulators of the OTDM transmitter, we will now explore important issues involving multiplexing the optical signals. Specifically, this section discusses the timing of optical signals, and also deals with a coherence problem which arises during the OTDM multiplexing process.

4.4.3.1 Variable Optical Delay

Inspecting the optical bit pattern diagrams of Figure 4.7, we see that some form of optical path length adjustment is required in order to time properly the interleaving of the

0001 pulsed channel with the $0\ \frac{1}{0}\ 00$ data channel. There is no way to accomplish this timing through electrical delay adjustments. The relative timing of the the two channels must be accurate since the $0\ \frac{1}{0}\ 01$ channel is ultimately intended to be multiplexed with the 1010 channel. Therefore, if we allow +/- 10% timing error for a 10 Gb/s pulse, the required adjustment resolution using an optical index of 1.44 is :

$$\Delta P_{res} = +/- (10\%) (10*10^9\ s^{-1})^{-1} * (3*10^{10}\ cm/s) * (1.44)^{-1}$$
$$= +/- 2.1\ mm$$

The maximum adjustment required is two full bit periods or

$$\Delta P_{max} = 2 (10*10^9\ s^{-1})^{-1} * (3*10^{10}\ cm/s) * (1.44)^{-1}$$
$$= 4.2\ cm$$

While it is possible to cut fiber lengths to these tolerances, it is not a simple or flexible solution. Fibers of different lengths are required every time the system is re-arranged. As shown in Figure 4.7, the OTDM variable optical delays were accomplished using two SELFOC lenses in a free space configuration. The positioning and separation distance between the lenses was controlled through the use of optical positioning hardware. Using an optical index of 1 in the previous calculations we obtain the free space resolution and maximum spacings as 3.0 mm and 6.0 cm respectively. These targets were readily achieved using the SELFOC lenses. The insertion loss through the two lens arrangement was typically less than 2 dB for lens separations of up to 10 cm.

4.4.3.2 Coherence Problems

During the collection of the experimental results for the OTDM system, it was discovered that the multiplexed $0\ \frac{1}{0}\ 01$ signal was unstable. When viewed on the sampling oscilloscope, the waveform at some instants of time was quite clear. However, over a period of seconds the waveform would fluctuate so badly that the data and pulse streams

were not recognizable. It was determined that the source of these fluctuations was a coherency problem involving partial pulse overlap of the two multiplexed channels.

When operated using purely sinusoidal signals for creating optical pulses, the OTDM system does not yield non-overlapping pulses as suggested by the notation $0\ \frac{1}{0}\ 01$ typically used in the OTDM Figures. As observed in the computer simulations of Chapter 3, the pulses created by the $2V_\pi$ OTDM system are partially overlapping due both to the finite extinction ratio of the switches and the sinusoidal drive signal applied to the switches. Figure 4.18 below shows the theoretical optical electric field envelopes of two ones on channels two bits apart when combined with the optical switch. The Figure clearly shows that there is some pulse overlap even in the ideal OTDM case where the extinction ratio is infinite.

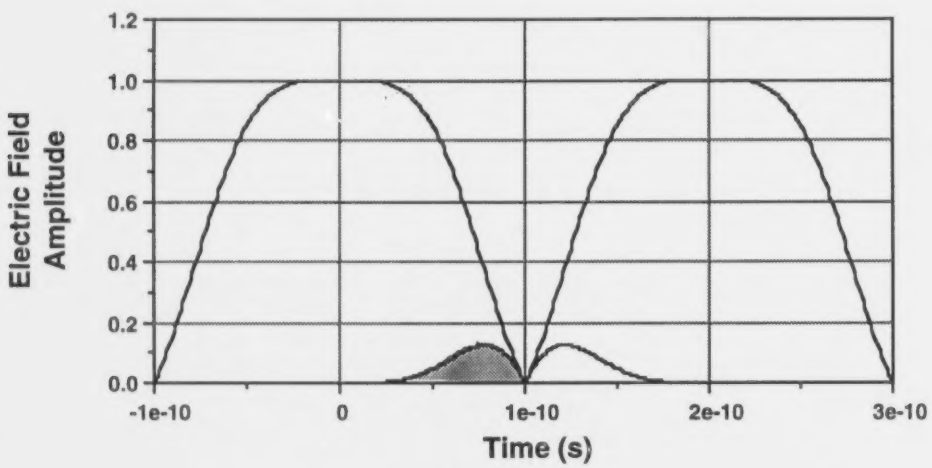

Figure 4.18 : Pulse Overlap (2 Bit Separation)

The overlapping occurs to a much greater extent when immediately adjacent pulses are multiplexed. Figure 4.19 shows the theoretical pulse overlap when adjacent pulses are combined through the optical switch. The pulse shapes are not the same as those in Figure 4.18 since $2V_\pi$ switching is used to multiplex immediately adjacent pulses.

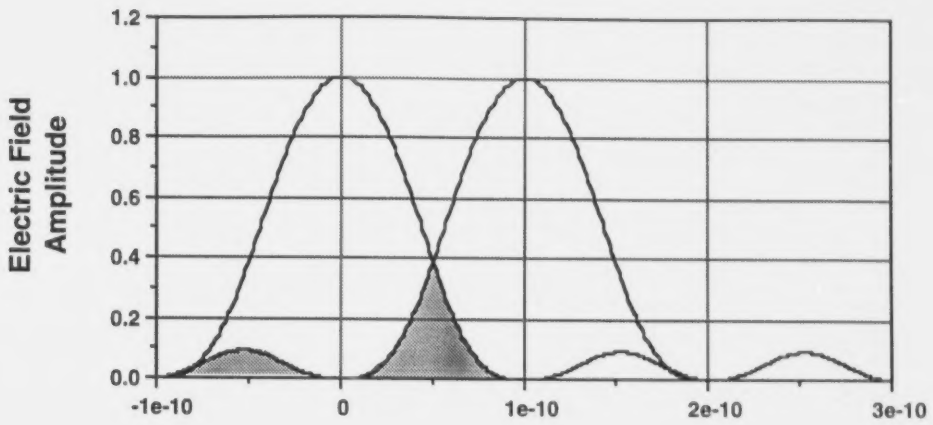

Figure 4.19 : Pulse Overlap (1 Bit Separation)

If the OTDM system is implemented as an integrated optical circuit as described in Chapter 2, the optical signal path lengths will be less than perhaps 5 cm from the point at which the pulses are divided until the pulses are recombined. The difference in the distance travelled by any two optical signals which are recombined may be limited to less than millimeters depending on the accuracy of the fabrication process. Now the coherence length L of the optical source is related to its spectral width Δf by [4]:

$$L = \frac{c}{2\, n\, \Delta f} \qquad (4.3)$$

$$= \frac{3*10^8 \text{ m/s}}{2\ (1.44)\ (150 \text{ MHz})} = 70 \text{ cm}$$

In an integrated OTDM system, the path length difference of recombined optical signals would be much less than the coherence length of the optical source, and therefore the signals are phase related. As indicated earlier in Chapter 2, the phases of the optical signals must be aligned so that constructive interference or electric field addition occurs. This phase alignment could be accomplished by using a phase modulator in one branch of any pair of recombined optical signals.

In the distributed component approach, however, individual switches and modulators are linked together using relatively long lengths of fiber. The optical path lengths in this case are on the order of meters. In the experimental setup used for our experiments, the path length difference between recombined optical signals was not easily controlled. In addition, phase modulators were not available to perform phase alignment. If the phases of the overlapping recombined optical pulses are not aligned, then the sum of electric fields can vary from complete addition to complete subtraction.

Even if phase modulators were available, thermal variations over meters of fiber will likely cause significant phase fluctuations. The differential optical path delay as a function of temperature for typical silica fiber is approximately 40 ps per km per ^{o}C. For typical fiber path lengths of about 5 meters for the OTDM recombined optical signals, only a 0.05 ^{o}C temperature variation between the two fiber paths will result in 180^{o} of phase shift between the two optical signals at at 1550 nm operating wavelength. Unless both the optical phase and temperature stability of the system can be accurately controlled, coherent addition of the optical signals in the distributed system will not be possible.

In the experimental setup where the multiplexed waveform fluctuations occurred, the path lengths of the recombined optical signals were about 5 meters, and the path difference between the recombined signals was about one meter. Since this path length difference was on the order of the coherence length, it is suspected that the waveform fluctuations described earlier were in fact due to quasi-coherent addition of the two signals. Sometimes the frequencies of the two multiplexed signals were the same. In this case, thermal variations likely caused instability in the combined signal due to electric field addition under fluctuating phase conditions. When the frequencies of the two signals were sufficiently different, there was little fluctuation since the optical signals would add on an

intensity basis. In other words, it is hypothesized that both frequency and phase variations of the two almost coherent optical signals caused instability in the combined signal.

Since coherent addition of the signals was not practical in the distributed OTDM implementation, another solution was conceived. As shown in Figure 4.7, one optical signal was intentionally delayed using 15m of fiber to ensure that the multiplexed signals were incoherent. In this configuration, the two optical signals are added on an intensity basis, and any thermally induced phase fluctuations will not produce instability.

Note, however, that incoherent addition of the two signals also introduces some problems of its own. When it is stated that the two signals are incoherent, we mean that the frequencies of the two signals are not correlated. It is false to assume that the frequencies of the two signals will never be the same. Increased noise will be produced whenever the frequencies of the two signals become close. In effect, a self-delayed homodyne system has been set up, and a beat-noise spectrum is produced at baseband in the same manner as described earlier in the analysis of the optical source spectral width.

Quantitative determination of the additional noise introduced into the digital OTDM system as a result of this 'incoherent' multiplexing process is not trivial. Several factors must be considered in the process. First, the baseband beat noise spectrum produced from mixing the two digitally encoded optical signals is not the same as that produced using cw laser light as examined in section 4.3.2. Second, the noise produced in a given digital pulse is not constant over the pulse duration. As Figures 4.18 and 4.19 show, the pulse overlap varies with time within a bit period. The noise at a particular time in the pulse depends on the amount of overlap from the adjacent pulse. Some method for determining the effective noise at the decision time in the pulse is required. In addition, the bandwidth of the system is limited at the receiver, and the noisy 'edges' of the pulses will be smeared in towards the decision point.

Mathematical analysis of the 'coherence noise' in the OTDM system will not be attempted in this work. Chapter 5 will present system results which experimentally determine the penalty associated with this phenomenon.

4.4.4 OTDM High Speed Electronics

Having finished examining the characteristics of the optical elements of the OTDM transmitter, we will now move on to discuss the electrical components of Figure 4.7. The electrical blocks of Figure 4.7 include the clock filter, the electrical delay elements, and the amplifiers. This section will review the implementation of these blocks in turn.

4.4.4.1 Clock Filter

The error rate test set provides the transmitter with a 2.5 GHz square wave clock output which is synchronized with the data signal. We wish to show that OTDM switching can be accomplished with purely sinusoidal signals. Therefore, a 2.5 GHz lowpass filter is used to recover the clock fundamental. This sinusoidal clock signal is then delivered to the switches after passing through separate variable electrical delays and power amplifiers.

4.4.4.2 Delay Adjustment

Delay adjustment is necessary to synchronize the drive signals with the optical signals entering the switches and modulator. Omni-Spectra coaxial phase shifters were used for the variable electrical delays. The delay adjustment range was about one centimeter, or about 50 ps of delay time if the rf propagation velocity in the device is 0.7c. This delay time corresponds to approximately 12 percent of the 400 ps (8 cm) data bit period. Therefore, lengths of semi-rigid coax were used to provide coarse delay adjustment, and the phase shifters were used to provide the variable fine adjustment.

4.4.4.3 Amplitude Adjustment

The error rate test set provided 2.0 volts peak to peak maximum amplitude clock and data signals. Since the switches and modulators required from 7 to 14 peak-peak volts for complete switching, power amplifiers were required to boost the signal amplitudes. For the switch signals, variable attenuators were inserted prior to the power amplifiers to provide amplitude adjustment capability. For the data signal, the amplitude was adjusted via the test set data output signal level.

The power amplifiers used in the experimental work were Mini-Circuits ZHL42W models. These amplifiers typically had passbands from 10 MHz to 4.2 GHz, and gains of 32-36 dB. The 1 dB gain compression output levels were +29 dBm which corresponded to about 17.8 sinusoidal peak-peak volts, or 12.6 square-wave peak-peak volts. This provides enough voltage to drive the switches at $2V_\pi$ and the modulator at V_π.

The switches are driven at single frequencies and therefore there is no distortion caused by ripples in the frequency response of the power amplifier. Amplifier distortion is a concern, however, for the relatively broadband 2.5 Gb/s data signal which drives the modulator. The 2.5 Gb/s, 2^7-1 pseudo-random data stream has a lower frequency component of 2.48832/(2^7-1) Hz or 19.6 MHz. The significant upper frequency content of the signal is limited to perhaps 2.5 GHz. The bottom trace of Figure 4.20 shows the eye diagram for the 2.5 Gb/s data signal as delivered by the test set. The top trace of Figure 4.20b shows the same data signal after amplification using the ZHL42W amplifier.

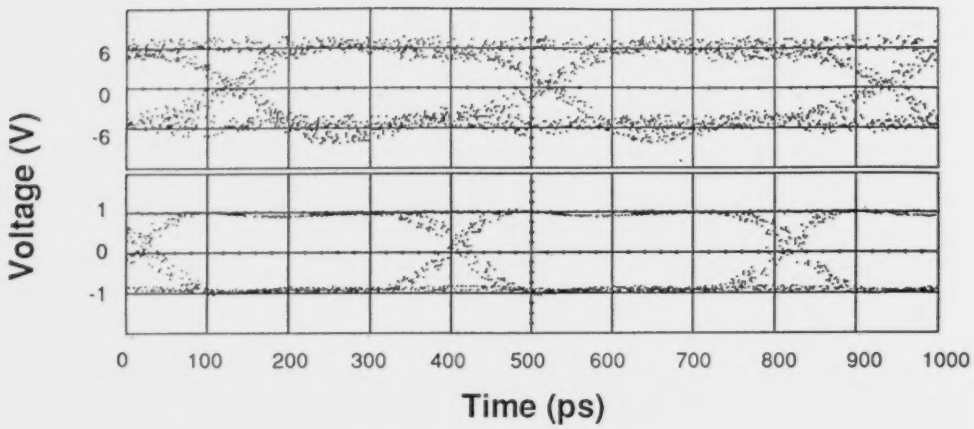

Figure 4.20 : Amplifier Distortion of 2.5 Gb/s Data Signal

There are several causes for the distortion in the amplified signal. First, there is some ripple in the 10-4200 MHz passband of the amplifier. Second, the phase response of the amplifier is not quite linear with frequency near the lower section of the passband (<50 MHz). And finally, the gain compression of the amplifier is in general a function of frequency, so additional ripple can be introduced into the passband at higher output levels.

Two characteristics of the modulator in the OTDM system serve to somewhat mitigate the distortion effects of the power amplifier on the data signal. First, the data signal is used only to gate the much narrower optical pulses which pass through the modulator. Therefore, the data signal can be electrically delayed such that the 'cleanest' part of the data eye is centered on the optical pulses. Second, and perhaps more important, is the fact that the cosine squared switching characteristic of the Mach-Zehnder modulator reduces the effects of overshoot and undershoot of a full V_π drive signal. Figure 4.21 shows the calculated optical intensity percentage amplitude ringing as a function of the electrical signal under-shoot or over-shoot ringing. For example, 10% amplitude ringing on the electrical drive signal pulses reduces to approximately 2.5% ringing on the optical

signal. The data eye diagram resulting from use of this power amplifier in the OTDM system will be presented in the system results section of Chapter 5.

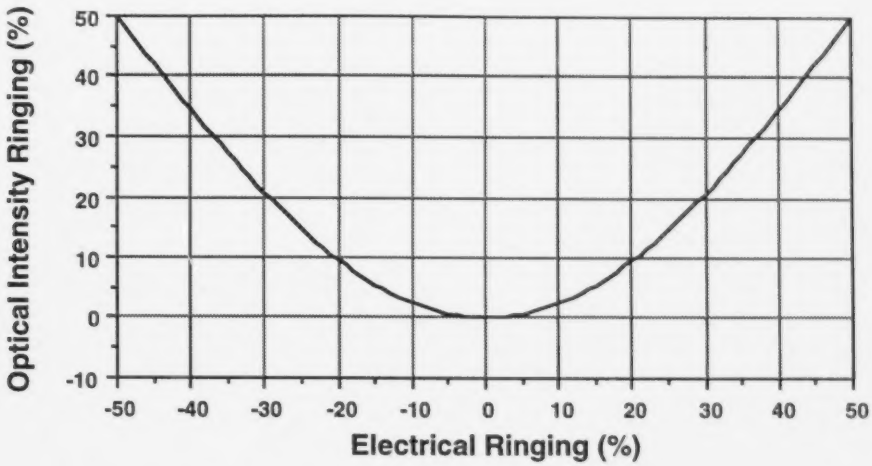

Figure 4.21 : MZ Modulator Ring Reduction

4.5 Fiber Characteristics

Having finished a description of the OTDM transmitter, we will now move on to describe briefly the optical fiber transmission medium. There were two types of fiber available for the OTDM transmission experimental work at TR Labs. One fiber type was 70 km of Corning 900-μm tight buffered fiber. This fiber was wound on 20 cm diameter spools, and was divided into two 25 km sections and two 10 km sections, with the ends of each section being terminated in angled physical contact (APC) connectors. The other fiber type was 100 km of Northern Telecom fiber, wound on 35 cm diameter spools, and divided into two 50 km sections. For both types of fiber, the attenuation constant was approximately 0.22 dB/km at an operating wavelength of 1550 nm. The estimated dispersion factors were 17 ps/(km nm) for both the Corning and the Northern Telecom fiber.

Depending on the OTDM configuration and transmission distance, up to 2 erbium-doped fiber amplifiers (EDFAs) were used to boost the optical signal. An EDFA was also used as part of the optical receiver, and EDFA operation will therefore be discussed as part of the receiver characteristics.

4.6 Receiver Characteristics

Now that the transmitter and fiber blocks of the OTDM system have been investigated, we will turn to examine the receiver component of Figure 4.1. The receiver will be discussed in two sections. The optical demultiplexing process will be described first, followed by details of the optical to electrical conversion process for a single 2.5 Gb/s optical data channel.

4.6.1 OTDM Receiver

Figure 4.22 shows an expansion of the receiver block from the overall system diagram of Figure 4.1. This particular receiver configuration optically demultiplexes two 2.5 Gb/s data channels which have been interleaved by the transmitter of Figure 4.7.

The operation of the OTDM receiver is relatively simple. The incoming optical signal is first passed through a polarization controller in order to maximize the electro-optic effect of the optical switch. The two 2.5 Gb/s channels are demultiplexed by the optical switch which is electrically driven with a 2.5 GHz sinusoidal clock signal.

Receiver clock recovery was not undertaken for the OTDM experimental work. The clock signal used in the OTDM experiments was a 'cheat' clock taken from the error rate test set at the transmitter. Using the transmitter clock for clocking in the receiver can introduce timing stability problems at the receiver if there is significant variation in the

frequency reference over the length of the transmission link. This issue will be discussed during analysis of the transmission experiments in Chapter 5.

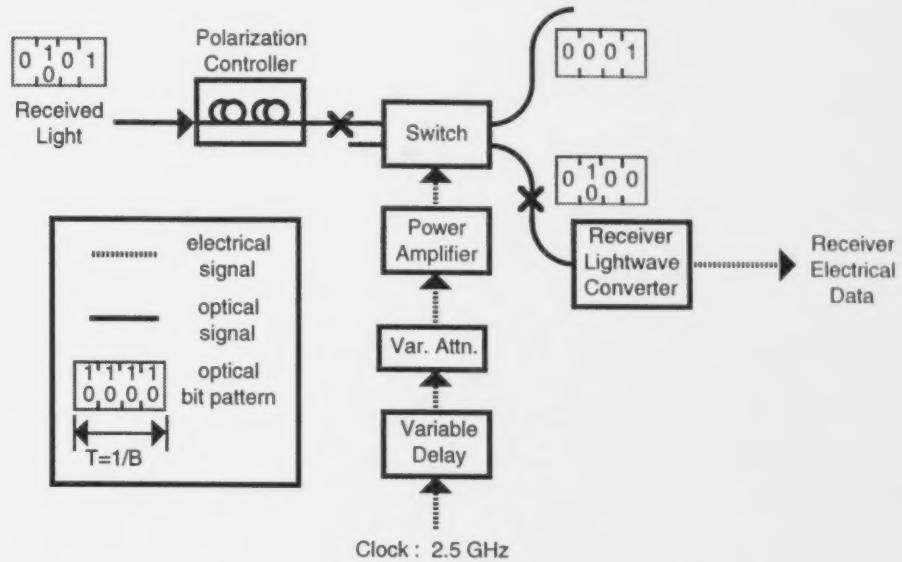

Figure 4.22 : OTDM Receiver

Proper timing of the electrical drive signal to the switch was accomplished in the same manner as for the transmitter. The timing adjustment was performed using lengths of semi-rigid coaxial cable for coarse adjustment, and a coaxial phase shifter for fine adjustment. Similarly, amplitude adjustment was again carried out by using a variable attenuator followed by a power amplifier.

After the optical demultiplexing stage, the return-to-zero (RZ) optical data signal is delivered to the receiver lightwave converter section to be converted to an electrical signal.

4.6.2 Receiver Lightwave Converter

The overall function of the lightwave converter block is to convert the optical signal to an electrical signal, and then to amplify and filter the data in order to optimize the signal to noise ratio. Figure 4.23 outlines the basic components of the converter.

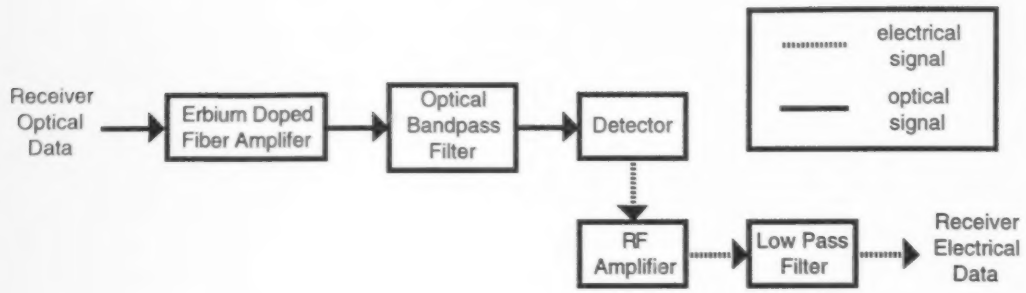

Figure 4.23 : Receiver Lightwave Converter

The optical data stream is first amplified optically using an erbium-doped fiber amplifier. The purpose of optical amplification is to improve the sensitivity of the receiver. As we will show later, the sensitivity of the overall receiver can be improved until noise introduced by the amplifier dominates the thermal noise of the detector. The amplified optical signal is then passed through an optical bandpass filter to limit the wideband noise introduced by the EDFA. The optical signal is then converted to an electrical current signal by the detector. The electrical data signal is amplified in order to overcome noise floor limits of downstream data analysis equipment. A low pass filter is also used after amplification to reduce the noise bandwidth of the signal. Important characteristics of each of these components will now be detailed in turn.

4.6.2.1 Erbium-Doped Fiber Amplifier

In optical digital transmission systems without optical amplifiers, the dominant source of noise is usually the thermal noise of the electrical pre-amplifier. The erbium-doped fiber amplifier is used to amplify the received optical data signal prior to detection, and thus improve the signal to noise ratio. The signal to noise ratio can be improved through optical amplification until the noise introduced by the optical amplifier overcomes the thermal noise floor of the pre-amplifier. An overview of EDFA operation and noise

considerations will be presented in this section. More detailed information on EDFAs can be found in the cited references.

The typical EDFA is composed of two wavelength division multiplexers, a section of erbium-doped fiber, and a pump laser as shown in Figure 4.24 below :

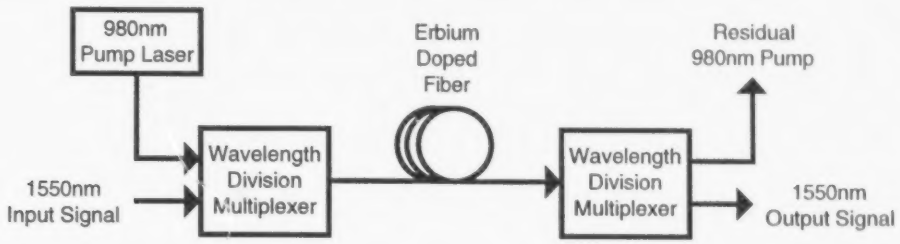

Figure 4.24 : Erbium Doped Fiber Amplifier Configuration

Conceptually, the operation of the amplifier is relatively simple. The 980 nm pump laser light and the 1550 nm input signal are multiplexed onto one fiber using the wavelength division multiplexer. The 980 nm pump light is absorbed by the erbium atoms in the erbium fiber. 1550 nm light passing through the erbium fiber is then amplified through the process of stimulated emission. The wavelength division multiplexer at the output separates the 1550 nm signal from the residual 980 nm pump light. The EDFA contributes additional noise to the signal through the process of spontaneous emission. The spontaneous emission is amplified as it travels through the erbium-doped fiber, and thus it is termed amplified spontaneous emission (ASE). The spectral distribution of ASE depends on a host of parameters including erbium-doped fiber properties, fiber length, pump power, and signal input level to name a few. Typically, the ASE spectrum is tens of nanometers wide with a peak at the gain peak wavelength of the EDFA.

The average optical ASE power from an erbium-doped fiber amplifier with gain G can be expressed as [46] :

$$P_{sp} = 2\, h\nu\, B_o\, N_{sp}\, (G-1) \qquad (4.4)$$

where B_o is the ASE bandwidth, N_{sp} is the spontaneous emission factor of the EDFA and hν is the photon energy. For the EDFA used in the OTDM receiver, the maximum achievable small signal gain was 21 dB at 1550 nm. This gain was achieved using a 980 nm pump laser current of 160mA, and the corresponding pump power coupled into the erbium fiber was about 50 mW.

The spontaneous emission factor for the amplifier was experimentally determined by measuring the ASE power and the small signal gain at 1550 nm. An optical filter with bandwidth of 1.4 nm was used to filter the ASE and the 2 dB loss of the filter reduced the effective gain of the amplifier to 19 dB. The measured ASE power in the 1.4 nm bandwidth was -23 dBm and thus the spontaneous emission factor was calculated as :

$$N_{sp} = P_{sp} / [\, 2\, h\nu\, B_o\, (G-1)\,]$$
$$= 1.42$$

It is important to note that B_o is the equivalent noise bandwidth, and that this parameter will be determined by the actual bandpass filter optical frequency response. We have used a value for B_o equal to the specified 3 dB bandwidth of the optical filter for calculation purposes.

In addition, the noise factor depends on several parameters [47]. These include the length and exact composition of the erbium fiber, the pump power, and the signal input power. For the purposes of calculation comparisons, however, we will assume that the spontaneous emission factor is constant with a value of 1.4.

When the amplified signal along with ASE is detected using a square law detector, the incoherent ASE beats with both itself and the signal producing baseband noise. The noise power contribution due to the ASE beating with itself in the detection process is termed spontaneous-spontaneous beat noise and is given by [48]:

$$i^2_{sp\text{-}sp} = 4\, B_o [\, N_{sp}\, \eta\, (G - 1)\, q\,]^2 \qquad (4.5)$$

where η is the detector quantum efficiency and q is the electronic charge. Expressions 4.4 and 4.5 assume that the EDFA gain spectrum is uniform with gain G and bandwidth B_o, and also that the ASE spectrum is uniform with bandwidth B_o. Since the detection process in effect performs a convolution of the ASE spectrum with itself, the baseband noise spectrum generated will be triangular in shape with a single-sided electrical bandwidth of B_o. An optical bandwidth B_o on the order of nanometers translates into an electrical bandwidth of terahertz, and so only the first few percent of this noise spectrum will impact systems operating in the gigahertz region. For gigahertz systems then, the spontaneous-spontaneous beat noise is essentially flat. Equation 4.5 represents the value of the spontaneous-spontaneous beat noise close to dc when the ASE spectrum is uniform with bandwidth B_o. In reality, however the spectral shape of the ASE is not exactly rectangular. Equations 4.4 and 4.5 are approximations, but they nonetheless provide a useful reference point for relative noise contribution analysis.

The noise component due to the ASE beating with the signal during detection is known as signal-spontaneous beat noise and is given by [48]:

$$i^2_{sig\text{-}sp} = \frac{4\, q^2}{h\nu}\, \eta^2\, P_d\, N_{sp}\, (G - 1)\, G \qquad (4.6)$$

where $h\nu$ is the photon energy and P_d is the input signal power to the optical amplifier. Expression 4.6 was arrived at by assuming again that the ASE spectrum is rectangular, and also that the signal spectrum is an impulse function. Under these conditions the beat-noise spectrum produced at baseband is uniform with bandwidth B_o and amplitude given by equation 4.6.

Both spontaneous-spontaneous beat noise and signal-spontaneous beat noise limit the signal-to-noise ratio improvements possible through optical amplification. A comparison of the relative receiver noise contributions from ASE and other sources will be presented later in section 4.6.2.5.

4.6.2.2 Optical Bandpass Filter

An optical bandpass filter is inserted immediately after the optical amplifier to band-limit the ASE. Assuming a perfectly frequency stable optical source, the ideal optical filter bandwidth has a bandwidth of twice the electrical signal bandwidth. For a 10 Gb/s data signal with a two-sided bandwidth of 20 GHz, the narrowest possible optical filter bandwidth is :

$$\Delta\lambda = \Delta f\left[\frac{\lambda^2}{c}\right] = 20\ \text{GHz}\left[\frac{1\ \text{nm}}{125\ \text{GHz}}\right] = 0.16\ \text{nm} \qquad (4.7)$$

In practical systems, neither the filter or the optical source is perfectly frequency stable, and thus some tolerance must be allowed. In addition, narrow optical filters are typically difficult and expensive to construct.

The filter used in the OTDM receiver was the JDS FITEL TB1500B tunable bandpass filter. The insertion loss of the filter was about 2.5 dB, the tuning range was 1530-1560 nm and the optical filter bandwidth was approximately 1.4 nm at 1550 nm. Due to the relatively wide filter bandwidth, the spontaneous-spontaneous noise contribution in the OTDM receiver will be considerably higher than the theoretical minimum achievable using a 0.16 nm filter.

4.6.2.3 Photodetector Characteristics

The photodetector used in the OTDM receiver was a BT&D model #PDC4310. The dc responsivity of the device was approximately 0.7 A/W and the specified 3dB bandwidth was 20 GHz. The frequency response of the photodetector was confirmed using two measurement techniques.

The first method involved detecting high levels of amplified spontaneous emission produced by an erbium-doped fiber amplifier. As described in section 4.6.2.1, the ASE produces essentially flat wide-band spontaneous-spontaneous beat-noise during the detection process. The frequency response of the detector is then reflected in the noise spectrum through changes in the quantum efficiency η, which is frequency dependent for the detector. If enough spontaneous-spontaneous beat noise can be produced to overcome the thermal noise floor, the noise spectrum containing the rolloff of the detector can be observed directly with a conventional RF spectrum analyzer. Figure 4.25 below shows the experimental setup used to measure the detector frequency response using the optical amplifier noise.

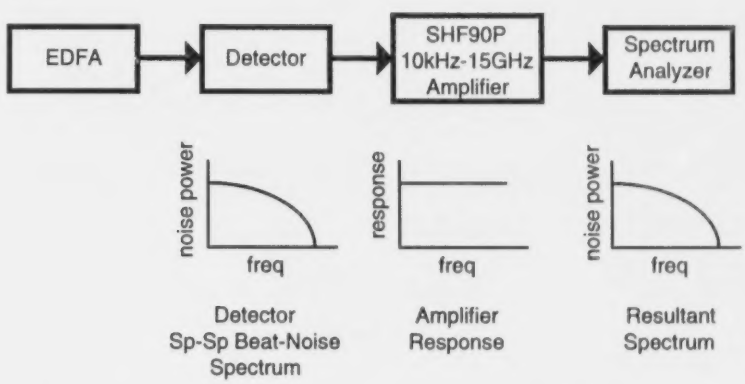

Figure 4.25 : Detector Frequency Response Measurement Setup Using EDFA Sp-Sp Beat Noise

The EDFA generates ASE which is mixed down to baseband as spontaneous-spontaneous beat-noise by the detector. At this point, the electrical noise spectrum includes the rolloff of the detector. The signal is boosted by a low-noise wide-band amplifier to bring the signal level up above the noise floor of the subsequent spectrum analyzer. The spectrum observed on the analyzer thus contains the rolloff of both the detector and amplifier, the shot noise due to the high average optical input power, and the thermal noise introduced by the amplifier.

The experiment was carried out with 0.0 dBm of ASE optical power incident on the BT&D detector. The pump current to the EDFA was 115 mA, and the small signal gain varied from greater than 30 dB at the 1535 nm gain peak to about 18 dB at the 1551 nm wavelength. Note that no optical bandpass filter was after the EDFA, and therefore the full ASE spectrum of perhaps 10 to 30 nm was incident on the detector.

The resulting total noise power at low frequencies (ie: 1-50 MHz) was approximately -123 dBm/Hz. A figure of -125 dBm/Hz for the spontaneous-spontaneous beat noise can be calculated using equation 4.5 with parameters B_o=20 nm, G=25 dB (average), N_{sp}=1.4, R=50 ohms, η=0.56, and multiplying the expression by the 26 dB gain of the SHF90P amplifier. The amplifier noise floor was measured at about -145 dBm/Hz and the shot noise was calculated to be about -144 dBm/Hz. Thus the spontaneous-spontaneous beat noise level was sufficiently high to dominate the other noise terms, and make detector frequency response measurement possible. The response of the amplifier was determined using a 40-GHz network analyzer. The detector response shown in Figure 4.26 was isolated by taking the total noise level as a function of frequency and then subtracting out the frequency response of the amplifier, the shot noise, and the thermal noise floor of the amplifier.

The frequency response in the Figure was limited to a useful range of approximately 13 GHz due to the sharp rolloff of the amplifier after 14 GHz. As the Figure shows, the 3dB electrical response of the detector is about 6 GHz and the 6 dB response is perhaps greater than 13 GHz. This result is substantially less than the 3 dB 20 GHz bandwidth reported in the device specifications. The discrepancy may be associated with the somewhat unreliable coupling between the fiber and the detector chip. The

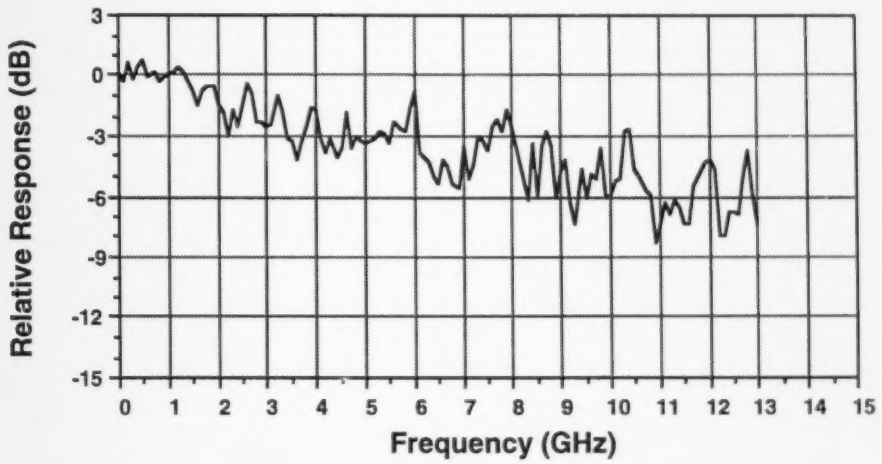

Figure 4.26 : Detector Frequency Response (EDFA Sp-Sp Beat Noise Method)

detector is fitted with a FC/PC mating sleeve, which facilitates removal of the FC/PC terminated fiber. The detector efficiency and bandwidth varied with different FC/PC connectors and tightness levels. It is possible that the detector bandwidth is reduced if the fiber is not optimally aligned with the detector illumination target. For the OTDM experiments, the input fiber was secured in a position which yielded high dc responsivity, and Figure 4.26 is the high frequency response result in that same position.

In any case, the 6 GHz measured bandwidth of the detector is sufficient for detection of the 2.5 Gb/s signals in the OTDM system. In fact, this bandwidth is sufficient to view the 10 Gb/s pulse shapes produced by the system.

A second technique was used to confirm the frequency response of the detector. This method involved external modulation of a cw laser source at single frequencies using an electro-optic modulator.

As presented in Chapter 2, the switching characteristic of a Mach-Zehnder interferometer is given by :

$$I_{out} = I_{in} \cos^2\left[\frac{\pi}{2}\frac{V_t}{V_\pi}\right] \tag{4.8}$$

where I_{in} and I_{out} are the input and output optical intensities respectively. It is assumed that a cw optical source is used as input to the modulator and therefore I_{in} is a constant. V_t is the electrical drive signal applied to the interferometer, and V_π is the half-wave voltage. Note that in general, V_π is a function of frequency. If the device is driven at a single frequency with an electrical signal of amplitude V_a and dc bias V_b then :

$$V_t = V_b + V_a\cos(2\pi ft) \tag{4.9}$$

The output intensity is then :

$$I_{out} = I_{in} \cos^2\left[\frac{\pi}{2}\frac{V_b + V_a\cos(2\pi ft)}{V_\pi}\right] \tag{4.10}$$

When this modulated optical signal is detected, the electrical power spectrum is composed of discrete frequencies at dc, f, 2f, 3f, etc. The relative levels of these harmonics depend on both the bias level and the amplitude of the RF drive signal. For an arbitrary RF drive level, midpoint biasing of the modulator is obtained at a level of $V_b=V_\pi/2$ and at this point the powers of both the fundamental and third harmonic are maximum and the power of the second harmonic is theoretically zero. It can be calculated that a maximum fundamental power level occurs when the peak to peak RF drive level is 1.172 V_π.

To obtain a constant amplitude modulated optical signal for use as a probe source to test the photodetector response, the bias level of the MZ modulator must be adjusted such that the second harmonic content of signal at the modulator output is minimum. The RF drive power must then be increased until the fundamental content of the signal is maximum. This process compensates for any frequency dependence of the V_π of the modulator. The frequency response of the detector can be determined by carrying out this procedure at a number of single tones, and noting the maximum power in the fundamental at each frequency. In addition, the frequency response of the modulator is determined by observing the relative increase in drive voltage or power required to produce the constant level optical test signal.

Figure 4.27 shows the experimental setup used to perform the single tone modulation tests using the UTP modulator and the BT&D detector.

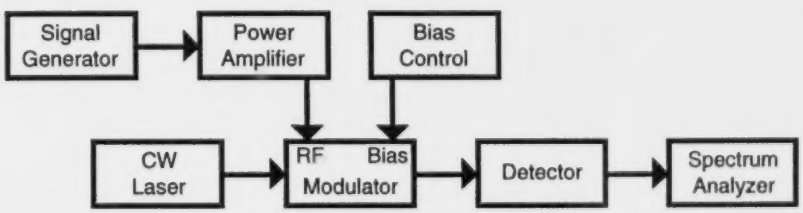

Figure 4.27 : Detector Frequency Response Measurement Setup Using Single Tone Modulation Technique

The modulator was driven at selected RF frequencies, and the detected electrical power spectrum was observed on the spectrum analyzer. The bias level was set so that the second harmonic content of the received signal was minimized, and the RF amplitude level was adjusted to maximize the power in the fundamental. The measurements were taken over the 10 MHz to 4.2 GHz frequency range which corresponded to the lower and upper limits of the available power amplifier required to drive the modulator. The rolloff in the power observed at the fundamental frequency as a function of frequency is shown in

Figure 4.28 along with the detector response as previously measured using the EDFA spontaneous-spontaneous beat-noise technique.

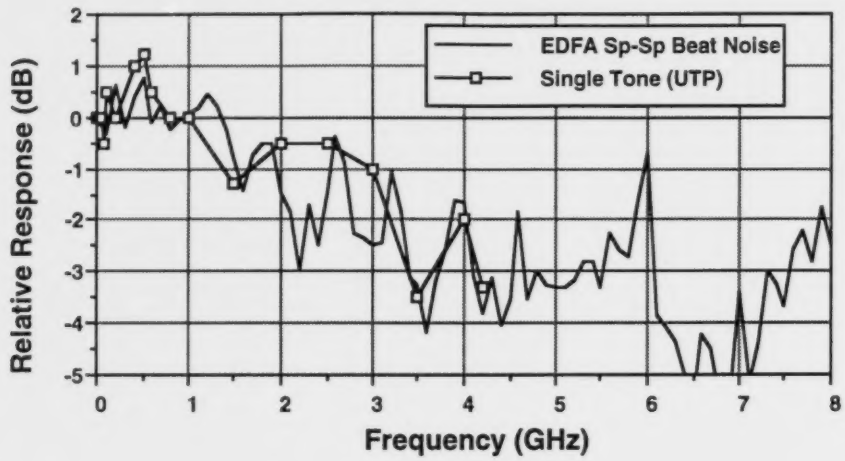

Figure 4.28 : Detector Frequency Response (Single Tone Modulation Method)

Over the frequency range of the power amplifier, the two techniques yield similar measurements of the detector frequency response. The detector responsivity at dc was measured to be about 0.7 A/W. The responsivity at relatively low rf frequencies (ie: 10-50 MHz) was also found to be about 0.7 A/W. The frequency dependence of the detector responsivity relative to the 0.7 A/W level can be determined using Figure 4.28 and dividing the vertical axis scale by two since Figure 4.28 measures RF power response of the detector.

4.6.2.4 Data Amplifier

A wide-band, low noise electrical amplifier follows the photodetector in Figure 4.23 in order to boost the signal for subsequent processing and/or data analysis equipment. For the purposes of the OTDM receiver, the amplifier should have flat response out to at least 2.5 GHz to properly amplify the 2.5 Gb/s data streams. For observation of the multiplexed 10 Gb/s signal, flat response out to about 10 GHz is preferred. The amplifier

should also have as low a noise figure as possible in order to maximize the signal-to-noise ratio.

The amplifier selected for the OTDM receiver was the SHF90P pulse amplifier. The typical specifications for the amplifier were 23 dB gain, 7 dB noise factor, and 15 GHz bandwidth flat to within +/- 1.0 dB. Experimentally, the gain was measured to be approximately 25 dB and the noise figure about 7 dB. The frequency response of the amplifier was measured directly using the 40 GHz network analyzer and is displayed in Figure 4.29.

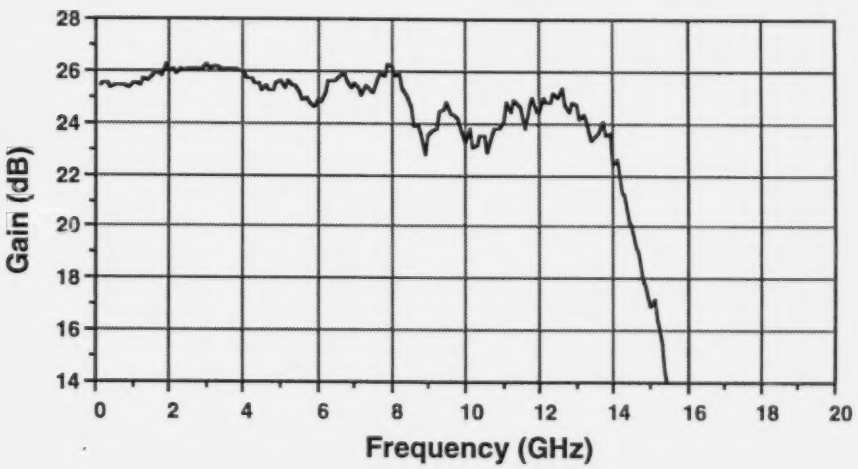

Figure 4.29 : SHF90P Frequency Response

The amplifier gain is flat to +/- 1 dB and the 3 dB bandwidth of the device is approximately 14 GHz.

4.6.2.5 Noise Limiting Lowpass Filter

After amplification by the pulse amplifier, the noise bandwidth of the signal is approximately 14 GHz. The 2.5 Gb/s data channel only requires approximately 2.5 GHz of information bandwidth, and thus a signal-to-noise ratio improvement can be obtained by adding a noise limiting low pass filter after the pulse amplifier. In addition, zero

intersymbol interference (ISI) can be theoretically achieved at the receiver using an appropriate filter.

The raised cosine pulse shape has been chosen as the target pulse shape since it is a common zero ISI pulse shape in digital transmission systems [49]. The raised cosine pulse shape is preferred since it provides zero ISI and minimum pulse ringing. The objective frequency content OBJ[f] of a pulse at the output of the filter is given by the raised cosine spectrum :

$$\text{OBJ}[f] = \cos^2\left(\frac{\pi f}{2 f_o}\right) \tag{4.11}$$

where f_o is the bit rate of operation. The filter frequency domain transfer function FILTER[f] multiplied by the remaining transfer functions in the system must produce the objective function as shown below :

$$\text{OTDM}[f] * \text{RCV}[f] * \text{AMP}[f] * \text{FILTER}[f] = \text{OBJ}[f] \tag{4.12}$$

where OTDM[f] is the spectrum of the OTDM data pulse falling on the detector. RCV[f] is the frequency response of the detector, and AMP[f] is the frequency response of the low-noise amplifier. The required frequency response for the filter is then given by :

$$\text{FILTER}[f] = \frac{\text{OBJ}[f]}{\text{OTDM}[f] * \text{RCV}[f] * \text{AMP}[f]} \tag{4.13}$$

The OTDM pulse shape after detection by a perfect detector is approximately a 1/4 duty cycle pulse. This pulse shape, along with the objective 2.5 Gb/s pulse shape is displayed in Figure 4.30.

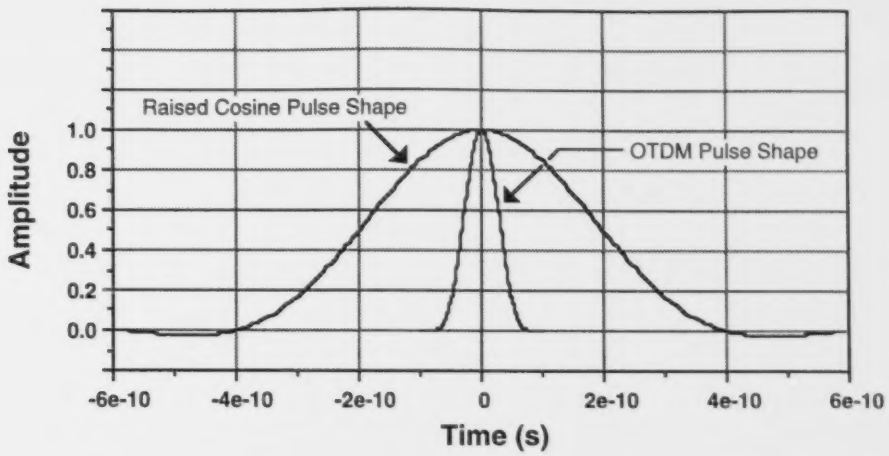

Figure 4.30 : OTDM and Target Pulse Shapes

The equivalent frequency domain content of the OTDM pulse, the objective pulse, and the concatenated responses of the detector and amplifier are shown in Figure 4.31.

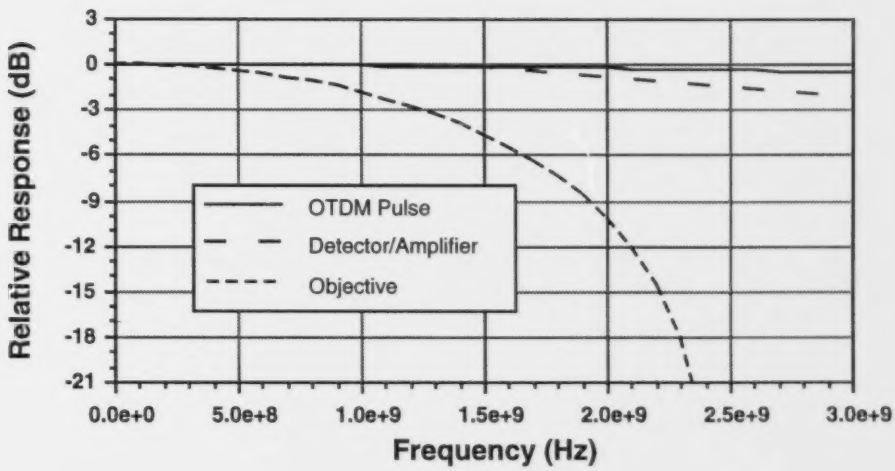

Figure 4.31 : OTDM, Receiver and Objective Pulse Spectrums

The ideal filter frequency response was calculated using equation (4.13) and the result was a frequency response almost identical to the objective response. The filter frequency response is approximately the same as the objective response because as Figure 4.31 shows, the OTDM pulse spectrum and the concatenated responses of the detector and

amplifier are broad and effectively flat over the region of the objective response. Thus, the exact shape of the OTDM pulse at the receiver is relatively unimportant in the design of the filter, and the ideal filter response is approximately given by the objective pulse frequency content.

The calculated ideal filter response, along with the 1.8 GHz, 5th order butterworth low pass filter used to approximate the ideal filter are shown below in Figure 4.32.

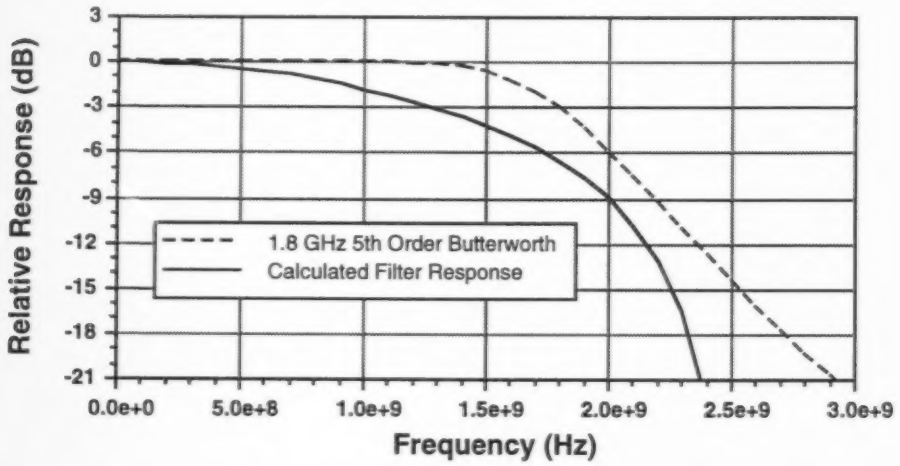

Figure 4.32 : Ideal Filter and Actual Implementation

The 1.8 GHz filter used in the OTDM receiver has a frequency response somewhat wider than the ideal characteristic and has a sharper initial rolloff. Gradual rolloff filters at gigahertz frequencies are not easy to manufacture, and the 1.8 GHz fifth order low pass version was one of the closest commercial approximations available.

4.6.2.6 Receiver Noise Considerations

The noise characteristics of several elements in the OTDM system have been discussed briefly in previous sections. This section will summarize the several sources of noise and their relative importance in the OTDM system. Five source of noise will be

considered and will be referred to the output of the photodetector in terms of noise current densities for comparison purposes.

The noise current density contribution due to relative intensity noise of the optical source is given by :

$$i_{rin}^2 = RIN\,(P_d\,r)^2 \qquad (4.14)$$

where RIN is the relative intensity noise, P_d is the optical power incident on the detector, and r is the detector responsivity. For the OTDM system, RIN=-134.5 dB/Hz, and r=0.7 A/W. The optical input power P_d will be varied in the analysis.

The thermal noise is given by:

$$i_{th}^2 = \frac{4\,k\,T\,F}{R} \qquad (4.15)$$

where $k=1.38*10^{-23}$ is the Boltzmann constant, T=300K is the resistor temperature, R=50 ohms is the resistance, and F=7 dB is the noise figure of the amplifier.

The shot noise contribution due to the signal and ASE is:

$$i_{shot}^2 = 2q\,[\,r\,(P_d + P_{sp})\,] \qquad (4.16)$$

where $q=1.6*10^{-19}$ is the electronic charge, and P_{sp} is the ASE optical power defined in equation (4.4).

The optical amplifier noise terms include the spontaneous-spontaneous beat noise and the signal-spontaneous beat-noise and are given by:

$$i_{sp\text{-}sp}^2 = 4\,B_o\,[\,N_{sp}\,\eta\,(G-1)\,q\,]^2 \qquad (4.17)$$

$$i_{sig\text{-}sp}^2 = \frac{4\,q^2}{h\nu}\,\eta^2\,P_{inEDFA}\,N_{sp}\,(G-1)\,G \qquad (4.18)$$

where B_o is the filtered ASE bandwidth, N_{sp} is the EDFA noise factor, G is the EDFA gain, and hν is the photon energy. For the EDFA in the receiver B_o=1.4 nm and N_{sp}=1.4. η is the detector efficiency and is related to the responsivity by η =r * (hν/q) = 0.56. The EDFA gain G will be a variable parameter. P_{inEDFA} is the optical input power to the EDFA and is related to P_d by P_d= G P_{inEDFA}.

The signal power is given by :

$$i_{sig}^2 = (P_d r)^2 \qquad (4.19)$$

With a noise bandwidth of B_e, the signal-to-noise ratio is given by :

$$SNR = \frac{i_{sig}^2}{\left[i_{rin}^2 + i_{th}^2 + i_{shot}^2 + i_{sp\text{-}sp}^2 + i_{sig\text{-}sp}^2 \right] B_e} \qquad (4.20)$$

For 10^{-9} bit error rate performance, the SNR for the system must be 15.5 dB. As a starting point we will calculate the required optical input power P_d to achieve a SNR of 15.5 dB if thermal noise is the only noise source. Evaluating (4.15) and (4.20) with an electrical noise bandwidth of B_e=2.5 GHz, the required optical input power for 10^{-9} error rate performance is approximately -17.5 dBm. The EDFA gain in the OTDM receiver has about 20 dB of gain at the 1551 nm wavelength. Therefore, a probable optical input power to the EDFA at 10^{-9} bit error rate performance is -37.5 dBm.

Figure 4.33 shows the calculated noise current densities of the five noise sources along with the total noise as a function of gain when the input power to the EDFA is fixed at -37.5 dBm.

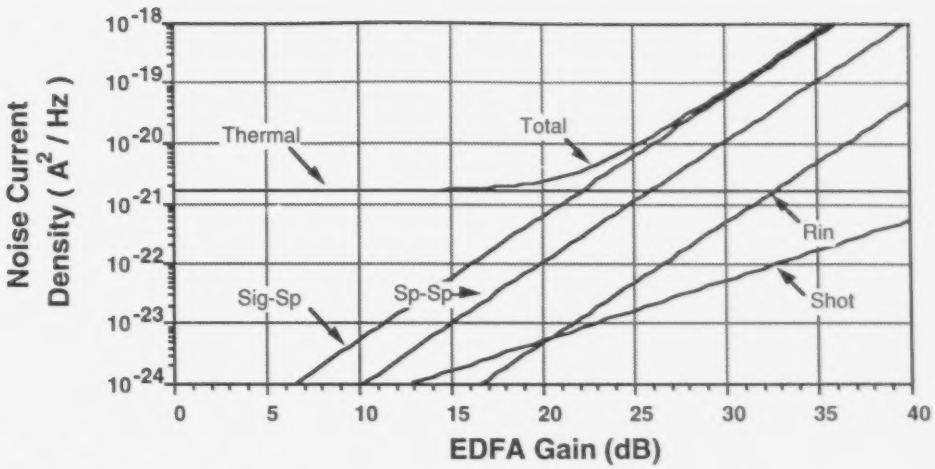

Figure 4.33 : Noise Levels vs. EDFA Gain

Figure 4.33 shows that the total noise in the system is determined primarily by the thermal noise for EDFA gains up to about 22 dB. For higher gains, the signal-spontaneous beat-noise dominates. Both signal power and the signal-spontaneous beat-noise power are proportional to the square of the EDFA gain. As a result, the composite signal-to noise ratio improves with increasing EDFA gain until the signal-spontaneous beat-noise starts to dominate. Figure 4.34 shows the signal-to-noise ratio as a function of EDFA gain for an EDFA signal input power of -37.5 dBm. As expected, the SNR improves until the signal-spontaneous beat-noise becomes the dominant noise factor.

Figure 4.34 also shows the SNR curves for P_{inEDFA} levels of -45 dBm and -30 dBm. For a higher input power, the SNR 'knee' occurs at lower EDFA gains since the signal-spontaneous beat-noise power is proportional to P_{inEDFA}. In addition, the SNR limit increases for increased input power since the signal power is proportional to the square of P_{inEDFA}. Note that for an input power of -45 dBm, 10^{-9} bit error rate operation is not possible for any EDFA gain since the SNR saturates below the required 15.5 dB level.

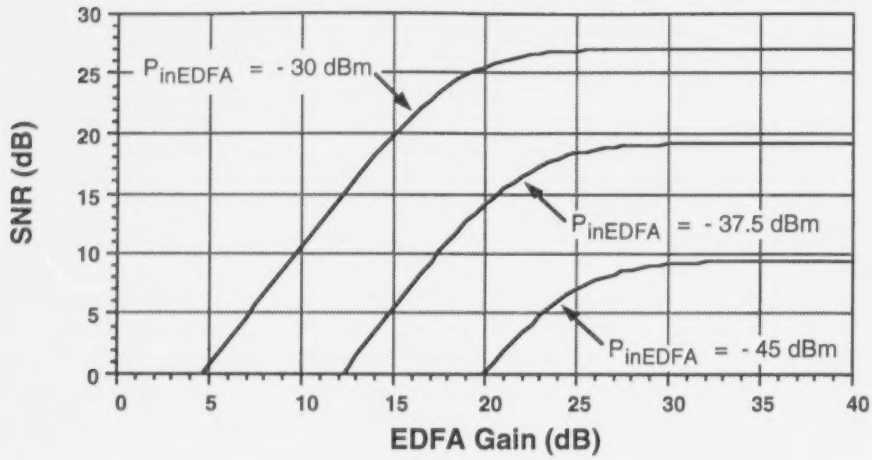

Figure 4.34 : Composite SNR vs. EDFA Gain

For the EDFA used in the OTDM receiver, the maximum achievable small signal gain was 19 dB at 1551 nm. Fixing the EDFA gain at this particular level, we can compare the relative levels of the various noise sources as a function of P_{inEDFA}. Figure 4.35 shows the noise current densities of the five noise sources along with the total noise as a function of signal input power for an EDFA gain of 19 dB.

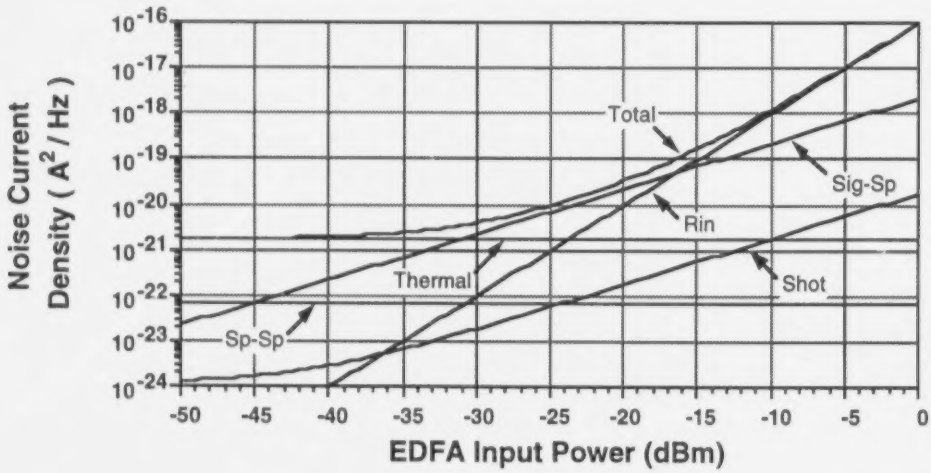

Figure 4.35 : Noise Levels vs. EDFA Input Power

For P_{inEDFA} levels of less than -32 dB, the total noise is primarily determined by thermal noise. Signal-spontaneous beat-noise dominates at input levels from about -32 to -16 dBm. At very high input levels above -15 dBm, the ultimate limit of laser RIN is encountered. Figure 4.36 shows the corresponding SNR levels for Figure 4.35.

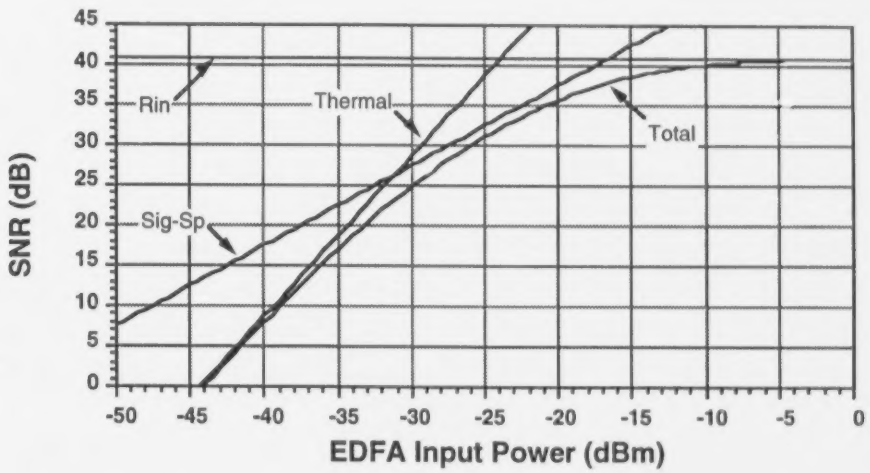

Figure 4.36 : SNR vs. EDFA Input Power

Again, we see that below -32 dBm input power levels, the SNR is dependent on the thermal noise. The slope of the composite SNR curve in this region is 2, which means the SNR is improved by 2 dB for every 1 dB increase in input power. In the -32 dBm to -16 dBm range, the SNR curve has a slope of 1 since signal-spontaneous beat noise is dominant. Finally, the SNR approaches the hard limit of 40.5 dB as laser RIN dominates at input levels above about -15 dBm.

The performance of the OTDM system will be assessed by determining the received optical power for which 10^{-9} bit error rate performance is achieved. Figure 4.36 shows that at a SNR of 15.5 dB or equivalently a bit error rate of 10^{-9}, the theoretical receiver sensitivity as referenced to the input of the EDFA is about -36 dBm. At this input power

level, the thermal noise is the dominant noise factor. Chapter 5 will compare the actual performance of the OTDM system with these theoretical results.

4.7 Summary

In Chapter 4, we have examined the experimental setup used to test the OTDM concept. The distributed component solution along with its associated problems was discussed first. The general system setup was presented in block form, and then a more specific configuration was selected for the purposes of detailed analysis. The components of the optical source were examined, and it was determined that the relative intensity noise and linewidth of the source met the requirements for information limited 10 Gb/s OTDM operation.

A specific OTDM transmitter arrangement which multiplexed two 2.5 Gb/s channels was presented. Characteristics of the modulator and switches, the passive optics, and the high speed electronics were then investigated. In addition, the coherence problem introduced by the discrete approach to the OTDM layout was discussed along with a potential solution.

Finally, operation of the OTDM receiver was considered. The optical demultiplexing process was discussed for the two channel OTDM configuration. The optical detection process was then examined in some detail. Characteristics of the optical amplifier, filter, photodetector and subsequent electronics were presented. A brief analysis of the several sources of noise, and their relative significance in the OTDM system was conducted. Having completed the examination of the individual components, we will now move on to discuss the performance of the OTDM system as a whole.

5.0 OTDM System Experimental Results

In Chapter 4 we were concerned with characterization of the individual components of the OTDM system. Having completed this task, we now turn to examine the performance of the system as a whole. In this Chapter we first discuss the rationale for implementing a scaled down experimental version of the OTDM system. Experimental results pertaining to optical time division multiplexing of two 2.5 Gb/s channels are then presented. This is followed by an investigation of multiplexing the 2.5 Gb/s data channel with the two immediately adjacent channels. Finally, we move on to examine the polarization multiplexing experiments. Polarization multiplexing was investigated as an alternative to OTDM. Comparisons between computer simulation results and experimental results are made to evaluate the accuracy of the computer model.

5.1 Demonstrating the OTDM Concept

Ideally, we would like to evaluate the performance of the OTDM system in its complete form. This would involve modulating and fully multiplexing and demultiplexing four 2.5 Gb/s channels. It would be beneficial to examine both the spectral properties and eye patterns of the composite OTDM signal. In addition, system concerns involving power budgets and determination of the receiver sensitivity degradation as a result of the complete OTDM process would be valuable.

For an OTDM system composed of integrated electro-optic devices, experimental operation of a four channel system would likely be possible, since the combined optical power loss in the transmitter and receiver might be in the 15-20 dB range. However, for the distributed experimental system examined here, four concatenated switches and a modulator may result in a 30 dB power loss in the transmitter alone if the average device loss is 6 dB. In the receiver, two more switches are required which adds another 12 dB of

loss. The total losses in the link due to the electro-optic devices alone will be approximately 42 dB. These losses were considered too high to perform measurements on the system even with the availability of the three optical amplifiers at TR Labs. In addition, economical considerations and concern over the coherency problem of the distributed system discussed in Chapter 4 suggest that a scaled down version of the OTDM system is more appropriate for the experimental work stage.

To demonstrate the OTDM concept, three configurations of the system were tested experimentally. The first system examined was presented in Chapter 4 during analysis of the individual OTDM components. This configuration of the system multiplexed two 2.5 Gb/s channels using 10 Gb/s type pulses positioned 2 bit times apart. The results of this pseudo-5 Gb/s back-back OTDM system are presented in Section 5.2. The second system was designed to show multiplexing of directly adjacent channels in the system, and is presented in Section 5.3. The third system used polarization multiplexing instead of time division multiplexing to combine the adjacent channels. The insertion loss penalties associated with polarization multiplexing were substantially less than for OTDM, and thus 100 km transmission experiments were possible. The polarization multiplexing system and the fiber transmission results are explored in Section 5.4.

5.2 Two Channel OTDM Results

The two channel OTDM transmitter and receiver configurations were presented earlier in chapter 4. This configuration demonstrated the pulse forming, modulation, and multiplexing aspects of the system at a 5 Gb/s throughput rate using pulses ultimately intended for 10 Gb/s applications. This section presents details of the experimental results obtained with the two channel system. In Sections 5.2.1 and 5.2.2, the transmitter and receiver configurations are revisited, and the experimental pulse shapes and eye diagrams obtained at various points in the system are examined. Finally, the bit error rate

performance of the system in the back to back configuration is determined, and the impact of the two channel OTDM approach on receiver sensitivity is assessed.

5.2.1 Transmitter Layout and Pulse Shapes

The experimental setup of the transmitter used to perform optical multiplexing of two 2.5 Gb/s type channels is shown in figure 5.1 below. This layout is identical to the transmitter of figure 4.7 except that the electronic details have been omitted, and an erbium-doped fiber amplifier has been added between the first two switches to compensate for losses.

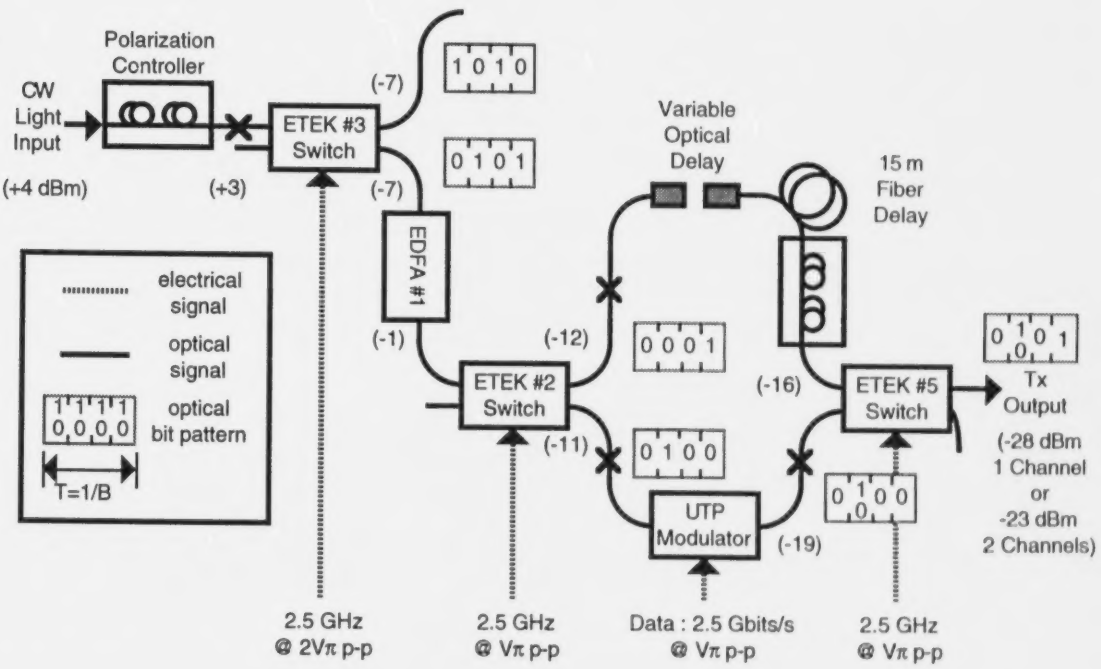

Figure 5.1 : 2 Channel OTDM Transmitter

The average power levels in terms of optical dBm units are indicated in brackets in the figure. The operational details for the optical amplifier blocks including EDFA #1 in figure 5.1 are included in appendix 5A. The EDFA has a relatively low 6 dB gain because

it is operated under highly saturated conditions. Including the optical amplifier, the losses in the transmitter are still extremely high. If $0\ \frac{1}{0}\ 01$ modulation of the +4 dBm cw optical source was performed in a zero-loss system, the optical powers in the modulated $0\ \frac{1}{0}\ 00$ channel and the unmodulated 0001 channel would be -5 dBm and -2 dBm, respectively. The total power at the transmitter output would then be about -0.2 dBm. In the actual transmitter presented in figure 5.1, the total power at the transmitter output is about -23 dBm. Thus, the excess loss of the OTDM two channel transmitter is a hefty 23 dB, even after including the 6 dB gain of the optical amplifier.

Having presented the physical layout of the transmitter, we will now turn to examine the transmitter pulse shapes obtained using this system. The modulated optical waveforms were observed using the lightwave converter and a high-speed sampling oscilloscope as shown in figure 5.2 below.

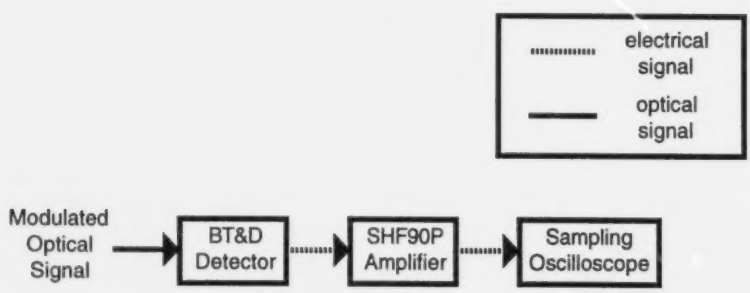

Figure 5.2 : Waveform Acquisition Equipment

The modulated optical signal was detected using the BT&D photodetector. The detector output was amplified using the SHF90P amplifier, and then delivered to the Hewlett Packard 34 GHz bandwidth sampling oscilloscope via a low loss connection cable. The sensitivity of the oscilloscope was approximately 1 mV, and the thermal noise floor of the SHF90P amplifier was measured at 4.5 mV rms or about 10 mV peak-to-peak visually.

Referring back to figure 5.1, the first switch was driven with a switching voltage amplitude of $2V_\pi$ at 2.5 GHz. The switch was biased at the minimum intensity crossover point for the lower branch. As shown in the $2V_\pi$ switching simulations in chapter 3, this bias condition will produce a 5-Gb/s train of relatively wide pulses on the lower output branch of the switch. A 5 Gb/s train of relatively narrower pulses is expected on the upper output branch.

The actual waveforms at the lower and upper outputs of the first switch were obtained using the sampling scope and are shown in figures 5.3 and 5.4, respectively. In addition, the theoretical waveforms calculated using the simulation software are overlaid in the figures for comparison purposes. The computer model was modified to take into account the frequency response characteristics of the BT&D detector and the pulse amplifier, as well as the frequency and phase response of the ZHL42W power amplifier used to drive the modulator.

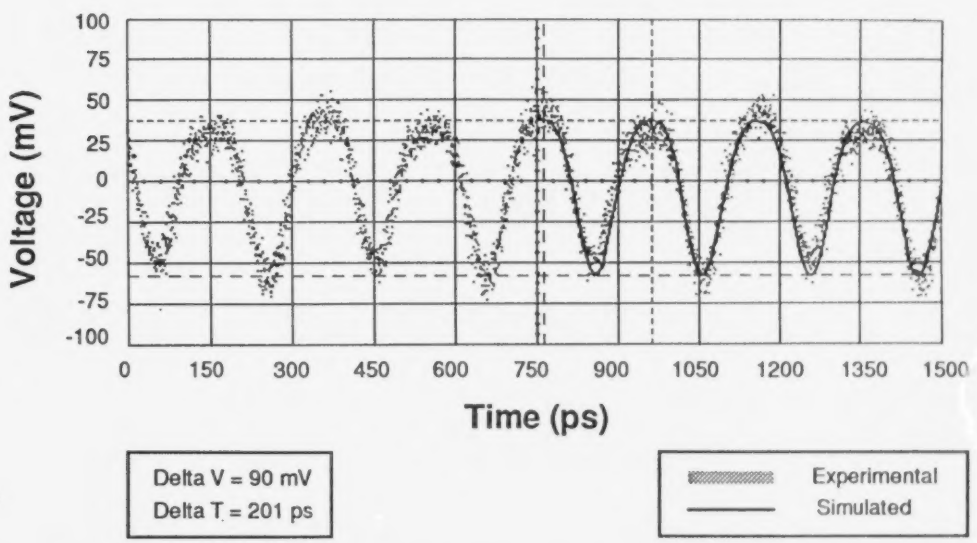

Figure 5.3 : ETEK #3 Switch Lower Output Waveform

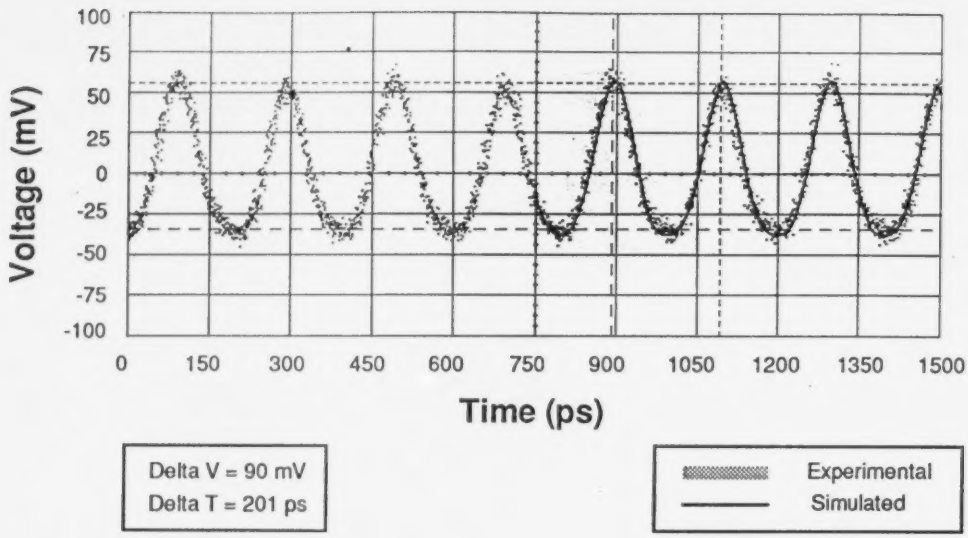

Figure 5.4 : ETEK #3 Switch Upper Output Waveform

As expected, a 5 Gb/s pulse train was produced from the lower branch, and a noticeably narrower pulse train was produced from the upper branch. The width of the wider pulses as measured at the midpoint was approximately 125 ps, while the width of the narrower pulses was about 75 ps. Note that the traces acquired by oscilloscope are thickened by the 10 mV peak-to-peak thermal noise. Qualitatively, the simulated waveforms agree well with the experimental result.

The second switch was driven by a 2.5 GHz tone with voltage amplitude V_π. In order to demultiplex the 5 Gb/s stream properly, the drive signal was delayed in time so that the peaks and valleys of the applied signal arrived with the peaks of the optical input signal. In this way, the 5 Gb/s input pulse train was divided into two 2.5 Gb/s streams. The upper and lower switch output waveforms as obtained by the sampling scope are displayed in figures 5.5 and 5.6 along with the simulated pulse shapes.

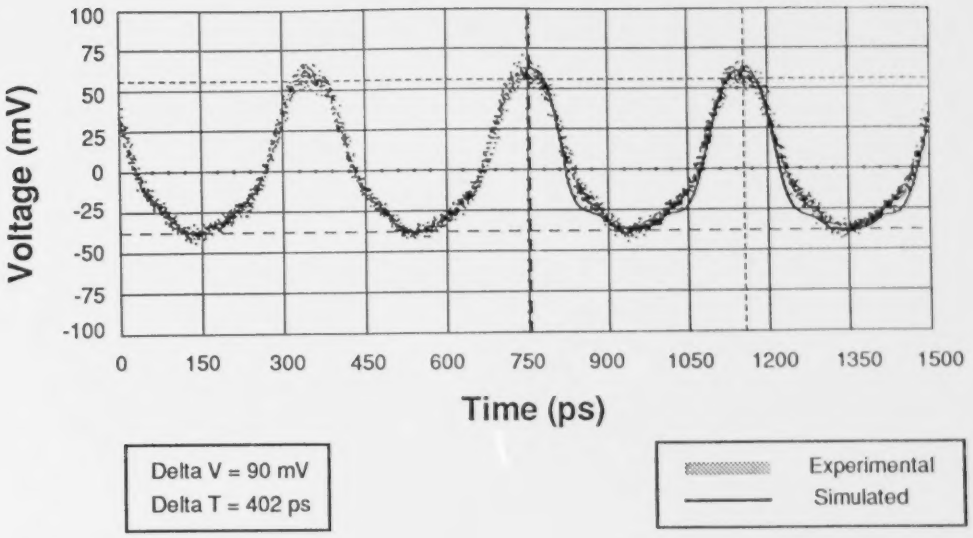

Figure 5.5 : ETEK #2 Switch Upper Output Waveform (Wide Pulse Train Utilized)

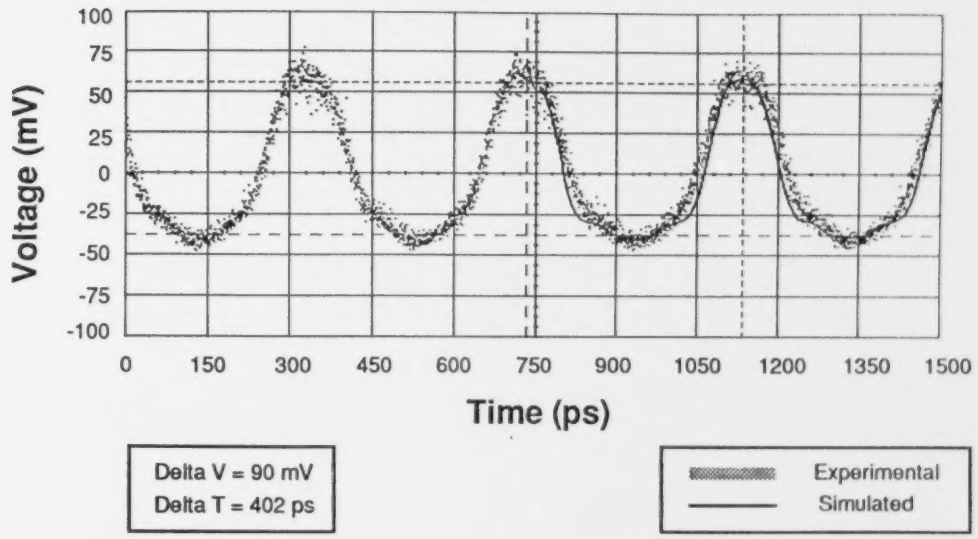

Figure 5.6 : ETEK #2 Switch Lower Output Waveform (Wide Pulse Train Utilized)

As we expect the waveforms from the two outputs of the second switch are approximately the same in shape since a symmetric drive signal is applied to the switch.

The half-maximum pulse width is approximately 150 ps in both figures. Here, the simulated pulse trains are similar in shape to the experimental results.

The modulator was driven with the 2^7-1 length pseudo-random 2.5 Gb/s sequence at the full 12.6 peak-to-peak switching voltage using the ZHL42W power amplifier. Figure 5.7 shows the eye diagram obtained at the output of the modulator using the sampling scope. The simulated eye diagram at this point agrees well with the experimental result.

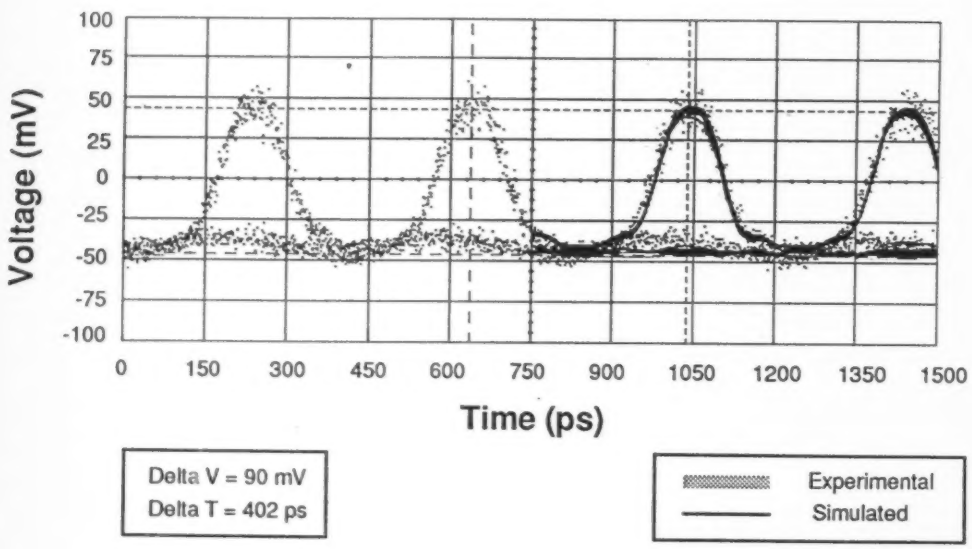

Figure 5.7 : UTP Modulator Eye Pattern

In Section 4.4.4.3, it was estimated that the power amplifier introduced approximately a 15 to 20 percent variation in the level of 'ones' and 'zeros' in the 2.5 Gb/s data signal. It was calculated that this distortion would translate into approximately a 5 to 10 percent variation in the levels of the modulated optical intensity signal. Comparing figures 5.5 and 5.7, we see that both the one and zero levels are in fact slightly broader in the modulated case as a result of the amplifier distortion. In the unmodulated case, the width of the sampled trace is approximately 10-15 mV p-p due to thermal noise, while in

the modulated case, the width increases to about 20 mV p-p. Therefore, the modulated trace has been thickened by about 5-10 mV or 5-10 percent of the amplitude as a result of the amplifier distortion.

The third switch labelled ETEK #5 in the transmitter was driven by a 2.5 GHz tone with voltage amplitude V_π. In order to properly multiplex the two 2.5 Gb/s streams, the drive signal was delayed in time such that the peaks of the applied voltage signal arrived with the peaks of the optical input signals. In addition, the timing of the upper optically pulsed channel relative to the modulated channel was controlled via the variable optical delay as shown in figure 5.1. The resulting 5 Gb/s multiplexed eye diagram was observed using the sampling scope and is shown in figure 5.8 along with the simulated eye diagram.

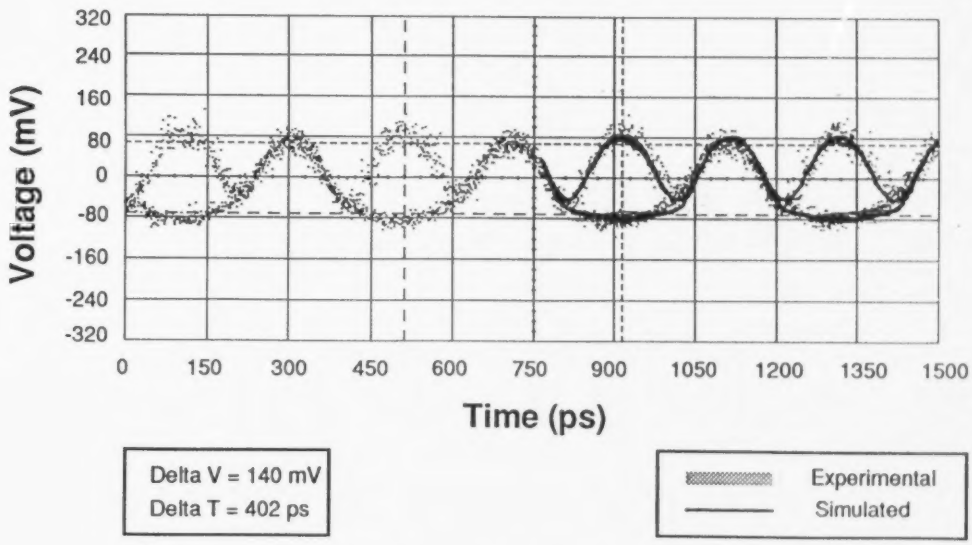

Figure 5.8 : 2 Channel Multiplexed Eye Pattern

The modulated and continually pulsed channels are readily identified, and the simulated pulse pattern agrees well with the measured result. The multiplexed signal of figure 5.8 exhibits approximately 30-40 mV of noise on top of the signal. This additional

noise is a result of the incoherent addition of the partially overlapping optical pulses, as discussed in Section 4.4.3.2.

5.2.2 Receiver Layout and Pulse Shapes

The experimental setup of the two channel receiver is shown in figure 5.9 below.

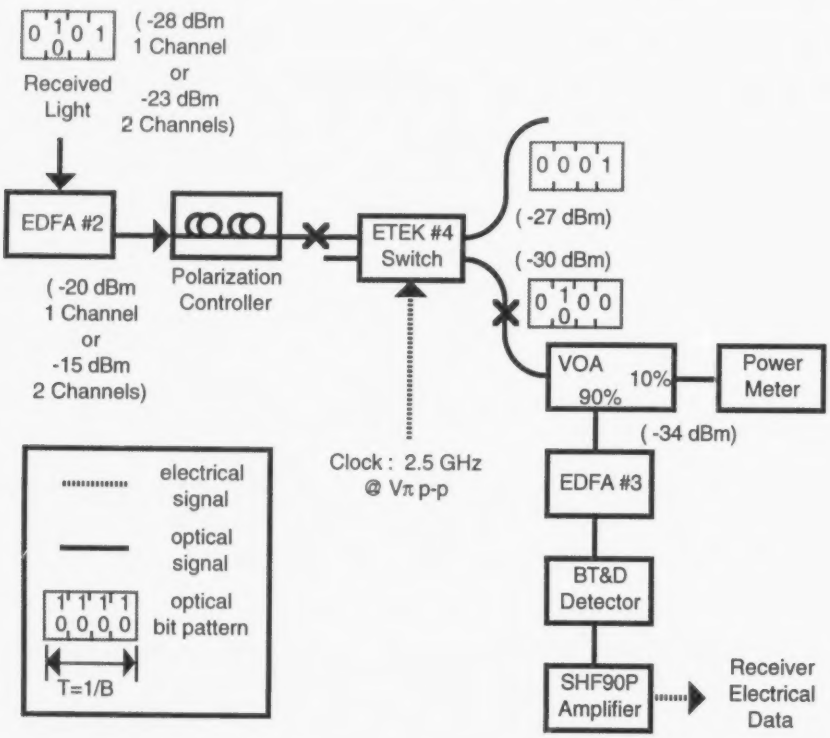

Figure 5.9 : 2 Channel Receiver Configuration

This receiver configuration differs from the receiver of figure 4.22 in that another EDFA has been introduced at the front end of the system in order to boost the signal to compensate for the loss of the demultiplexing switch. The operating condition details of the EDFA blocks 2 and 3 are given in appendix 5A. In addition, a 90/10 percent splitting variable optical attenuator was added to facilitate convenient optical power monitoring. The

optical power level measurements in the diagram are indicated in brackets for both the one and two channel cases.

The single optical demultiplexing switch was driven at 2.5 GHz at the full switching voltage. The drive signal was delayed electrically such that the modulated channel was gated to the lower output of the switch. The demultiplexed eye diagram observed at the lower output of the switch is shown in figure 5.10, along with the overlaid simulated result. For comparison purposes, the experimental and simulated data eye diagrams in the absence of the second pulsed channel are presented in figure 5.11.

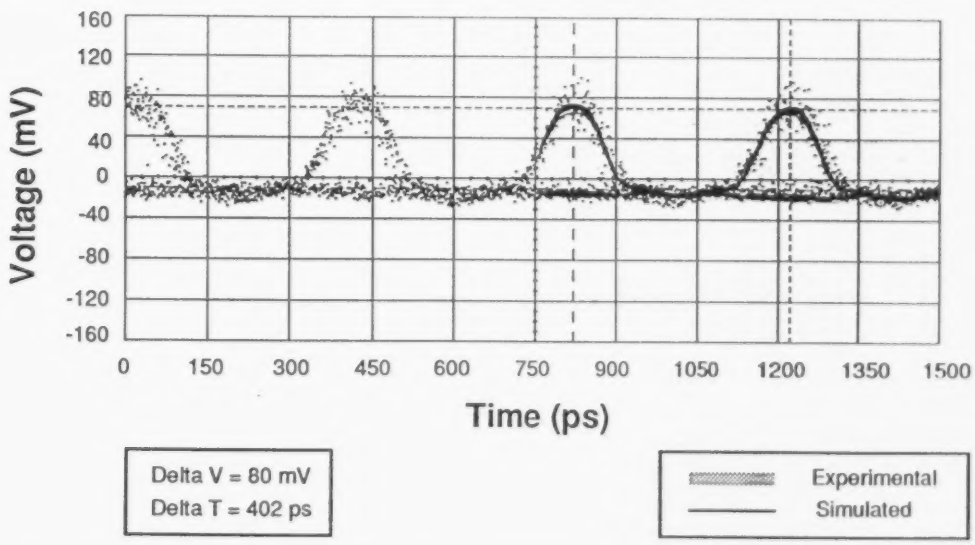

Figure 5.10 : Received Eye Diagram - 2 Channels Transmitted

The eye diagrams of both figures were obtained at an optical power of -30.0 dBm referenced to the input of EDFA #3. Note that to obtain this power level, the variable optical attenuator was bypassed. Qualitatively, it is apparent from figures 5.10 and 5.11 that the presence of the second pulsed channel produces some additional closure in the data eye.

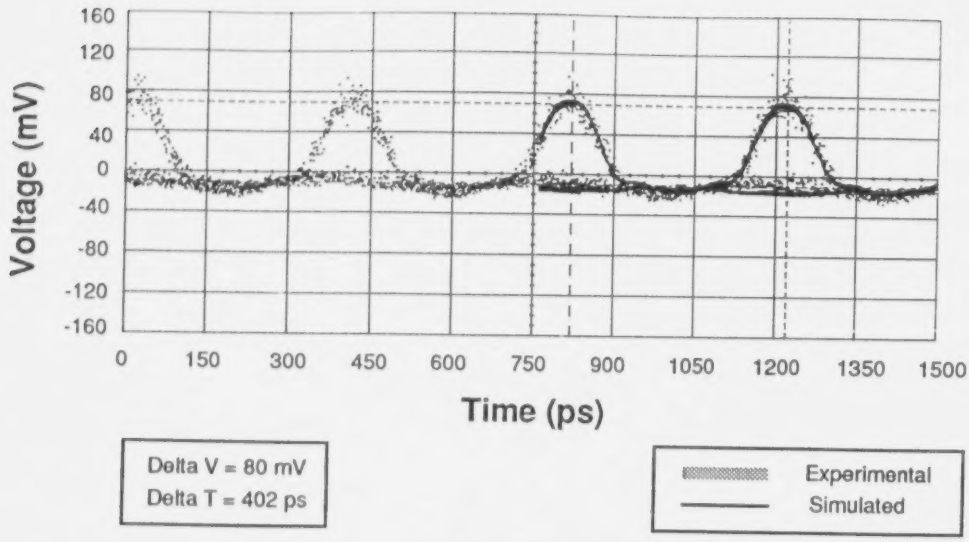

Figure 5.11 : Received Eye Diagram - 1 Channel Transmitted

The 1.8 GHz low pass filter described earlier in Section 4.6.2.5 was inserted after the SHF90P amplifier to band-limit the noise. The low pass filter lowers the noise bandwidth to approximately 1.8 GHz, and broadens the relatively narrow data eye. Figure 5.12 displays the filtered data eye diagram observed using the sampling oscilloscope.

Compared with the unfiltered eye, the filtered eye diagram is significantly broadened and spreads out to occupy essentially the entire bit period. The simulated eye diagram is overlaid in the figure and is in very good agreement with the experimental result.

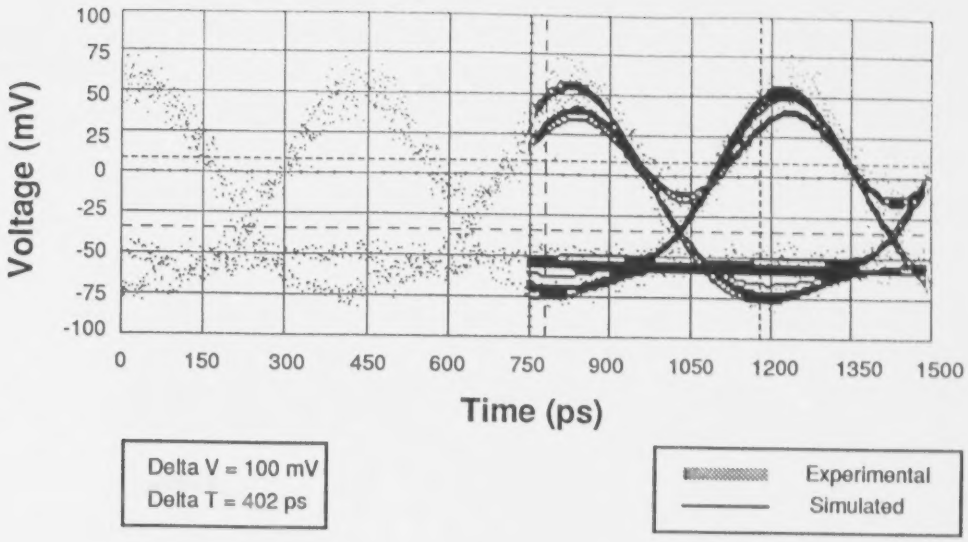

Figure 5.12 : Filtered Eye Diagram

5.2.3 Two Channel OTDM Bit Error Rate Measurements

To assess the penalty associated with 2 channel OTDM in a more quantitative manner, bit error rate measurements were conducted on the data channel in both the absence and presence of the second pulsed channel. The bit error rate measurements were conducted using the receiver of figure 5.9 followed by an additional stage of electrical amplification before termination in the bit error rate test set as shown in figure 5.13.

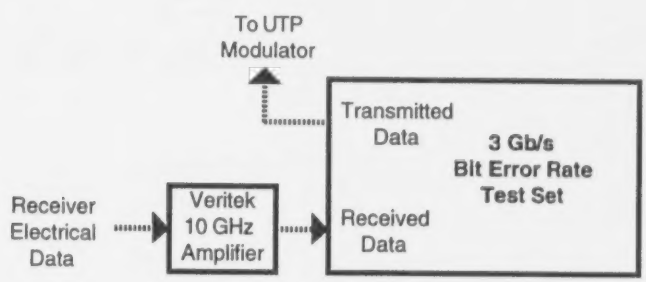

Figure 5.13 : 2 Channel OTDM Bit Error Rate Measurement Setup

The Veritek amplifier was used to boost the level of the electrical signal to levels required by the error rate test set. The bandwidth of the amplifier was approximately 3 kHz to 10 GHz, the RF gain was 32 dB, and the 1 dB gain compression output power was +17 dBm (3 V p-p). The 0.1-3 Gb/s error rate test set was composed of a Hewlett Packard 70841A Pattern Generator and a 70842A Error Detector module. The minimum input signal level required by the error detector was 500 mV peak-to-peak. In addition, the input electronics to the error detector had a 3 dB bandwidth of about 3 GHz. The exact frequency response of the input electronics was not available, and so an optimum filter was not designed for the bit error rate measurements. Thus, the filtering function was accomplished by the input electronics of the error detector, and the 1.8 GHz low pass filter was not used.

Figure 5.14 shows the bit error rates measured for the modulated channel as a function of received power.

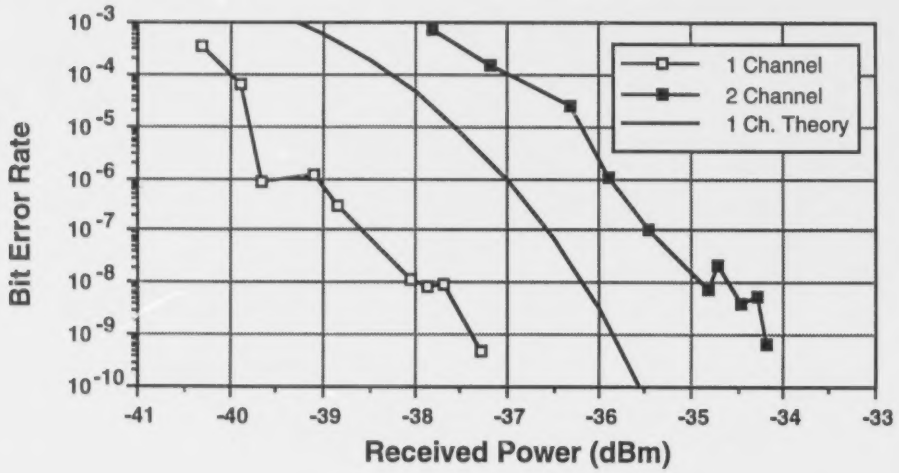

Figure 5.14 : 2 Channel OTDM Bit Error Rate Measurements

Received power is referenced to the input of EDFA #3 of the receiver. The '1 Channel' result in the figure was obtained by simply disconnecting the pulsed channel in

the transmitter. For this single 2.5 Gb/s data channel, we can see from figure 5.14 that the 10^{-9} bit error rate receiver sensitivity is approximately -37.5 dBm. Recall that in Section 4.6.2.5 the 10^{-9} bit error rate receiver sensitivity was calculated at -36 dBm. Thus the experimentally determined receiver sensitivity is close to the theoretical value. One possible reason that the experimental value is approximately 1.5 dB lower than the theoretical value is that the equivalent noise bandwidth at the error rate test set is slightly lower than the 2.5 GHz assumed in the calculations. This is possible, since the specified 3 dB bandwidth of the input electronics for the test set was 3 GHz. Another possibility is that the noise factor of the SHF90P amplifier is slightly lower in the 0-3 GHz range than the 7 dB nominal specification over the full 15 GHz range. Finally, the experimental data pulse shape received by the bit error rate test set was highly return-to-zero in nature. For the theoretical curve shown here, the pulse shape was not considered. Therefore, the slightly return-to-zero characteristic may also account somewhat for the discrepancy.

In addition, the experimentally determined -37.5 dBm receiver sensitivity level indicates that dominant source of noise in the system is likely thermal noise as predicted in the calculations. This hypothesis was confirmed by a visual inspection of the noise present on the modulated waveform using the high speed oscilloscope. The thermal noise was measured at about 250 mV peak-peak at the output of the Veritek amplifier with no optical input to the detector. The noise present on the modulated waveform was also measured at 250 mV peak-to-peak. Thus, the OTDM receiver operated in the thermally noise limited regime. As predicted in chapter 4, both the optical signal input power to the receiver EDFA (-37.5 dBm) and the EDFA gain (19 dB) are too low to make signal-spontaneous beat-noise a dominant source of noise.

The '2 Channel' measurement in figure 5.14 was observed when the pulsed channel was connected in the transmitter. Comparing the two curves, we can see that introduction of the second channel results in an approximate 3 dB penalty in receiver

sensitivity. This penalty arises from the coherent addition of the partially overlapping pulses in the two channels as described in Section 4.4.3.2. Intersymbol interference may also introduce a penalty, and it is important to point out that this ISI issue is separate from the coherence issue. Differentiating the two penalties may be valuable in future experiments. Note that it was just possible to obtain 10^{-9} bit error rate performance in the transmitter-receiver back-to-back arrangement due to the high losses of the optical switches. Thus, actual fiber transmission experiments with the two channel OTDM system were not possible. Introduction of additional EDFAs after the transmitter would likely permit OTDM transmission experiments.

5.3 Three Channel OTDM - Multiplexing Adjacent Channels

The two channel system demonstrated optical time division multiplexing of two 2.5 Gb/s channels placed two bits apart yielding a throughput rate of 5 Gb/s. To demonstrate the feasibility of 10 Gb/s transmission, a second system was conceived to multiplex the modulated data channel with the two directly adjacent pulses. Sections 5.3.1 and 5.3.2 will present the transmitter and receiver configurations and examine the pulse shapes obtained using the OTDM system to interleave 3 adjacent channels. Section 5.3.3 will investigate the bit error rate performance of the system and assess the impact of the OTDM process on receiver sensitivity.

5.3.1 Transmitter Layout and Pulse Shapes

Referring back to the transmitter of figure 5.1, adjacent channel multiplexing was accomplished by taking the 1010 pulsed upper output of the ETEK #3 switch and feeding it through the optical delay path into the upper input of the ETEK #5 multiplexing switch. The 0001 channel output from the ETEK #2 switch used in the two channel case was simply disconnected. This modified experimental setup of the transmitter used to perform optical multiplexing of three adjacent 2.5 Gb/s type channels is shown in figure 5.15.

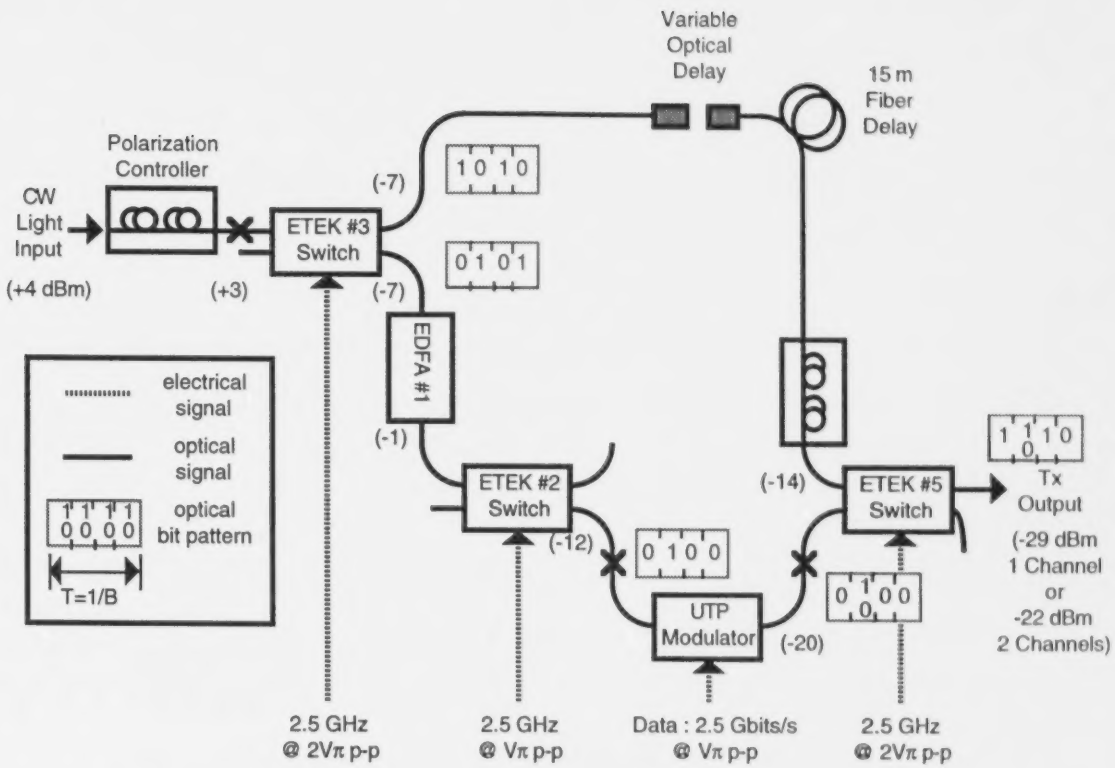

Figure 5.15 : 3 Channel OTDM Transmitter Configuration

The average power levels in terms of optical dBm units are indicated in brackets in the figure. The operational details for the optical amplifier EDFA #1 in the figure are included in appendix 5A. Similar to the two channel OTDM system, the excess loss in the 3 channel OTDM transmitter of figure 5.15 is extremely high at about 24 dB.

The drive signals applied to the switches #2 and #3 and the UTP modulator were the same as for the two channel OTDM case. The waveforms obtained at the upper output of the ETEK #3 switch and the UTP modulator are also the same and were shown in figures 5.3 and 5.7, respectively.

The ETEK #5 multiplexing switch was driven with a 2 V_π peak-to-peak 2.5 GHz sinusoidal signal to accomplish multiplexing of the data channel with the 5 Gb/s continually pulsed stream. The bias level and electrical delay to the switch were set such that the wide gating portion of the drive signal corresponded to the peaks of the narrow pulses in the 5 Gb/s pulsed channel. As was shown in Section 3.5 of Chapter 3, when this particular drive signal is applied to the final multiplexer, the output pulse train will be composed of identically shaped pulses. The timing of the pulsed channel relative to the modulated channel was controlled via the variable optical delay. The resulting pseudo 10 Gb/s multiplexed eye diagram was observed using the sampling scope and is shown in figure 5.16 along with the simulated eye diagram.

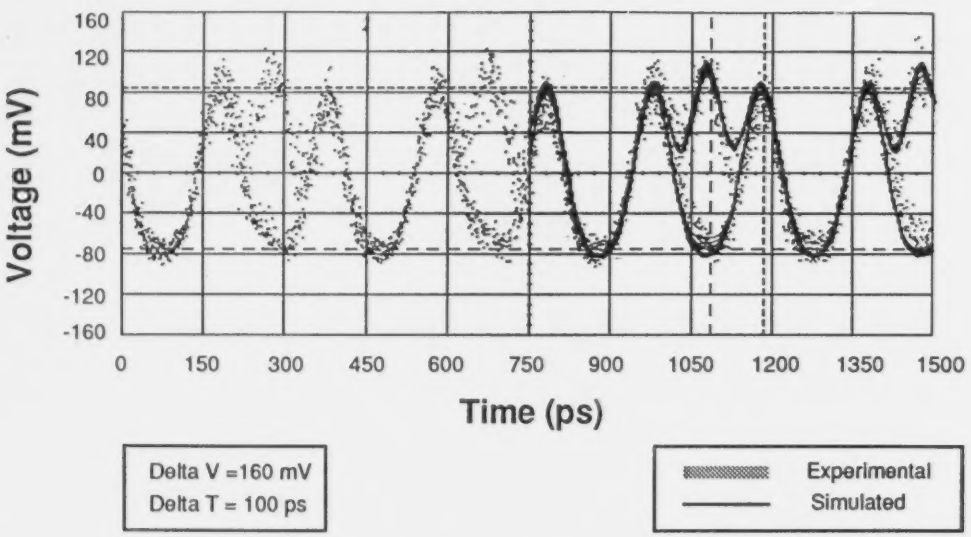

Figure 5.16 : 3 Channel Multiplexed Eye Pattern

The modulated and continuously pulsed channels are readily identified. The simulated waveform agrees well with the experimental result, and the partial return-to-zero characteristic of the pulse pattern expected due to the OTDM process is clearly visible.

5.3.2 Receiver Layout and Pulse Shapes

The experimental setup of the three channel receiver is shown in figure 5.17 below.

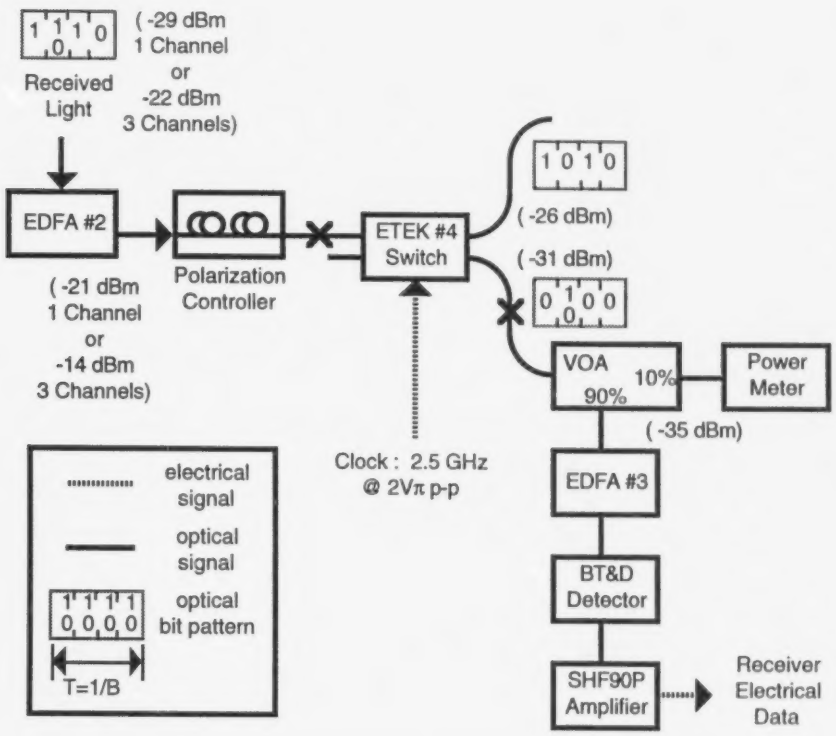

Figure 5.17 : 3 Channel Receiver Configuration

The EDFA#2 and #3 blocks are identical to those in the 2 channel receiver, and the EDFA operating conditions are given in appendix 5A. The optical power level measurements in the diagram are indicated in brackets for both the one and three channel cases.

The single optical demultiplexing switch was driven at 2.5 GHz at twice the switching voltage. The drive signal was delayed electrically such that the modulated channel was gated to the lower output of the switch, and the two pulsed channels were gated to the upper output of the switch. The wide part, or endpoints of the 2 V_π gating

function was used to demultiplex the data channel. The demultiplexed eye diagram observed at the lower output of the switch is shown in figure 5.18, along with the overlaid simulated result. For comparison purposes, the experimental and simulated data eye diagrams in the absence of the two adjacent pulsed channels are presented in figure 5.19.

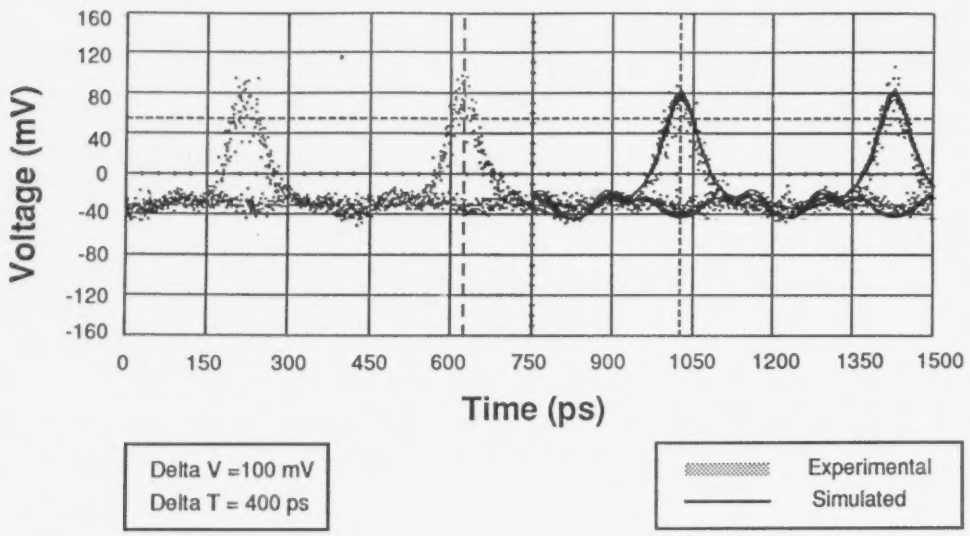

Figure 5.18 : Received Eye Diagram - 3 Channels Transmitted

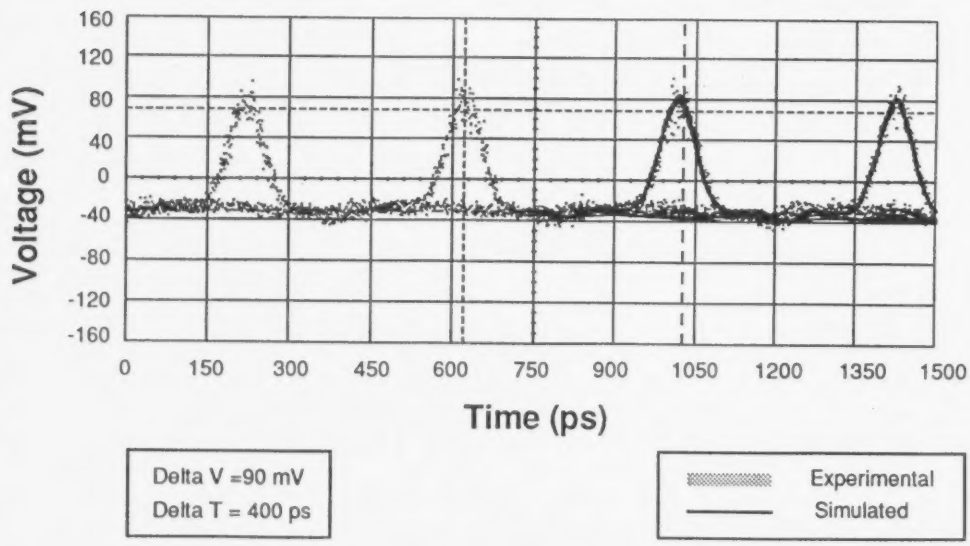

Figure 5.19 : Received Eye Diagram - 1 Channel Transmitted

The eye diagrams of both figures were obtained at an optical power of -31.0 dBm referenced to the input of EDFA #3. To obtain this power level, the variable optical attenuator was bypassed. Comparing figures 5.18 and 5.19, it is apparent that the presence of the adjacent pulsed channels produces detectable closure in the data eye. Time varying fluctuations on the order of seconds were observed in the 3 channel demultiplexing case. These fluctuations were significantly greater than those observed in the 2 channel OTDM case. The increased fluctuations are suspected to be brought about by the increased pulse overlap and associated coherence effects of the 3 channel system. Figure 5.18 does not show this phenomenon well, and therefore the bit error rate measurement will be used to assess the performance degradation more precisely.

The narrow part, or the midpoint of the $2V_\pi$ gating function was also used to demultiplex the data channel in a second experiment. This involved simply moving the bias point on the ETEK #5 switch down by V_π and adjusting the signal timing. Slightly narrower pulse shapes were obtained for the data channel due to the narrower gating function, and approximately the same eye closure was observed.

5.3.3 Three Channel OTDM Bit Error Rate Measurements

To quantitatively assess the receiver sensitivity penalty associated with 3 channel OTDM, bit error rate measurements were conducted on the data channel in both the presence and absence of the two adjacent pulsed channels. The bit error rate measurements were conducted using the receiver of figure 5.17 followed by the amplification stage and error rate test set as was shown in figure 5.13 for the 2 channel OTDM measurements.

Figure 5.20 shows the bit error rates measured for the modulated channel as a function of received power.

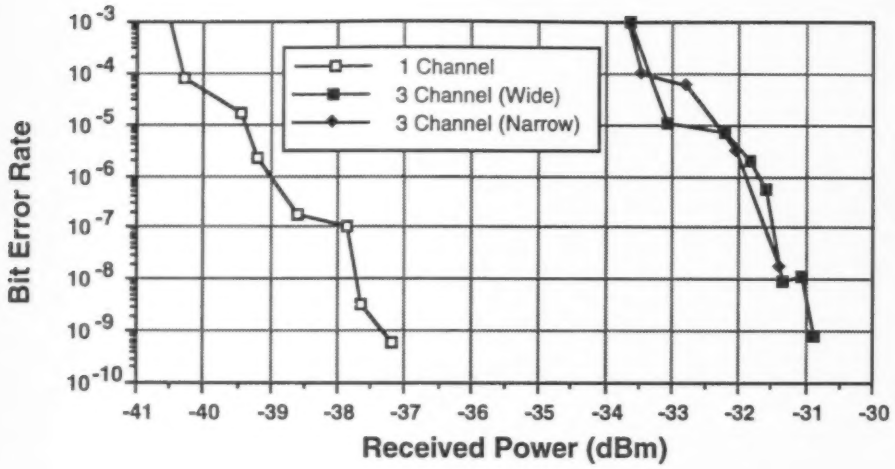

Figure 5.20 : 3 Channel OTDM Bit Error Rate Measurements

As was the case for the 2 channel OTDM measurement, the received power was measured at the input to the receiver EDFA. The '1 Channel' result in the figure was obtained by disconnecting the pulsed channels in the transmitter. The 10^{-9} receiver sensitivity is approximately -37.5 dBm. As we would expect, this level is about the same as for the 2 channel OTDM - '1 Channel' measurement, and is also close to the -36 dBm value calculated in chapter 4.

The '3 Channel (Wide)' measurement was obtained when the pulsed channel was re-connected, and the wide portion of the $2V_\pi$ gating function was used to demultiplex the data channel. The '3 Channel (Narrow)' result was observed when the narrow portion of the $2V_\pi$ gating function was employed. Comparing the three curves, we can see that introduction of the 2 pulsed channels results in approximately a 6-7 dB penalty in receiver sensitivity. The penalty for 3 channel OTDM operation is about 3-4 dB worse than for the 2 channel case. This is not surprising since there is significantly more coherent addition of light in the overlapping regions of immediately adjacent pulses. Again, intersymbol interference also contributes to the penalty, and this is a separate issue from the coherence

issue. These two penalty contributions have not been separated here, and it may be informative to do so in further work.

In addition, we see that the bit error rate performance is essentially the same for wide or narrow demultiplexing of the data stream. It was not possible to obtain 10^{-9} bit error rate performance for the narrow demultiplexing case due to optical power limitations.

Figure 5.20 presents the average bit error rates measured. It is worthwhile to point out that the instantaneous bit error rate as reported by the test set in a 0.1 second interval fluctuated significantly. For example, at an input power level of -33 dBm for the wide gated 3 channel OTDM case, it was observed that the 0.1 second interval bit error rate fluctuated between $5.0 * 10^{-5}$ and 0. The average error rate over tens of seconds was much more stable and was measured at about $1.0 * 10^{-5}$. For the '1 channel' case where the two adjacent bits are disconnected, the instantaneous error rate was observed to fluctuate within a much narrower range. At an input power level of -39.5 dBm for the single channel case, the instantaneous error rate varied from about 10^{-4} to 10^{-6} around an average of 10^{-5}. This difference between the stabilities of the 0.1 second error rates for the 1 and 3 channel OTDM systems indicates that some process with a time constant on the order of the 0.1 second interval is at work in the 3 channel system. This fluctuation phenomenon was also noted earlier in the eye diagrams of the 3 channel system in Section 5.3.2. It is hypothesized that the coherence effects in the 3 channel system contribute to this instability, however, further work is required to identify the exact cause of this phenomenon.

5.4 Polarization Multiplexing of Adjacent Channels

A second method was used to multiplex the 5 Gb/s pulsed stream with the 2.5 Gb/s data stream. Two optical polarization splitter/combiner devices were available at TR Labs, and these devices were used to perform polarization multiplexing and demultiplexing on the

two streams. The term polarization division multiplexing (PDM) was used to describe this type of signal combination.

Polarization division multiplexing is a relatively new concept, and only a couple of papers have been published concerning the technique. Previous experimental PDM research includes a 4 Mb/s transmission system using polarization maintaining fiber [50], and both 4 Gb/s [51] and 8 Gb/s [52] systems using standard single-mode fiber. As well, a theoretical examination of PDM has been conducted [53].

In our system, PDM theoretically solves the intersymbol interference and pulse overlap problems associated with OTDM since the polarized channels were orthogonal. In addition, the variable optical delay was no longer strictly necessary since pulse overlap was in theory no longer an issue.

Aside from these positive issues, polarization multiplexing also raised some new concerns. First, the pulse overlap problem was not completely avoided since the polarization multiplexers did in reality have finite crosstalk. Second, the polarization stability and the polarization leakage over long fiber distances was unknown. Hill, Olshansky, and Burns noted in earlier work [51] that the state of polarization did indeed wander after travelling over 45 km of fiber, and that the polarization crosstalk penalty increased with transmission distance. As will be shown in the subsequent experimental studies conducted on polarization multiplexing, it was found that in spite of these concerns, relatively long distance transmission in the laboratory environment was possible using PDM.

5.4.1 PDM Transmitter Configuration and Pulse Shapes

The transmitter was configured with a polarization combiner in place of the last ETEK #5 switch as shown in figure 5.21. The 1 dB insertion loss of the polarization

multiplexer was relatively low compared to the ETEK #5 switch and therefore no optical amplifier was required between the first and second switching stages.

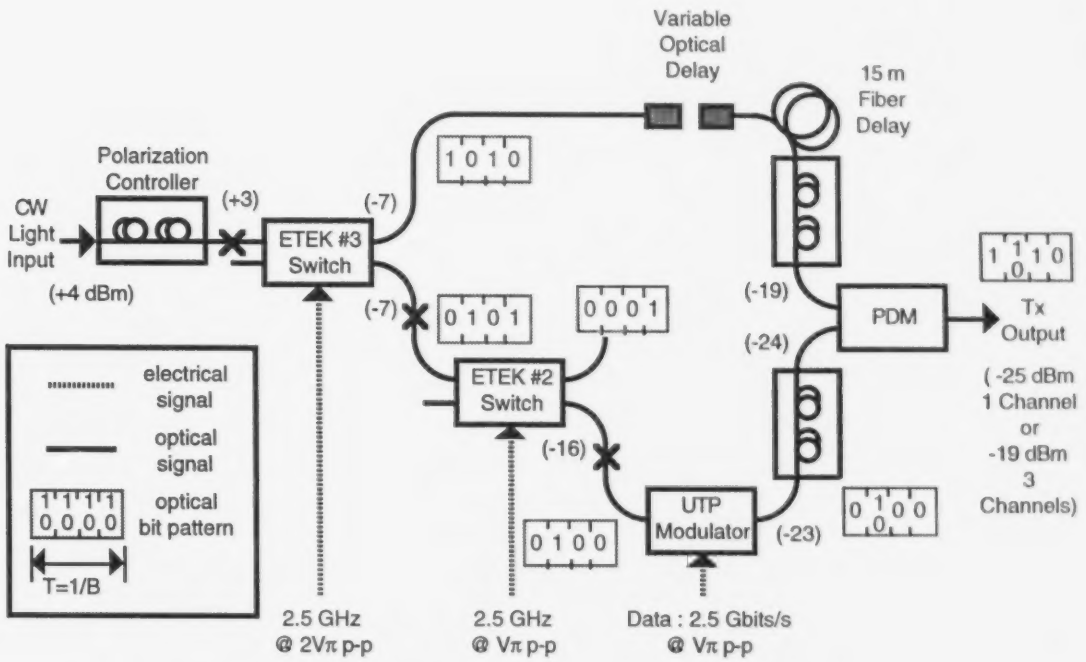

Figure 5.21 : PDM Transmitter Configuration

Polarization controllers were inserted in both the modulated signal and pulsed stream optical paths in order to match the polarizations of the signals with the required orthogonal polarization states required at the polarization multiplexer input. The variable optical delay adjustment was left in place to allow time interleaving of the two streams for the purposes of waveform analysis. The variable optical delay can further reduce the effect of the already small polarization crosstalk by centering the modulated channel between the two pulsed channel peaks. The variable optical delay also conveniently functioned as a variable optical attenuator when the axial positions of the two lenses were offset.

The polarization multiplexed output of the transmitter was observed using the sampling scope, and is shown in figure 5.22a. For comparison purposes, a part of the actual data stream is also shown in figure 5.22b.

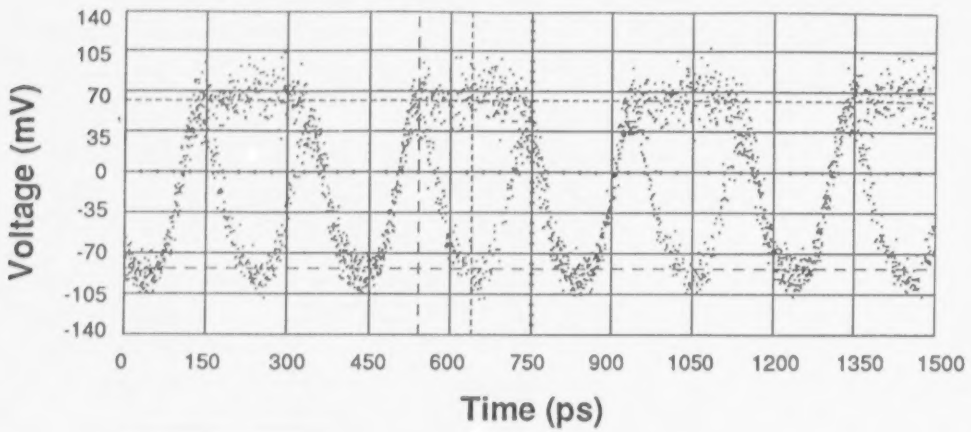

Figure 5.22a : PDM 3 Channel Eye Diagram

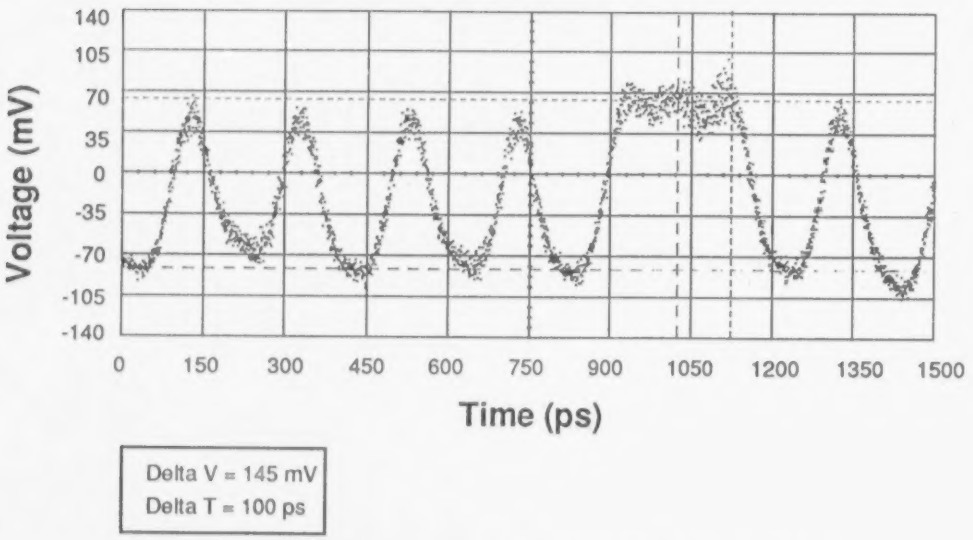

Figure 5.22b : PDM 3 Channel Data Pattern

From these two figures, we can clearly see both the 5 Gb/s type pulsed channel as well as the modulated data channel which lies in between the peaks of the pulsed channel. Comparing the 3 Channel PDM eye diagram with the 3 Channel OTDM eye diagram of figure 5.16, we observe that the PDM eye does not possess the partial return-to-zero characteristic. The PDM generated 3 channel signal is essentially non-return-to-zero since no light is gated out of the system by the polarization multiplexer.

It is important to remember that the two waveform figures above are plots of the optical intensity of the multiplexed signal since the detector translates the incident optical intensity into an electrical current. The pulsed and data channels are in fact orthogonal in polarization, and thus the apparent 'eye' pattern is only a result of the detection process.

If the optical outputs of the first switch are exchanged, the modulated channel will utilize the narrow pulses, while the 5 Gb/s pulsed channel will be composed of relatively wider pulses. Figures 5.23a and 5.23b show the eye diagram and sample data pattern for the narrow pulse modulated channel polarization when multiplexed with the wider pulsed channel.

Comparing Figures 5.22 with Figures 5.23, we see that the narrow data channel eye diagram is slightly narrower as we expect, and again no return-to-zero characteristic is present.

5.4.2 PDM Receiver Configuration and Pulse Shapes

The polarization demultiplexing portion of the link, or the PDM receiver is shown in figure 5.24.

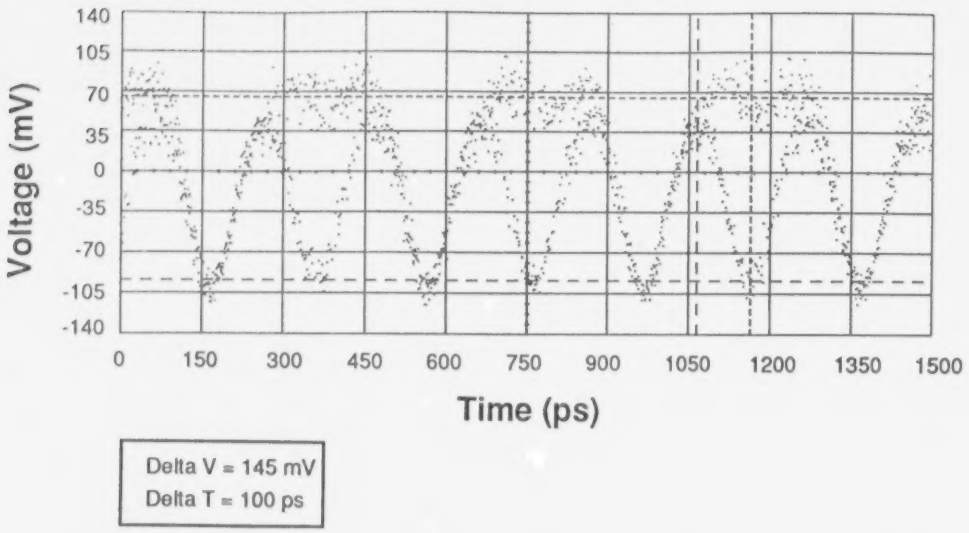

Figure 5.23a : PDM 3 Channel Eye Diagram - Narrow Data Pulse

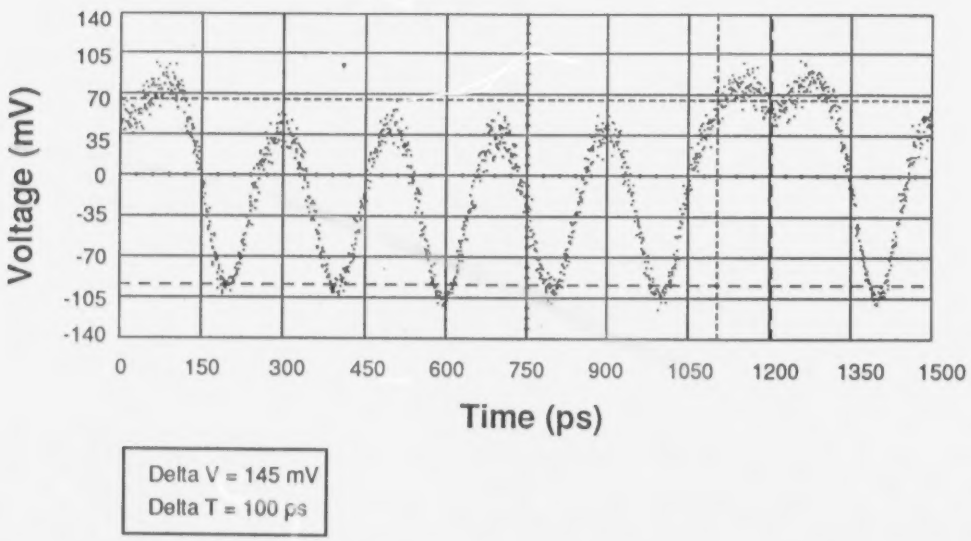

Figure 5.23b : PDM 3 Channel Data Pattern - Narrow Data Pulse

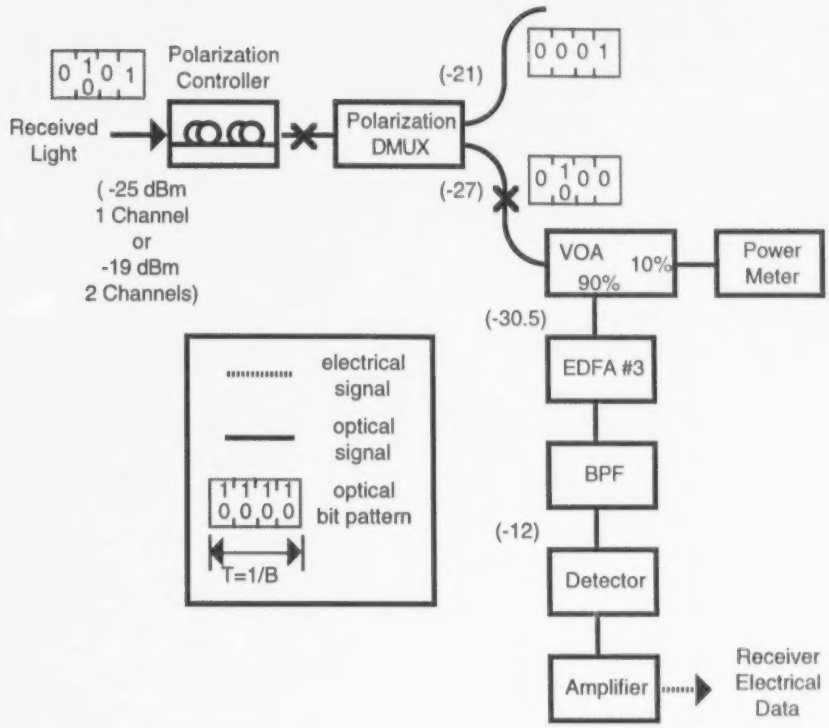

Figure 5.24 : PDM Receiver Configuration

The optical power levels are indicated in brackets for the case where the transmitter and receiver are placed back-to-back, and the variable optical attenuator is set to zero attenuation. It was found that the optical crosstalk observed between the two channels at the demultiplexer output was very sensitive to the polarization controller setting. The controller setting was optimized by disconnecting the modulated channel in the transmitter and then minimizing the power monitored in the modulated channel polarization at the receiver. Near the optimal setting, it was found that the crosstalk from the pulsed channel into the data channel output of the polarization demultiplexer was lower than -30 dB.

With the setting of the polarization controller optimized, the eye diagram of the data channel at the polarization demultiplexer output was observed using the sampling scope. Qualitatively, it was observed that the data eye diagram was virtually the same in both the

presence and absence of the pulsed channel on the orthogonal polarization. For the case where the modulated data channel utilizes the wide pulse shape in the transmitter, figure 5.25 shows the eye diagram at the receiver after polarization demultiplexing.

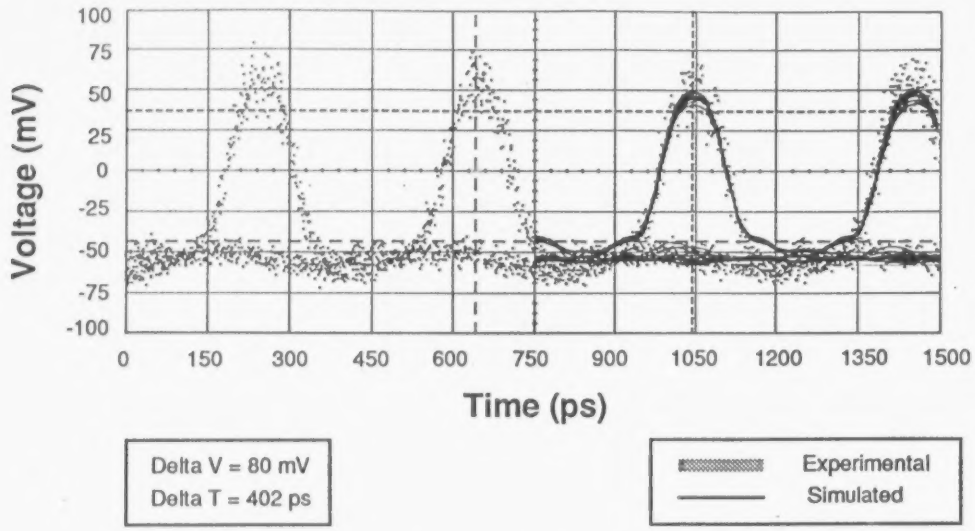

Figure 5.25 : PDM Receiver Eye Diagram

5.4.3 PDM Three Channel Bit Error Rate Measurements

The impact of the presence of the pulsed channels on the data channel was quantitatively assessed by measuring the bit error rate performance of the system in two cases. The situation where the pulsed channel was absent was termed the '1 Channel' case. The condition was termed '3 Channel' when the pulsed channel was present since three of the four time slots of the composite signal were filled. Figure 5.26 shows the bit error rate as a function of received optical power for both the 1 and 3 channel cases.

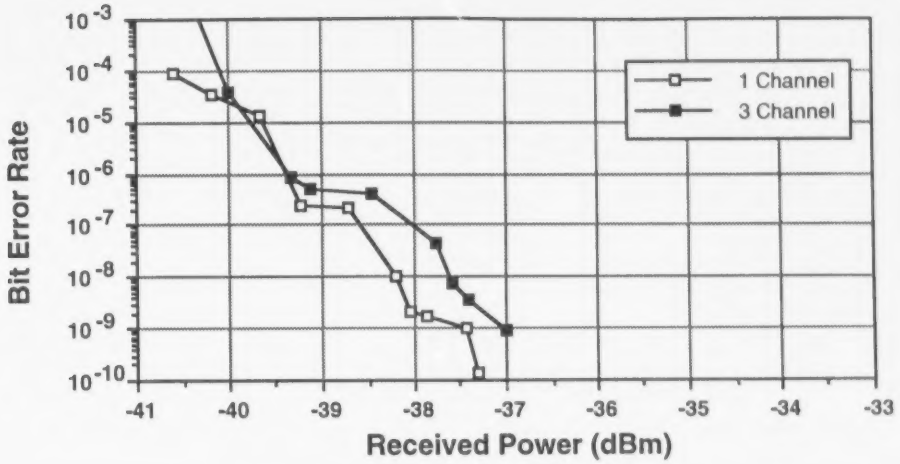

Figure 5.26 : PDM 1 and 3 Channel Receiver Sensitivity

The received power in the figure was referenced to the input of the EDFA in the receiver for convenience. As figure 5.17 shows, there was less than a 0.5 dB receiver sensitivity penalty due to the presence of the pulsed channel. In the 1 and 3 channel cases, the receiver sensitivities at a 10^{-9} bit error rate level were -37.5 dBm and -37.0 dBm respectively. This 0.5 dB penalty is due to polarization crosstalk arising from the finite polarization extinction characteristic of the polarization multiplexers.

5.4.4 Polarization Multiplexing Transmission Experiments

Only one EDFA was required to obtain 10^{-9} BER performance in the back-to-back polarization multiplexing link. Since two additional optical amplifiers were available, transmission experiments over optical fiber were conducted. The transmission experiments were carried out for three reasons. First, a quantitative measure of the receiver sensitivity penalty of polarization multiplexing/demultiplexing as a function of distance was desired. As well, it was important to investigate possible polarization dispersion and polarization stability issues over relatively long lengths of fiber. Finally, an indirect confirmation of the

spectral properties of the transmitted signal was deemed possible through observation of pulse distortion as a function of transmission distance.

5.4.4.1 Transmission Experiments

Several transmission tests were conducted using different fiber lengths. The particular set of distances examined here included fiber lengths from 0 to 100 km in steps of 25 km. Depending on the transmission distance, either 1 or two additional EDFAs were required. Figure 5.27 shows the five trial cases along with the appropriate EDFA configurations to compensate for fiber losses.

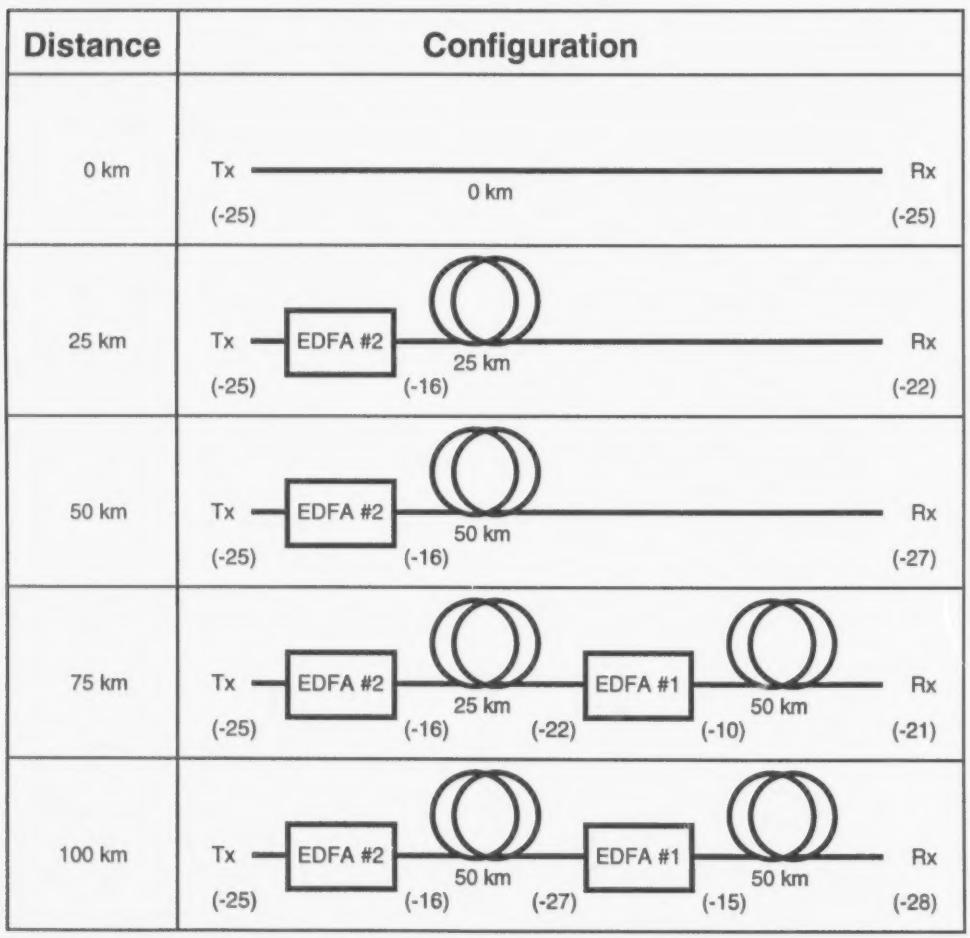

Figure 5.27 : PDM Transmission Configurations

The 25 km sections of fiber were the Corning type fiber, while the 50 km sections were the Northern Telecom fiber. The approximate optical signal power levels of the data channel at the maximum EDFA gain levels are included underneath each configuration. The total optical powers in the pulsed channels plus the modulated channel were about 6 dB higher than those listed for the modulated channel alone. Details on the EDFA types and operating conditions as well as the optical bandpass filters are included in appendix 5A.

The bit error rate as a function of received power was measured for the 0, 25, 50, 75, and 100 km distance cases. The actual bit error rate curves for each of these distances are included in appendix 5B. Figure 5.28 below summarizes the transmission results by plotting the 10^{-9} bit error rate receiver sensitivity as a function of transmission distance.

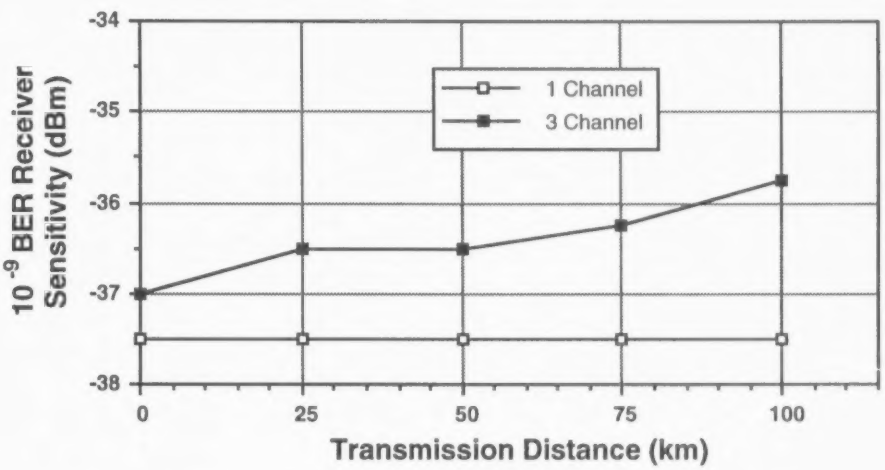

Figure 5.28 : PDM Transmission Receiver Sensitivities

By comparing the one and three channel 10^{-9} bit error rate sensitivities, we can estimate the effective receiver sensitivity penalty due to the polarization multiplexing process as a function of transmission distance. From the figure, we can see that the penalty increases from about 0.5 dB at the 0 km distance to about 1.75 dB at the 100 km distance.

The sensitivity penalty is caused by optical crosstalk from the pulsed channel into the modulated channel. The dependence of the penalty on distance indicates that polarized light travelling over long distances is either somewhat dispersed or unstable. In this context, polarization 'dispersion' is intended to mean polarization scattering from the pulsed channel into the orthogonal polarization of the data channel only as a result of transmission over the fiber. Polarization instability refers to polarization drift over time observed at the receiver. The instability is then translated into crosstalk after polarization demultiplexing.

5.4.4.2 Polarization Drift

While it was not possible to isolate strictly the relative contributions of the two PDM penalty sources, an attempt was made to observe the polarization drift over time for the 100 km transmission case. The polarization crosstalk was first minimized by adjusting the polarization controller at the receiver. Figure 5.29 shows the optical crosstalk as a function of time over a 40 minute interval.

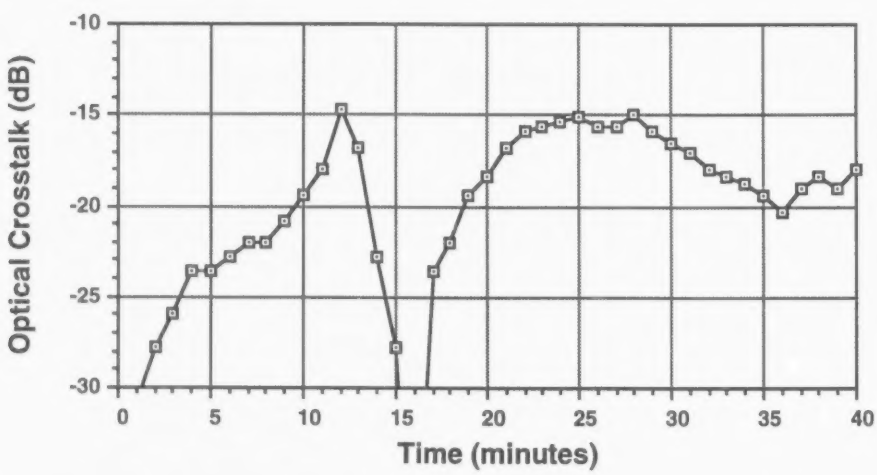

Figure 5.29 : PDM 100 km Transmission Optical Crosstalk

Figure 5.29 shows that over the 40 minute time interval, optical crosstalk varied from less than -30 dB to as high as -15 dB at some times. It was possible to obtain the original BER curve again by re-optimizing the position of the polarization controller. Thus, the absolute polarization orientation of the optical signal at the receiver wanders as a function of time after transmission through a relatively long distance of fiber. This time dependent polarization drifting penalty could conceivably be avoided through the introduction of a polarization 'tracking' feedback loop involving the polarization controller.

5.4.4.3 Signal Spectral Properties Revisited

From analysis of the inherent spectral linewidth of the source in Section 4.3.2 coupled with an investigation of the switch and modulator chirp in Section 4.4.2.4, it was concluded that the overall spectral width of the transmitted signal would be primarily information limited at a 10 Gb/s transmission rate. If this is indeed the case, then the time domain dispersion of 10 Gb/s type pulses in the experimental system should be determined mainly by the information sidebands imposed on the optical carrier. In chapter 3, the impact of dispersion on a 10 Gb/s eye was investigated for the case where the spectral width of the transmitted signal was determined exclusively by the modulated signal. By comparing the simulated and experimental pulse shapes as a function of transmission distance, it should be possible to confirm qualitatively the information limited spectral property of the transmitted signal. Note that the dispersion simulations examined in chapter 3 were only applicable for a full four channel OTDM system. Therefore, the dispersion simulation was modified to mimic the experimental system of figure 5.21. This included adding $2V_{\pi}$ switching for the first switch in the transmitter and including the frequency responses of both the photodetector and the SHF90P amplifier.

In addition to the BER curves measured during the 0-100 km polarization multiplexing transmission experiments, the actual eye diagrams for the data channel were

observed and recorded as a function of distance. Figures 5.30a to 5.30e show the 10 Gb/s type modulated channel eye diagrams obtained using the sampling scope for the five distances. The simulated eye diagrams are overlaid for comparison purposes.

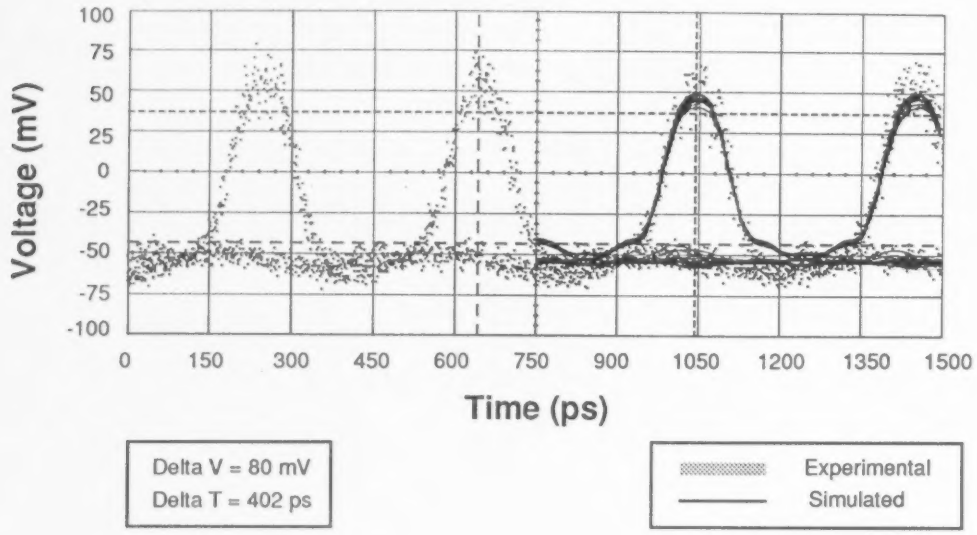

Figure 5.30a : Received Pulse Shape - 0 km

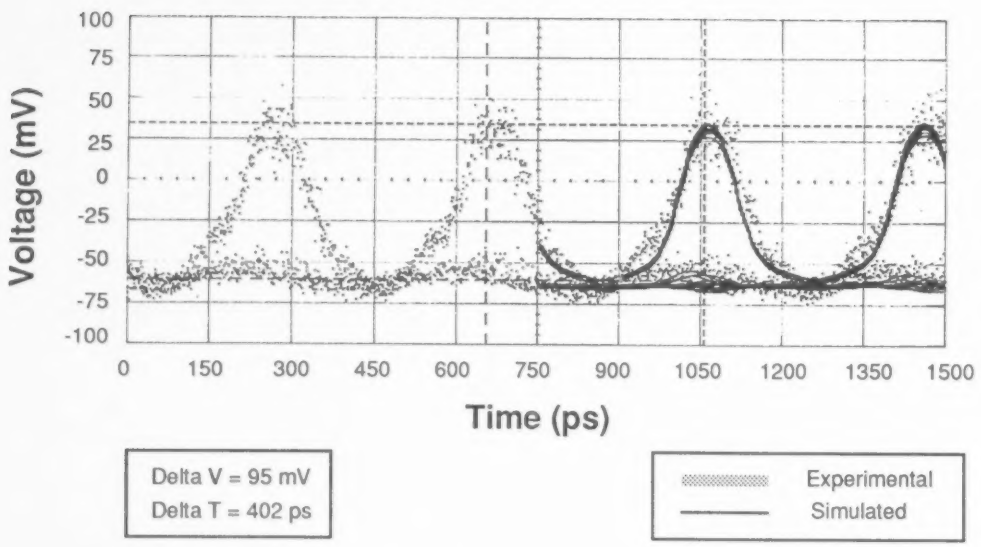

Figure 5.30b : Received Pulse Shape - 25 km

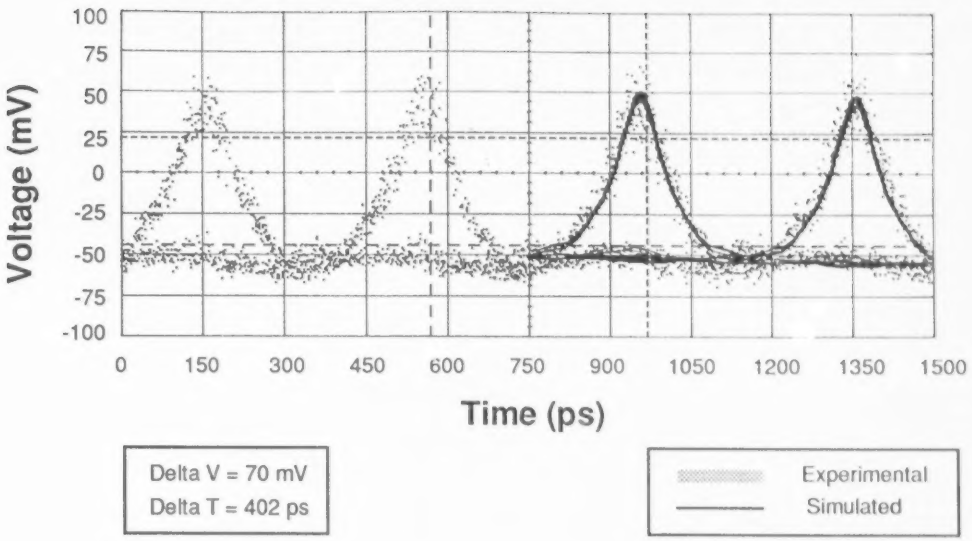

Figure 5.30c : Received Pulse Shape - 50 km

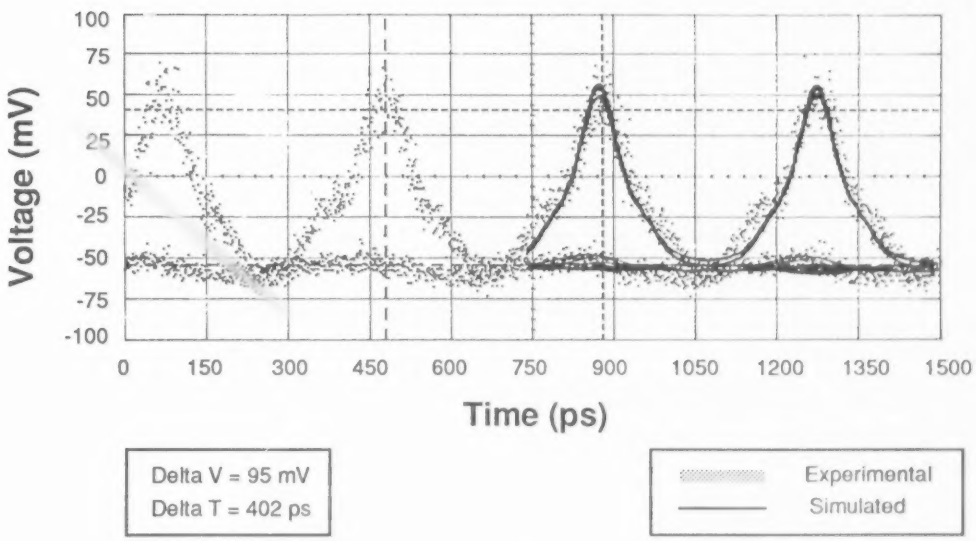

Figure 5.30d : Received Pulse Shape - 75 km

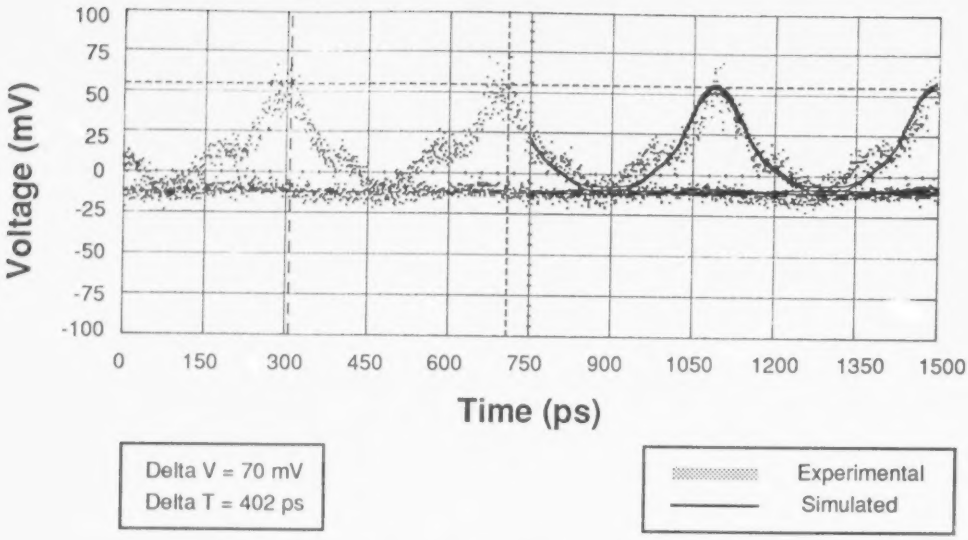

Figure 5.30e : Received Pulse Shape - 100 km

The simulations were conducted using a standard dispersion factor of 17 ps/(km nm). Relatively close agreement is found comparing the experimental pulse shape measurements against the simulation results. In effect, this agreement confirms that the spectrum of the transmitted pulse patterns created by the OTDM switching arrangement in conjunction with the Fujitsu optical source is primarily information limited.

5.5 Summary

The experimental results obtained using the optical time-division multiplexing technique have been examined in Chapter 5. The performance of a two channel OTDM system was discussed first. The block diagrams of the transmitter and receiver were presented along with the waveforms measured at selected points in the system. The computer simulated waveforms agreed well with the experimental results in most cases which indicated qualitatively that the computer model was accurate. The bit error rate performance of the two channel system was presented, and the receiver sensitivity penalty associated with 2 channel OTDM was determined to be approximately 3 dB.

Next, the operation of the three channel OTDM system was discussed to demonstrate multiplexing of immediately adjacent channels. Again, the transmitter and receiver configurations were explained, and the waveform shapes at various points in the system were analyzed. The bit error rate performance of the three channel system indicated a 6 dB receiver sensitivity penalty was associated with adjacent channel multiplexing using the OTDM technique. Both the three channel multiplexed waveform and the bit error rate were observed to fluctuate due to the coherency problems associated with multiplexing adjacent pulses.

Finally, the polarization division multiplexing (PDM) experiments were discussed. The transmitter and receiver configurations were presented, along with the observed waveforms. The bit error rate performance of the system was analyzed, and it was determined that polarization multiplexing resulted in a relatively small 0.5 dB receiver sensitivity penalty for the case where the transmitter and receiver were placed back to back. The penalty associated with PDM was found to be much smaller than that for OTDM due to the virtual elimination of the coherence problem through use of orthogonally polarized channels. Transmission experiments of up to 100 km were possible using the polarization multiplexing technique. The bit error rate performance of the system was presented, and the PDM receiver sensitivity penalty was observed to increase as a function of distance. Polarization drift as a function of time over 100 km of fiber was briefly addressed. Last, the information limited spectral property of the pseudo-10 Gb/s signal was confirmed qualitatively by examining the theoretical and experimental pulse distortion effects caused by fiber dispersion.

Having completed the presentation of the experimental results for the optical time-division multiplexing and polarization multiplexing techniques, we move on to conclude this work with Chapter 6.

6.0 Conclusion

In this thesis, we have described the simulation and experimental studies investigating the performance of an optical time-division multiplexing (OTDM) system. First, we reviewed several of the conventional electro-optic switch structures and provided theoretical background on those devices including switching voltage, bandwidth and chirp properties. It was determined that the Mach-Zehnder interferometer modulator and balanced bridge switch devices were best suited for an integrated OTDM system.

A BOSS computer model of the OTDM system was examined next. The computer model was modular and flexible, and allowed different switching configurations to be built up quickly. The model facilitated analysis of the impact of many system parameters on the composite output signal. Specifically, it was found that switch extinction ratios should exceed 25 dB for negligible eye closure. As well, in the fiber dispersion simulations, we found that after transmission over 60 km of fiber, the eye opening was reduced by 50 percent. Finally, we found that using the 2 V_π switching technique, a 10 Gb/s signal could be generated using 2.5 Gb/s data signals and narrowband 2.5 GHz tones. This technique circumvents the electronic bottleneck which limits high speed electronic systems.

We then moved on to describe the individual components of the experimental OTDM system set up at TR Labs. It was determined that both the spectral properties of the optical source and the chirping characteristics of the switches would not significantly broaden the transmitted spectrum beyond the 10 Gb/s information bandwidth. Essentially, every component from the transmitter to the receiver was characterized and its impact on overall system performance was considered. A brief analysis of the several sources of noise and their relative significance in the OTDM system was also conducted. It was determined that the thermal noise was dominant, and that the signal-spontaneous beat-noise of the optical amplifier was a secondary factor.

In Chapter 5 we presented the first experimental results for an OTDM system using a continuous wave laser source. Two configurations of the experimental system were examined. The '2 Channel' OTDM system multiplexed two 2.5 Gb/s optical digital streams positioned 2 bit times apart. The '3 Channel' system multiplexed three adjacent 2.5 Gb/s channels. The waveforms at various points in the systems were examined and it was found that the computer simulated waveforms agreed well with the experimental results. This agreement qualitatively confirmed the accuracy of the model. Bit error rate measurements were also conducted on the two systems. It was found that the intersymbol interference and coherence effects associated with active optical multiplexing degraded the receiver sensitivity of the system by 3 dB for '2 Channel' OTDM and 6-7 dB for '3-Channel' OTDM.

As shown in the simulations, the experimental OTDM system confirmed that we could generate a pseudo-10 Gb/s optical signal using 2.5 Gb/s data signals and narrowband 2.5 GHz drive electronics. OTDM allows us to avoid the frequency limitations of electronic components through optical multiplexing operations. In addition, we confirmed that the spectral width of the transmitted signal was limited by the imposed information sidebands. The spectral broadening associated with high speed direct modulation of the laser was avoided, and thus the pulse spreading impacts of fiber dispersion were limited.

Finally, the polarization multiplexing (PDM) experiments proved to be highly successful. The 0.5 dB receiver sensitivity penalty associated with 3 channel PDM was found to be substantially less than that for the 3 channel OTDM system since the coherency problem was virtually eliminated through polarization multiplexing. In addition, since the insertion losses of the polarization multiplexing and demultiplexing devices were small, it was possible to perform transmission experiments over distances of up to 100 km of optical fiber. We found that the two polarizations remained essentially orthogonal at

transmission distances of up to 100 km. The receiver sensitivity penalty due to polarization drifting could be eliminated through a polarization tracking feedback control loop. From the studies conducted here, polarization multiplexing looks promising as a technique for increasing fiber optic system throughput. Polarization division multiplexing has the potential to double system throughput if orthogonal polarizations are fully utilized.

6.1 System Improvements

Through this thesis work, we have provided a foundation for OTDM and PDM research at TR Labs. There are many opportunities for improvement of both the computer model and the experimental system.

The BOSS computer model could be enhanced in a number of ways. First, optical insertion losses for both the switching elements and fiber could be added. Second, the inclusion of optical amplifier and noise models, and bit error rate measurement capabilities would greatly increase the usefulness of this tool. Third, it may be helpful to base the switching characteristics of the devices on their physical structures. Currently, the switching elements are modelled by simple mathematical formulas. This would allow one to investigate the impact of the physical parameters such as device length and waveguide and electrode structures on both the single switch and the OTDM system as a whole. Fourth, it would likely be worthwhile to model other types of switching devices such as directional couplers and digital switches. Recall that the current model includes only the balanced bridge interferometer style switch. And finally, enhancing the model to handle optical sources with non-zero spectral widths may increase the flexibility of the model through more accurate dispersion modelling.

The experimental system may also benefit from improvements in several areas. First, optimization of the receiver would improve sensitivity. In the system examined here, the bit error rate test set made the decisions. The addition of an optimal filter and an

external decision-making flip-flop prior to the test set would likely increase sensitivity. In addition, replacing the 'cheat clock' with true clock recovery at the receiver would improve the stability of the system. At the longer transmission distances, clocking drift between the transmitter and receiver degrades the sensitivity.

Second, the coherence problems associated with OTDM could be reduced through the reduction of pulse overlap. This might be accomplished by driving the first switch in the OTDM system with a square-wave or pulsed signal. Alternatively, if near-transform limited optical pulses can be generated externally to the OTDM system, one might consider replacing the cw laser source with a continuously pulsed optical source.

Third, the dispersion impact on the system may be reduced by employing a coding technique such as duobinary encoding. In addition, utilizing the negative chirp properties of a chirp-inducing switch in the transmitter could be used to somewhat compensate for the dispersion in the fiber. Note however, that in general, 2 V_π switching will not be possible during chirped operation of the system.

6.2 Further Work

As stated previously, this thesis has laid some groundwork in the areas of OTDM and PDM and there are many opportunities for further research.

First, the coherency problems associated with multiplexing overlapping pulses in the OTDM system should be explored in further detail. This would involve nailing down the exact source of the problem, including thermal considerations. It may also involve calculating the noise introduced into the OTDM system as a function of coherency in the multiplexed signals. A starting point might be to compare the perfectly coherent and totally incoherent extremity cases.

Second, investigation of an integrated OTDM system may be possible in the future. The distributed system examined in this thesis suffered from high insertion losses and coherency problems. An integrated system would reduce the optical losses in the system. As well, an integrated system may make coherent OTDM possible since the distances traversed on a single substrate are relatively short. Investigation of electrical crosstalk and thermal issues would likely accompany such an endeavor.

Third, the experimental OTDM system examined here used strictly lithium niobate based devices. Problems with lithium niobate include its polarization selectivity and thermal drifting properties. Other optical switching devices such as multiple quantum well structures, polymer and gallium arsenide based switches, and future materials may provide several new avenues for exploration.

Finally, the polarization multiplexing experiments briefly examined in this thesis have raised some interesting issues. For one, it is possible that the polarization transmission properties of straight fiber differ from those of fiber coiled on reels. Investigation of actual polarization dispersion, or in other words, the wavelength delay as a function of polarization, properties of fiber may also be valuable. In addition, the PDM experiments examined here are applicable only to time-interleaved pulse patterns. A relatively simple extension of this work might involve measuring the PDM receiver sensitivity penalty when the pulses of orthogonally polarized channels are directly overlapped in time.

In fact, the polarization of optical signals is just another dimension. It may be possible to use the polarization plane of a signal as a dimension for modulation. This could be a stand alone technique where one would employ, for example, 'polarization-shift-keying'. Or, polarization modulation might be combined with amplitude modulation or even phase modulation as well to produce multi-dimensional modulation schemes.

These are only some of the possibilities that exist for further research. It is also important to remember that the time division and polarization division multiplexing techniques described in this work are only two of the many ways to take advantage of the enormous bandwidths offered by optical systems. As technology and learning progress, it will certainly be interesting to observe exactly how the exploitation of this tremendous resource unfolds.

References

[1] Montgomery, R.K., Ren, F., Abernathy, C. R., Fullowan, T. R., Kopf, R. F., Smith, P. R., Pearton, S. J., Wisk, P., Lothian, J., Nottenburg, R. N. "10 Gbit/s AlGaAs/GaAs HBT lightwave modulator IC", Electronics Letters, Vol. 27, No. 20, September 1991, pp 1827-1829.

[2] Heidemann, Rolf, "Investigations on the Dominant Dispersion Penalties Occurring in Multigigabit Direct Detection Systems", Journal of Lightwave Technology, Vol. 6, No. 11, November 1988, pp 1693-1697.

[3] Petermann, K., Laser Diode Modulation and Noise, Kluwer Academic Publishers, The Netherlands, 1988, pp 118-140.

[4] Djupsjöbacka, Anders. "Time Division Multiplexing Using Optical Switches," IEEE Journal on Selected Areas in Communications," Vol. 6, No. 7, August 1988, pp 1227-1231.

[5] Jaeger, Nick. "Integrated Optics Commutator Switch," University of British Columbia, UBC File No. 91-034, June 1992.

[6] Tamir, Theodor. Guided-Wave Optoelectronics. Springer-Verlag Berlin Heidelberg, Germany, 1988, pp 153-156.

[7] Voges, E., and Neyer, A. "Integrated-Optic Devices on $LiNbO_3$ for Optical Communication," IEEE Journal of Lightwave Technology, Vol. LT-5, No. 9, September 1987, pp 1229-1238.

[8] Zhou, Yi, and Izutsu, Masayuki, and Sueta, Tadasi. "Low-Drive-Power Asymmetric Mach-Zehnder Modulator with Band-Limited Operation." Journal of Lightwave Technology, Vol 9, No. 6, June 1991, pp 750-753.

[9] Marcuse, Dietrich. "Optimal Electrode Design for Integrated Optics Modulators." IEEE Journal of Quantum Electronics, Vol QE-18, No. 3, March 1982, pp 393-398.

[10] Kim, C.M., and Ramaswamy, R.V. "Overlap Integral Factors in Integrated Optic Modulators and Switches." Journal of Lightwave Technology, Vol 7, No. 7, July 1989, pp 1063-1070.

[11] Tamir, Theodor. Guided-Wave Optoelectronics. Springer-Verlag Berlin Heidelberg, Germany, 1988, p 156.

[12] Pedersen, P.R. et al. "A High-Speed 4x4 Ti:$LiNbO_3$ Integrated Optic Switch at 1.5 µm." Journal of Lightwave Technology, Vol. 8 No. 4, April 1990, pp 618-622

[13] Tamir, Theodor. Guided-Wave Optoelectronics. Springer-Verlag Berlin Heidelberg, Germany, 1988, p 157.

[14] Chung, Haeyang, and Chang, William, S.C. "Modelling and Optimization of Traveling-Wave $LiNbO_3$ Interferometric Modulators." IEEE Journal of Quantum Electronics, Vol. 27, No. 3, March 1991, pp 608-617.

[15] Chung, Haeyang, and Chang, William, S.C. "Modelling and Optimization of Traveling-Wave $LiNbO_3$ Interferometric Modulators." IEEE Journal of Quantum Electronics, Vol. 27, No. 3, March 1991, p 611.

[16] Sueta, Tadasi, and Izutsu, Masayuki. "Integrated Optic Devices for Microwave Applications." IEEE Transactions on Microwave Theory and Techniques, Vol. 38, No. 5, May 1990, pp 477-481.

[17] Kawano, K., Kitoh, T., Nozawa, T., and Yanagibashi, M. "New travelling-wave electrode Mach-Zehnder optical modulator with 20 GHz bandwidth and 4.7V driving voltage at 1.52μm wavelength," Electronics Letters, Vol. 25, No. 20, 1989, pp 1382-1383.

[18] Korotky, S.K., Veselka, J.J., "Efficient switching in a 72-Gbit/s Ti:$LiNbO_3$ binary multiplexer/demultiplexer", OFC '90 Technical Digest, January, 1990, p 32.

[19] Dolfi, D.W., Nazarathy, M., "Wide-bandwidth 13-bit Barker code $LiNbO_3$ modulator with low drive voltage", OFC '88 Technical Digest, January, 1988, p 144.

[20] Koyama, F., and Iga, K., "Frequency Chirping in External Modulators", Journal of Lightwave Technology, January, 1988, pp 87-93.

[21] Djupsjobacka, A., "Residual Chirp in Integrated-Optic Modulators", Photonics Technology Letters, January, 1992, pp 41-43.

[22] Cartledge, J. C., and McKay, R. G., "Performance of 10 Gb/s Lightwave Systems Using an Adjustable Chirp Optical Modulator and Linear Equalization", Photonics Technology Letters, December, 1992, pp 1394-1397.

[23] Gnauck, A. H., Korotky, S. K., Veselka, J. J., Nagel, J., Kemmerer, C. T., Minford, W. J., Moser, D. T. "Dispersion Penalty Reduction Using an Optical Modulator with Adjustable Chirp", Photonics Technology Letters, October, 1991, pp 916-918.

[24] Tamir, Theodor. Guided-Wave Optoelectronics. Springer-Verlag Berlin Heidelberg, Germany, 1988, p 175.

[25] Kogelnik, Herwig, and Schmidt, Ronald. "Switched Directional Couplers with Alternating $\Delta\beta$." IEEE Journal of Quantum Electronics, Vol. QE-12, No. 7, July 1976, pp 122-127.

[26] Tamir, Theodor. Guided-Wave Optoelectronics. Springer-Verlag Berlin Heidelberg, Germany, 1988, p 184.

[27] Belanger, Michel, and Yip, Gar Lam. "A Novel Ti:$LiNbO_3$ Ridge Waveguide Linear Mode Confinement Modulator Fabricated By Reactive Ion-Beam

Etching." Journal of Lightwave Technology, Vol. LT-5 No. 9, September 1987, pp 1252-1257.

[28] Sekerka-Bajbus, Michel A., and Yip, Gar Lam, and Goto, Nobuo. "BPM Design Optimization and Experimental Improvement of a Ti:$LiNbO_3$ Ridge Waveguide Linear Mode Confinement Modulator." Journal of Lightwave Technology, Vol. 8 No. 11, November 1990, pp 1742-1749.

[29] Pedersen, P.R., Nightingale, J. L., Kincaid, B. E., Vrhel, J. S., and Becker, R. A. "A High-Speed 4x4 Ti:$LiNbO_3$ Integrated Optic Switch at 1.5μm." Journal of Lightwave Technology, Vol. 8, No.4, April 1990, pp 618-622.

[30] Fujiwara, T., Sato, S., Mori, H., and Fujii, Y. "Suppression of Crosstalk Drift in Ti:$LiNbO_3$ Waveguide Switches." Journal of Lightwave Technology, Vol 6, No. 6, June 1988, pp 909-914.

[31] Yamada, S., and Minakata, M. "DC Drift phenomena in $LiNbO_3$ Optical Waveguide Devices." Japan Journal of Applied Physics, Vol. 20, pp 733-737, 1981.

[32] Haruna, M., and Shimada, J., and Nishihara, H. "Optical Wavelength-Independent and damage-free Polarization controller in $LiNbO_3$ Waveguides." 1st Opto-Electronics Conference Technical Digest (Tokyo, Japan), 1986, #A2-4.

[33] Silberberg, Y., and Perlmutter, P., and Baran, J.E. "Digital Optical Switch." Applied Physics Letters, Issue 51, 19 October, 1987, pp 1230-1232.

[34] Burns, William K. "Voltage-Length Product for Modal Evolution-Type Digital Switches." Journal of Lightwave Technology, Vol 8, No. 6, June 1990, pp 990-997.

[35] Tamir, Theodor. Guided-Wave Optoelectronics. Springer-Verlag Berlin Heidelberg, Germany, 1988, p 168.

[36] Tamir, Theodor. Guided-Wave Optoelectronics. Springer-Verlag Berlin Heidelberg, Germany, 1988, p 167.

[37] Veselka, J.J., Herr, D. A., Murphy, T. O., Buhl, L. L., and Korotky, S. K. "Crosstalk Measurements of Integrated High-Speed Ti:$LiNbO_3$ $\Delta\beta$-Reversal Switching Circuits." Journal of Lightwave Technology, Vol 7, No. 6, June 1989, pp 908-910.

[38] Minford, W.J., Korotky, S.K., and Alferness, R.C. "Low-Loss Ti:$LiNbO_3$ Waveguide Bends at $\lambda = 1.3$ μm." IEEE Journal of Quantum Electronics, Vol QE-18, No. 10, October 1982, pp 1802-1806.

[39] Elrefaie, A. F., Wagner, R. E., Atlas, D. A., and Daut, D. G. "Chromatic Dispersion Limitations in Coherent Lightwave Transmission Systems," Journal of Lightwave Technology, Vol. 5, No. 5, May 1988, pp 704-709.

[40] Petermann, K.. Laser Diode Modulation and Noise. Kluwer Academic Publishers, the Netherlands, 1988, pp 152-162.

[41] Bell Telephone Laboratories. Transmission Systems for Communications (Fifth Edition). Bell Telephone Laboratories, United States, 1982, pp 152-162.

[42] Kikuchi, K and Okoshi, T. "High Resolution Measurement of the Spectrum of Semiconductor Lasers," *Japan Annual Review on Electronics, Comp., Telecommunications, Optical Devices, and Fibers, 1982*, 1982, Ohmsha Ltd., Tokyo and North Holland Publishing Co., Amsterdam, Netherlands, pp 51-54.

[43] Kikuchi, K and Okoshi, T. "High Resolution Measurement of the Spectrum of Semiconductor Lasers," *Japan Annual Review on Electronics, Comp., Telecommunications, Optical Devices, and Fibers, 1982*, 1982, Ohmsha Ltd., Tokyo and North Holland Publishing Co., Amsterdam, Netherlands, pp 55.

[44] Miller, Stewart E., and Kaminow, Ivan P (ed.). Optical Fiber Telecommunications II. Academic Press, Inc., San Diego, CA, 1988, pp 270-271.

[45] Bell Laboratories. "Borosilicate glasses for fiber optical waveguides." Materials Research Bulletin, Pergamon Press Inc., 1973, Vol. 8 (4), pp 469-476.

[46] Way, Winston, I. "Optical Amplifiers For Multichannel Video Transmission and Distribution." 1991 Technical Digest Series Volume 13, July 1991, pp 206-209.

[47] Freeman, James, E. Theory, Design, and Characterization of EDFAs. University of Alberta, Oct. 1991, pp 113-115.

[48] Olsson, N. A. "Lightwave Systems With Optical Amplifiers." Journal of Lightwave Technology, Vol. 7, No. 7, July 1989, pp 1071-1081.

[49] Lathi, B. P. Modern Digital and Analog Communications Systems. Holt, Rinehart and Winston, United States, 1983, pp 153-155.

[50] Siddiqui, A. S., and Zhou, J. "Two-channel optical fiber transmission using polarization division multiplexing." Journal of Optical Communications, Vol. 12, 1991, pp 47-49.

[51] Hill, P. M., Olshansky, R., Burns, W. K. "Optical Polarization Division Multiplexing at 4 Gb/s." Photonics Technology Letters, Vol. 4, No. 5, May 1992, pp 500-502.

[52] Hill, P. M., Olshansky, R., Burns, W. K. "Optical Polarization Division Multiplexing at 8 Gb/s With Novel Clock and Carrier Recovery." European Conference on Optical Communications, Session Tu A5.6, 1992, pp 165-168.

[53] Herard, C., and Lacourt, A. "New Multiplexing Technique Using Polarization of Light." Applied Optics, Vol. 30, 1991, pp 222-231.

[54] Koehler, B. G., and Bowers, J., E. "In-Line Single-Mode Fiber Polarization Controllers at 1.55, 1.30, and 0.63 μm." Applied Optics, Vol. 24, No. 3, February 1985, pp 349-353.

Appendix 3A : BOSS Module Block Diagrams

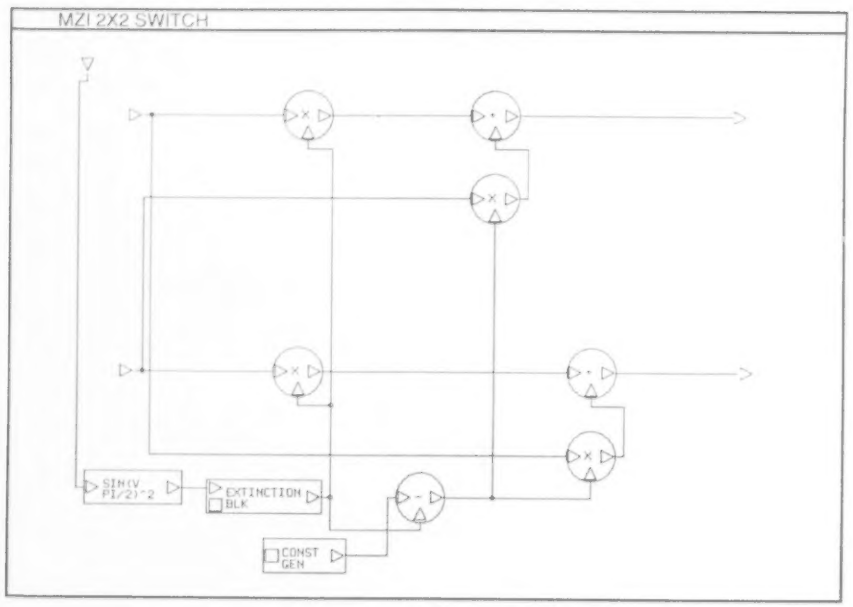

Figure 3A.1 : MZI 2X2 SWITCH Block Diagram

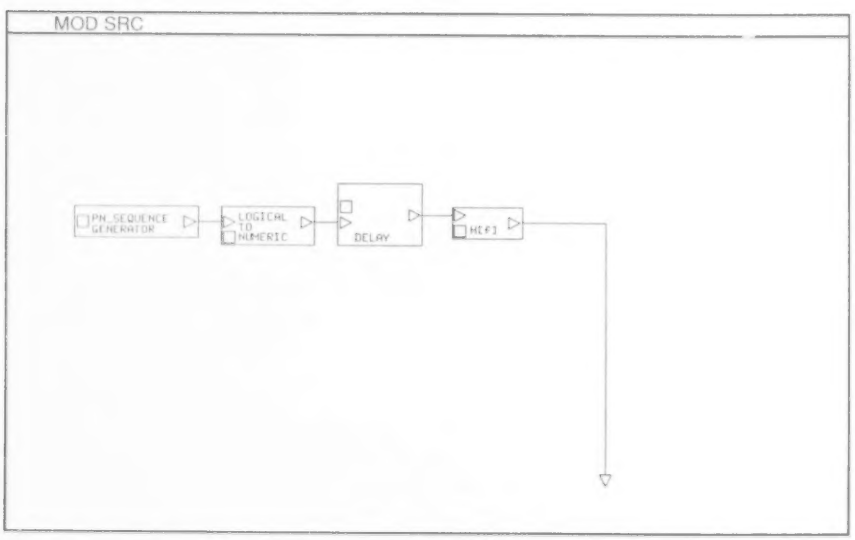

Figure 3A.2 : MOD SRC Block Diagram

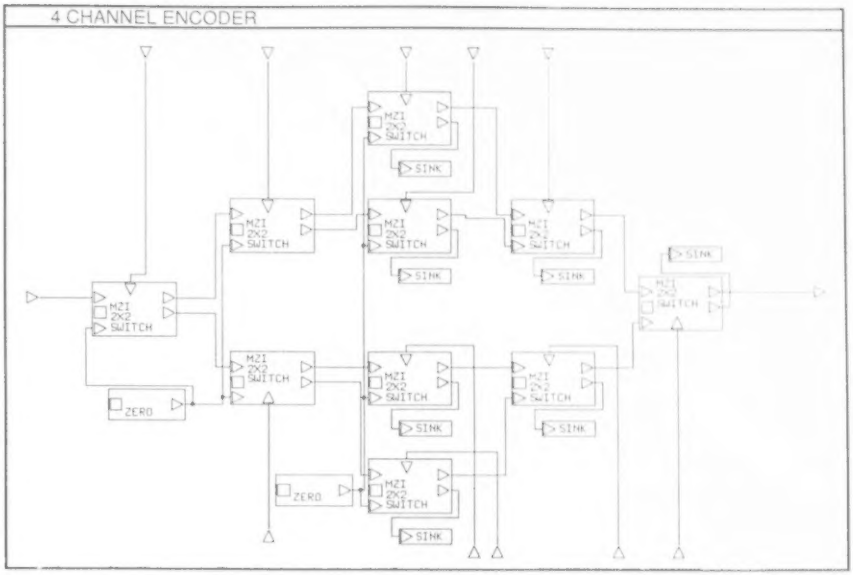

Figure 3A.3 : 4 CHANNEL ENCODER Block Diagram

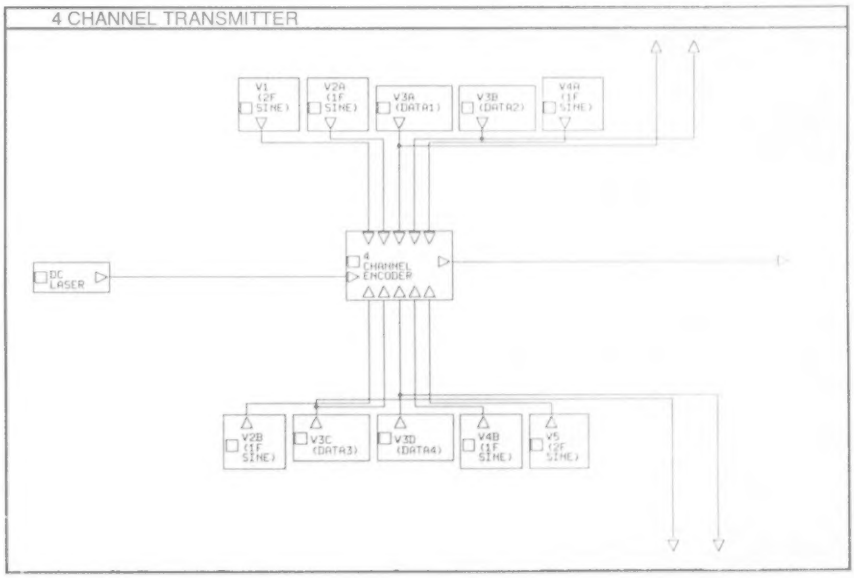

Figure 3A.4 : 4 CHANNEL TRANSMITTER Block Diagram

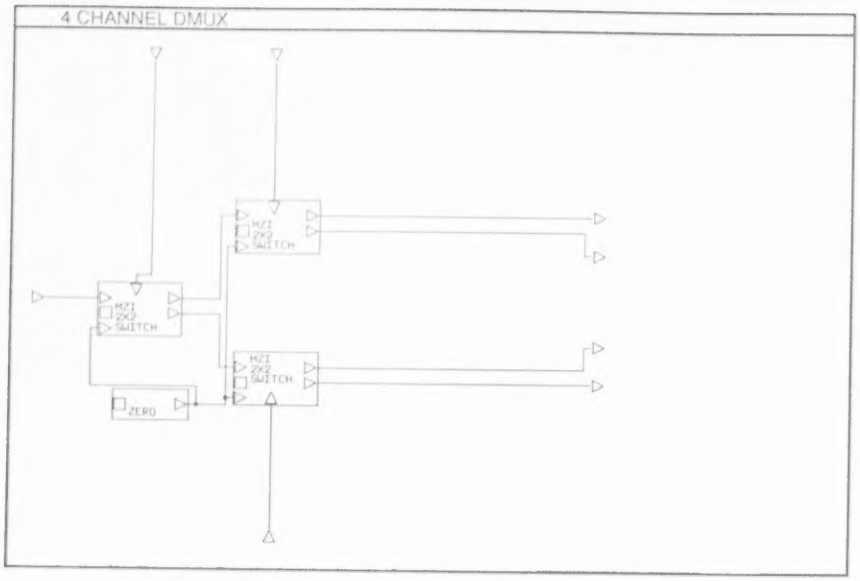

Figure 3A.5 : 4 CHANNEL DMUX Block Diagram

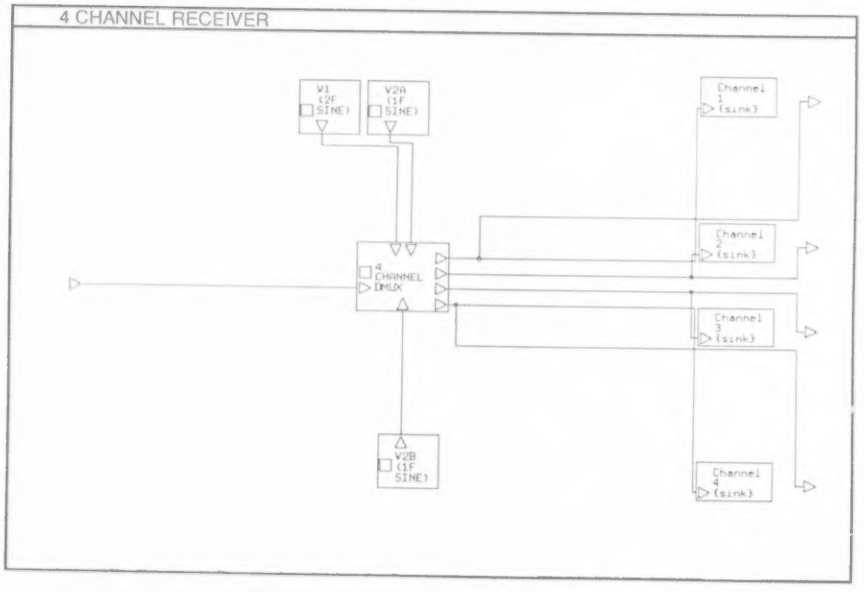

Figure 3A.6 : 4 CHANNEL RECEIVER Block Diagram

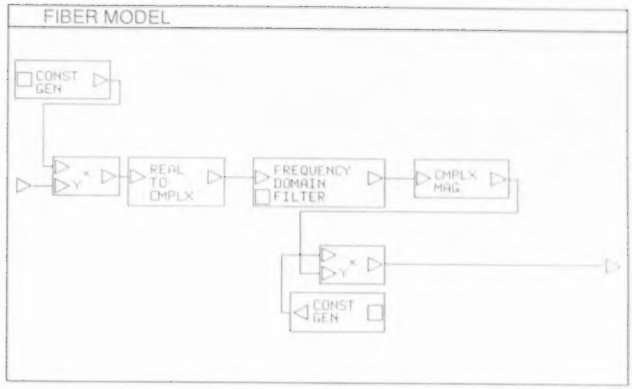

Figure 3A.7 : FIBER MODEL Block Diagram

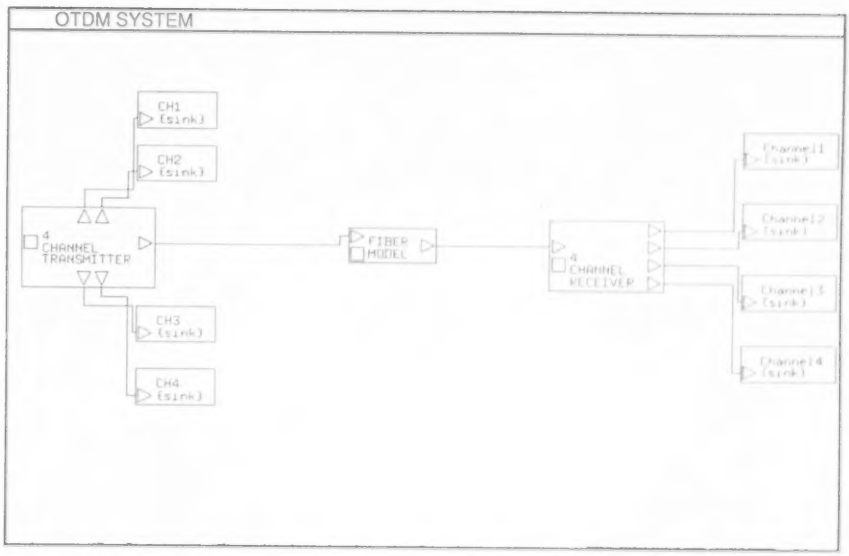

Figure 3A.8 : OTDM SYSTEM Block Diagram

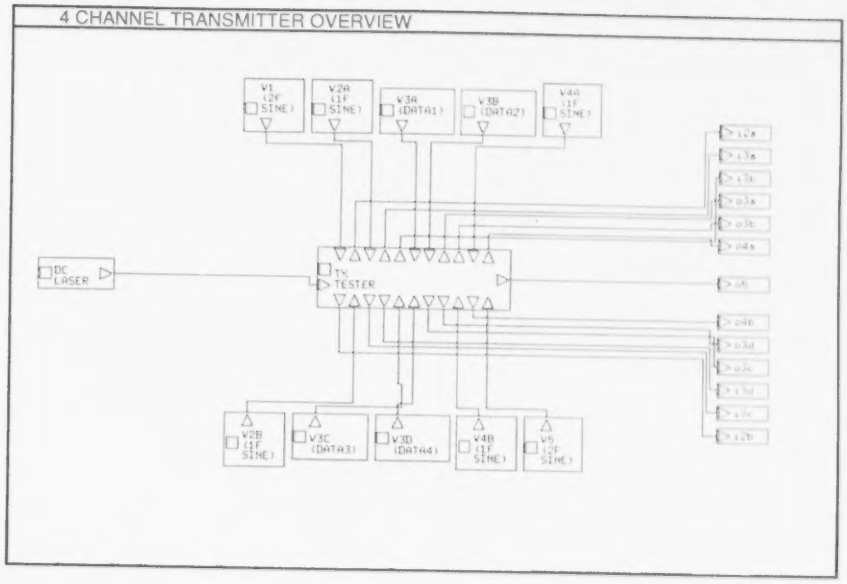

Figure 3A.9 : 4 CHANNEL TRANSMITTER OVERVIEW Block Diagram

Appendix 3B : Listing 3B.1 - Electro-optic Switch Frequency Response Calculation 'C' Code

```
/*
*   Microwave attenuation loss and velocity mismatch
*   data calculation code for an electro-optic switch.
*
*   Programmed by : Ken Benterud
*                   October 1991
*
*
*/

#include <stdio.h>
#include <math.h>
#define PI 3.1415926535
#define SMALL 0.001

#define DT (1.0/320.0E9)
#define NUMFPOINTS 640.0  /* actual #of points is NUMFPOINTS+1 */

#define Clight 3.0E+10     /* speed of light in vacuum in cm/s*/
#define Nm 4.2     /* microwave index */
#define No 2.2     /* optical index   */
#define ALPHAo 1.0 /* in dB/cm        */
#define LENGTH 1.0 /* centimeters     */


/********************** eta_calc ******************
*
*  Routine :  eta_calc
*
*
*/
double eta_calc(freq)
double freq;
{
  return( 2*PI*fabs(freq)*(Nm-No)/Clight );
}


/********************** alpha_calc ****************
*
*  Routine :  alpha_calc
*
*
*/
double alpha_calc(freq)
double freq;
{
  return( log(10.0) * ALPHAo * sqrt(fabs(freq/1E9)) / 10 );
}


/********************** hf_calc ***************
*
*  Routine :  hf_calc
```

```
*
*
*/
double hf_calc(freq)
double freq;
{
  double a,b,c,d,e;

  a= alpha_calc(fabs(freq))*LENGTH/2;
    /*  printf("absfreq= %e  a= %e\n",fabs(freq),a); */
  b= eta_calc(fabs(freq))*LENGTH/2;
    /*  printf("absfreq= %e  b= %e\n",fabs(freq),b);  */

    /*  printf("absfreq= %e  sinh(a)= %e\n",fabs(freq),sinh(a));  */
  d=  pow( (sinh(a)),2.0);
    /*  printf("absfreq= %e  d= %e\n",fabs(freq),d);  */

  c= sqrt (
                      (d + pow( (sin(b)),2.0) )
                      /
                  min,fmax);


  printf("Writing to output file %s\n",datname);
  datfile= fopen(datname,"w");
  fprintf(datfile,"3,%d\n",(int) (rint(NUMFPOINTS+1)) );
  fprintf(datfile,"freq in hertz\n");
  fprintf(datfile,"dB power magnitude\n");
  fprintf(datfile,"phase in degrees\n");

  for (freq=fmin; freq<=(fmax+df/2); freq+=df)
  {
    fprintf(datfile,"%e %e %e\n",rint(1E+10*freq)/1E+10,hf_calc(freq)
  ,phase);

  fclose ( datfile );
}
/* end hf_calc */



/********************* main *****************
*
*  Routine :  main
*
*
*/

main()
{
  hf_print("mwlf2");

}  /* end main */
```

Appendix 3C : Listing 3C.1 - Fiber Dispersion Calculation 'C' Code

```
/*
*   Fiber dispersion
*   data calculation code.
*
*   Programmed by : Ken Benterud
*                   October 1991
*
*/

#include <stdio.h>
#include <math.h>
#define PI 3.1415926535
#define SMALL 0.001

#define DT (1.0/320.0E+9)
#define NUMFPOINTS 1280.0  /* actual #of points is NUMFPOINTS+1 */


/* Global Variables */
double LENGTH; /* fiber length in km */


/********************** phasecalc *****************
*
*  Routine :  phasecalc
*
*
*/
double phasecalc(freq)
double freq;
{
  double wc,c,d,result_degrees;

  wc= 1550E-9; /* carrier wavelength */
  c= 3.0E+8; /* speed of light in m/s */

  d= 0.0170;  /* delay in s/(km m) */

  result_degrees= -wc*wc/c *d*LENGTH *freq*freq * 180;

    /*  printf("absfreq= %e  c= %e\n",fabs(freq),c);  */


  if ( fabs(freq)<1E-6 )
    return(0.0);
  else
    return (result_degrees);
}



/********************** phase_print ****************
```

```
*
*  Routine :  phase_print
*
*
*/
phase_print(datname)
char *datname;
{
  FILE *datfile;
  double freq,phase,attn,fmin,fmfreq)/1E+10,
                                    attn,phasecalc(freq));
  }

  fclose ( datfile );
}
/* end phase_print */


/********************* main *****************
*
*  Routine :  main
*
*
*/

main()
{
  LENGTH=100.0;
  phase_print("fiberfcn100km17");

}  /* end main */
```

Appendix 3D : Derivation of the Power Spectral Density of a Finite Length Pseudo-Random Binary Sequence

Let g[t] be the pulse shape for the sequence. For a rectangular pulse with amplitude A and duration T:

$$g[t] = \begin{cases} A & , 0 \le t \le T \\ 0 & , \text{otherwise} \end{cases} \qquad \text{(B.1)}$$

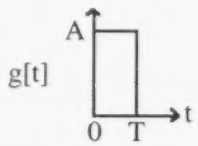

The power spectral density of g[t] is then given by G[f] as:

$$|G[f]|^2 = (AT)^2 \left(\frac{\sin \pi fT}{\pi fT}\right)^2 \qquad \text{(B.2)}$$

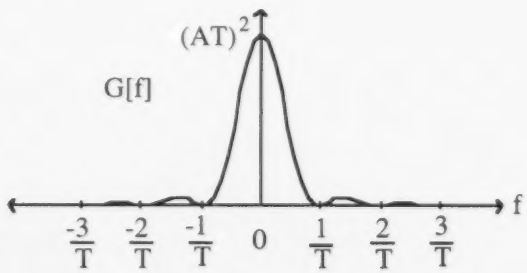

For a truly random sequence, the shape of the power spectral density of a sequence is the same as that for a single pulse since all pulses are truly independent. However, this is not the case for a pseudo-random sequence where a particular bit pattern is repeated. Repetition of a bit pattern introduces correlation into the sequence, and this dependence will show up in the spectral content of the signal.

If N is the length of the psuedo-random binary sequence with zero average value, the autocorrelation function of the sequence $\phi_i[k]$ is given by the expected value of the product of an information symbol I_n with all other symbols I_{n+k}:

$$\phi_i[k] = E[I_n I_{n+k}] = \begin{cases} 1 & , k=0,N,2N,3N \ldots \\ 0 & , \text{otherwise} \end{cases} \tag{B.3}$$

The Fourier transform of this sequence is :

$$S[f] = \sum_{k=-\infty}^{\infty} e^{-j2\pi fTk}\phi_i[k] = \frac{1}{TN}\sum_{k=-\infty}^{\infty} \delta\left(f - \frac{k}{TN}\right) \tag{B.4}$$

Finally, the power spectral density of the pseudo-random sequence using g[t] as the pulse shape is determined by :

$$X[f] = \frac{1}{T}|G[f]|^2 S[f]$$

or,

$$X[f] = \frac{A^2}{N}\left(\frac{\sin \pi fT}{\pi fT}\right)^2 \sum_{k=-\infty}^{\infty} \delta\left(f - \frac{k}{TN}\right) \tag{B.5}$$

From equation B.5, we can see that the power spectral density of a pseudo-random binary sequence of length N retains the envelope of the pulse shape spectrum, and is composed of discrete spectral lines with frequency spacing 1/TN. In the limit as the sequence length N approaches infinity, the result in (B.5) approaches the power spectral density of a truly random sequence :

$$X[f] = \frac{1}{T}|G[f]|^2$$

In this case, S[f] = 1 and the power spectral density is continuous.

APPENDIX 4A : The Polarization Controller

The lithium niobate modulator/multiplexer and demultiplexer electro-optic elements are sensitive to the polarization of the input light. For lithium niobate, the electro-optic effect is approximately 3 times larger for the TE mode compared to the TM mode. Therefore, to maximize the electro-optic effect, the polarization of the input light should be as linear as possible, and oriented so that the TE mode is acted upon by the electric field.

To achieve a linear polarization in the desired direction for the optical switches and modulator, in-line single-mode fiber polarization controllers were constructed according to directions by B.G. Koehler and J.E. Bowers [54]. The controllers consist simply of several fairly small loops of fiber fastened to a rotatable plate. The principle of operation is that the polarization of the light is altered by inducing birefringence in the fiber. Birefringence is accomplished by rotating the plate with the loops to place stress on the fiber.

By experiment, it was found that a quarter wave plate could be approximated by two 2.3 cm loops, and a half wave plate by three 2.3 cm loops. The idea is that the quarter wave plate can be used to obtain some linear polarization. Then the half-wave plate can be used to rotate the orientation of the linearly polarized light.

In practice, in fact, it was found that by using these approximate quarter and half wave plates, linear polarizations in any direction could be achieved. The degree of polarization, or the ratio of the power in the maximum power polarization relative to the power in the orthogonal direction, was typically greater than 100 to 1. Due to the relatively small radius bends, some light is scattered out of the fiber loops. The device was measured to have an insertion loss of about 1 dB.

APPENDIX 4B : Modulator and Switch Test Data

The dc and rf operating characteristics of the optical modulator and switches were confirmed experimentally. The setup used to perform the dc measurements included the Fujitsu DFB laser as the optical source, an optical power meter, and variable dc bias voltage supplies.

The rf measurements were performed using the swept frequency technique described in section 4.4.2.3 of this work. Briefly, a network analyzer was used to measure the swept frequency response of the electro-optic device in conjunction with the BT&D photodetector. The response of the detector was determined by using amplified spontaneous emission from an erbium-doped fiber amplifier as described in section 4.6.2.3. The response of the electro-optic device was obtained by subtracting the response of the detector from the response of the concatenated setup.

The test data sheets for the United Technologies Photonics (UTP) modulator and the five ETEK Dynamics (ETEK) 2 by 2 switches are contained in the following pages.

TR LABS

Test Data Sheet

Device Under Test :	United Technologies Photonics 1x2 Modulator	
Part Number :	APE-YBBM-1.5-12.T-02	
Serial Number :	266	
Device Length :	8.5 cm	
Fiber Lengths :	Input	1.60 m
	Output 1	2.09 m
	Output 2	1.77 m

Performance Data

Insertion Loss Output 1 :	4.5 dB
Insertion Loss Output 2 :	5.0 dB
Extinction Ratio Output 1 :	23.5 dB
Extinction Ratio Output 2 :	32.0 dB
DC V_π Switching Voltage :	5.8 Volts
RF Switching Power (1 GHz) :	+27 0 dBm into 50 ohms
RF Frequency Response :	See Plot Below

Test Conditions

Optical Source :	Fujitsu DFB 4 mW max.
Operation Wavelength :	1551 nm
Detector used in Swept Frequency Response Test :	BT&D PDC4310-30 (20 GHz BW)

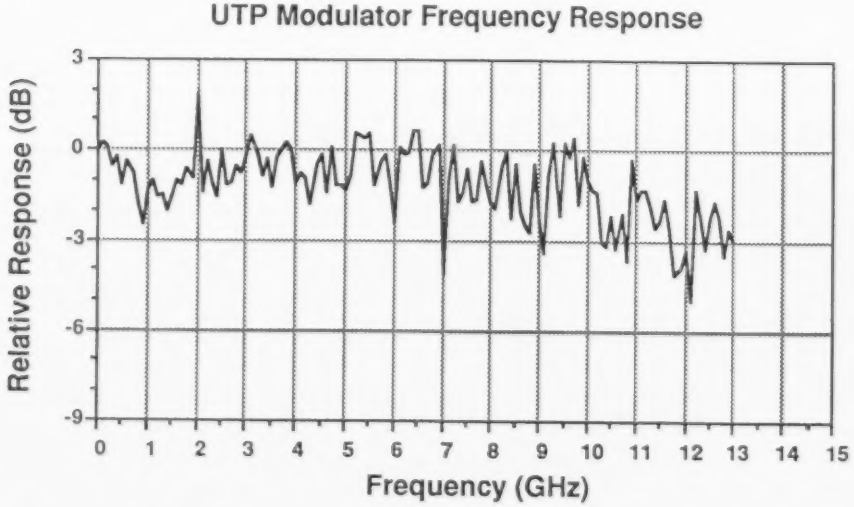

Performed By : _____ Date : _____

TR LABS

Test Data Sheet

Device Under Test :	ETEK 2x2 Electro-Optic Switch (ETEK #1)			
Part Number :	EOSW-0202-1550			
Serial Number :	92061901			
Device Length :	8.5 cm			
Fiber Lengths :	Input 1 (#1)	1.35 m	Output 1 (#3)	1.48 m
	Input 2 (#2)	1.37 m	Output 2 (#4)	1.32 m

Performance Data

Insertion Loss (I1 to O3) :	7.6 dB (Incl. 1.8 dB loss from 2 core mismatches)
Insertion Loss (I1 to O4) :	7.2 dB
Insertion Loss (I2 to O3) :	7.3 dB
Insertion Loss (I2 to O4) :	7.3 dB
Extinction Ratio (I1 to O3) :	40 dB
Extinction Ratio (I1 to O4) :	35 dB
Extinction Ratio (I2 to O3) :	25 dB
Extinction Ratio (I2 to O4) :	22 dB
V_1 Tuning Voltage :	11.5 Volts
V_3 Tuning Voltage :	7.5 Volts
DC V_π (V_2)Switching Voltage :	5.3 Volts
RF Switching Power (1 GHz) :	+23 dBm into 50 ohms
RF Frequency Response :	See Plot Below

Test Conditions

Optical Source :	Fujitsu DFB 4 mW max.
Operation Wavelength :	1551 nm
Detector used in Swept Frequency Response Test :	BT&D PDC4310-30 (20 GHz BW)

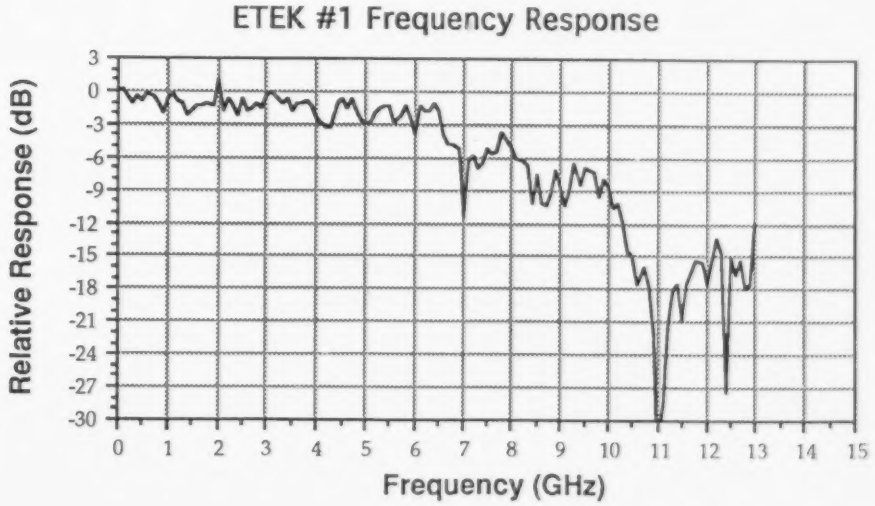

Performed By : _____ Date : _____

TR LABS

Test Data Sheet

Device Under Test :	ETEK 2x2 Electro-Optic Switch (ETEK #2)			
Part Number :	EOSW-0202-1550			
Serial Number :	92101601			
Device Length :	8.5 cm			
Fiber Lengths :	Input 1 (#1)	1.22 m	Output 1 (#3)	1.24 m
	Input 2 (#2)	1.18 m	Output 2 (#4)	1.12 m

Performance Data

Insertion Loss (I1 to O3) :	7.1 dB (Incl. 1.8 dB loss from 2 core mismatches)
Insertion Loss (I1 to O4) :	5.6 dB
Insertion Loss (I2 to O3) :	8.1 dB
Insertion Loss (I2 to O4) :	7.6 dB
Extinction Ratio (I1 to O3) :	32 dB
Extinction Ratio (I1 to O4) :	33 dB
Extinction Ratio (I2 to O3) :	24 dB
Extinction Ratio (I2 to O4) :	22 dB
V_1 Tuning Voltage :	12.5 Volts
V_3 Tuning Voltage :	11.3 Volts
DC V_π (V_2)Switching Voltage :	4.5 Volts
RF Switching Power (1 GHz) :	+21.5 dBm into 50 ohms
RF Frequency Response :	See Plot Below

Test Conditions

Optical Source :	Fujitsu DFB 4 mW max.
Operation Wavelength :	1551 nm
Detector used in Swept Frequency Response Test :	BT&D PDC4310-30 (20 GHz BW)

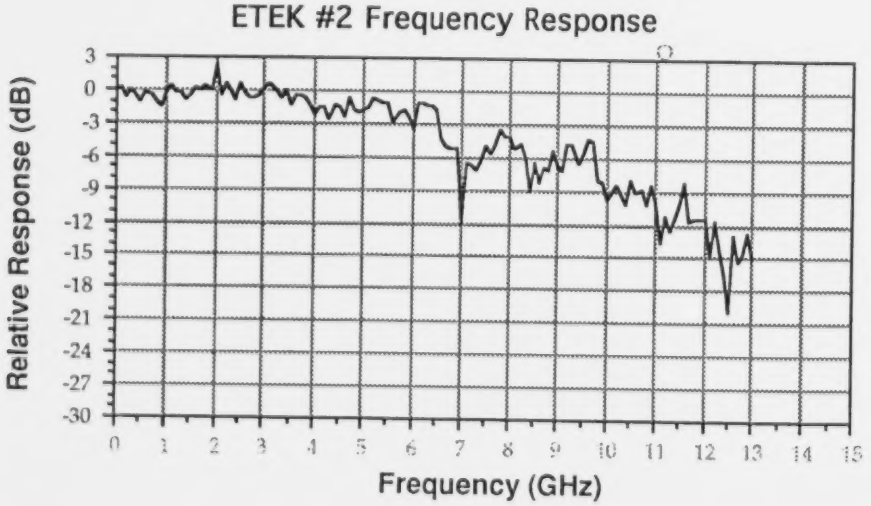

Performed By : _____ Date : _____

TR LABS

Test Data Sheet

Device Under Test :	ETEK 2x2 Electro-Optic Switch (ETEK #3)			
Part Number :	EOSW-0202-1550			
Serial Number :	92111001			
Device Length :	8.5 cm			
Fiber Lengths :	Input 1 (#1)	1.22 m	Output 1 (#3)	1.10 m
	Input 2 (#2)	1.21 m	Output 2 (#4)	1.10 m

Performance Data

Insertion Loss (I1 to O3) :	7.1 dB (Incl. 1.8 dB loss from 2 core mismatches)
Insertion Loss (I1 to O4) :	6.7 dB
Insertion Loss (I2 to O3) :	7.6 dB
Insertion Loss (I2 to O4) :	6.9 dB
Extinction Ratio (I1 to O3) :	26 dB
Extinction Ratio (I1 to O4) :	37 dB
Extinction Ratio (I2 to O3) :	23 dB
Extinction Ratio (I2 to O4) :	27 dB
V_1 Tuning Voltage :	9.9 Volts
V_3 Tuning Voltage :	10.0 Volts
DC V_π (V_2)Switching Voltage :	4.3 Volts
RF Switching Power (1 GHz) :	+21.5 dBm into 50 ohms
RF Frequency Response :	See Plot Below

Test Conditions

Optical Source :	Fujitsu DFB 4 mW max.
Operation Wavelength :	1551 nm
Detector used in Swept Frequency Response Test :	BT&D PDC4310-30 (20 GHz BW)

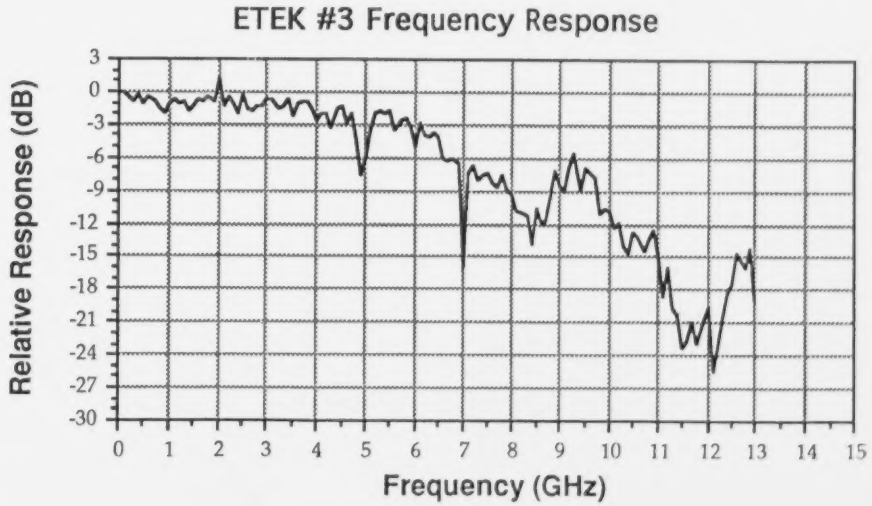

Performed By : _____ Date : _____

TR LABS

Test Data Sheet

Device Under Test :	ETEK 2x2 Electro-Optic Switch (ETEK #4)			
Part Number :	EOSW-0202-1550			
Serial Number :	92122801			
Device Length :	8.5 cm			
Fiber Lengths :	Input 1 (#1)	1.19 m	Output 1 (#3)	1.12 m
	Input 2 (#2)	1.20 m	Output 2 (#4)	1.12 m

Performance Data

Insertion Loss (I1 to O3) :	8.3 dB (Incl. 1.8 dB loss from 2 core mismatches)
Insertion Loss (I1 to O4) :	7.6 dB
Insertion Loss (I2 to O3) :	7.9 dB
Insertion Loss (I2 to O4) :	8.1 dB
Extinction Ratio (I1 to O3) :	27 dB
Extinction Ratio (I1 to O4) :	29 dB
Extinction Ratio (I2 to O3) :	36 dB
Extinction Ratio (I2 to O4) :	23 dB
V_1 Tuning Voltage :	10.6 Volts
V_3 Tuning Voltage :	0.53 Volts
DC V_π (V_2)Switching Voltage :	4.4 Volts
RF Switching Power (1 GHz) :	+22.5 dBm into 50 ohms
RF Frequency Response :	See Plot Below

Test Conditions

Optical Source :	Fujitsu DFB 4 mW max.
Operation Wavelength :	1551 nm
Detector used in Swept Frequency Response Test :	BT&D PDC4310-30 (20 GHz BW)

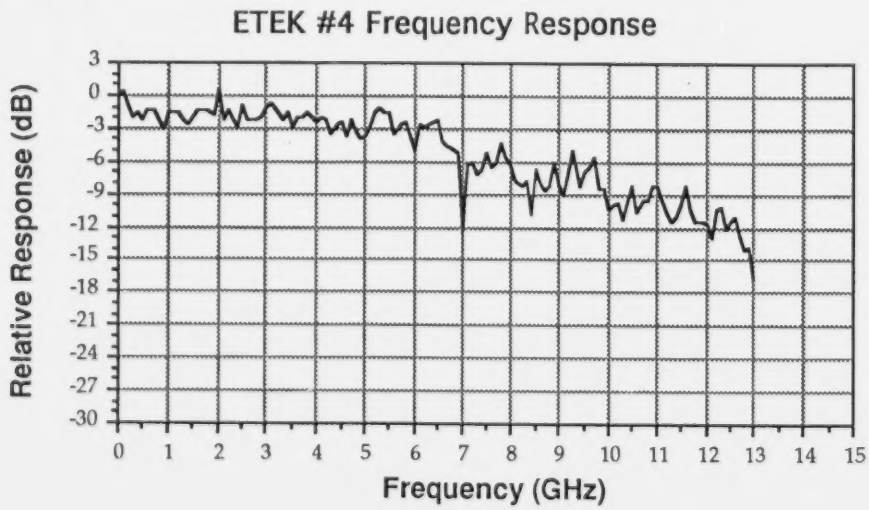

Performed By : _____ Date : _____

TR LABS

Test Data Sheet

Device Under Test :	ETEK 2x2 Electro-Optic Switch (ETEK #5)			
Part Number :	EOSW-0202-1550			
Serial Number :	92122101			
Device Length :	8.5 cm			
Fiber Lengths :	Input 1 (#1)	1.26 m	Output 1 (#3)	1.20 m
	Input 2 (#2)	1.22 m	Output 2 (#4)	1.20 m

Performance Data

Insertion Loss (I1 to O3) :	7.7 dB (Incl. 1.8 dB loss from 2 core mismatches)
Insertion Loss (I1 to O4) :	9.6 dB
Insertion Loss (I2 to O3) :	6.8 dB
Insertion Loss (I2 to O4) :	7.8 dB
Extinction Ratio (I1 to O3) :	26 dB
Extinction Ratio (I1 to O4) :	32 dB
Extinction Ratio (I2 to O3) :	31 dB
Extinction Ratio (I2 to O4) :	27 dB
V_1 Tuning Voltage :	4.5 Volts
V_3 Tuning Voltage :	8.3 Volts
DC V_π (V_2)Switching Voltage :	9.7 Volts
RF Switching Power (1 GHz) :	+22.0 dBm into 50 ohms
RF Frequency Response :	See Plot Below

Test Conditions

Optical Source :	Fujitsu DFB 4 mW max.
Operation Wavelength :	1551 nm
Detector used in Swept Frequency Response Test :	BT&D PDC4310-30 (20 GHz BW)

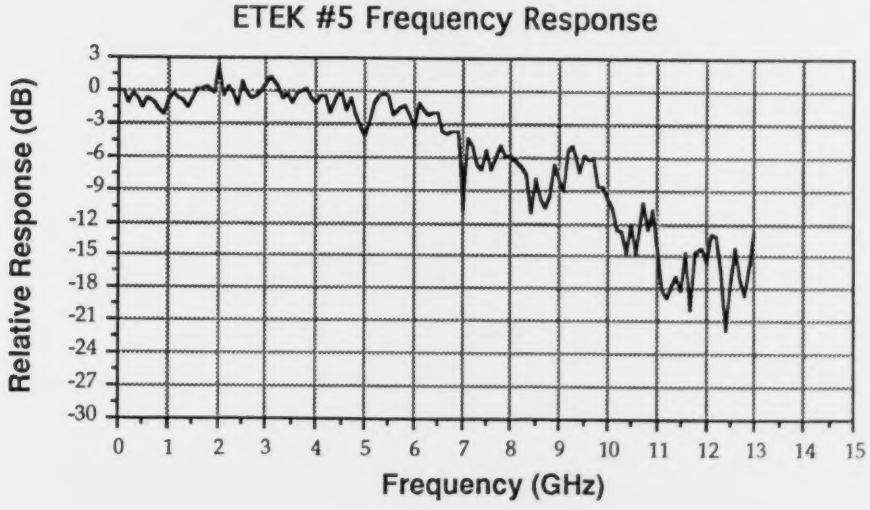

Performed By : _____ Date : _____

Appendix 5A : Erbium-Doped Fiber Amplifier Configurations

The optical time-division multiplexing experiments and the polarization multiplexing experiments used three common erbium-doped fiber amplifier configurations. The three configurations are shown below in figure 5A.1. Table 5A.1 lists the optical bandpass filters and their insertion loss and bandwidth figures. Table 5A.2 describes the erbium-doped fiber amplifiers and lists the operating parameters and resulting small signal gains.

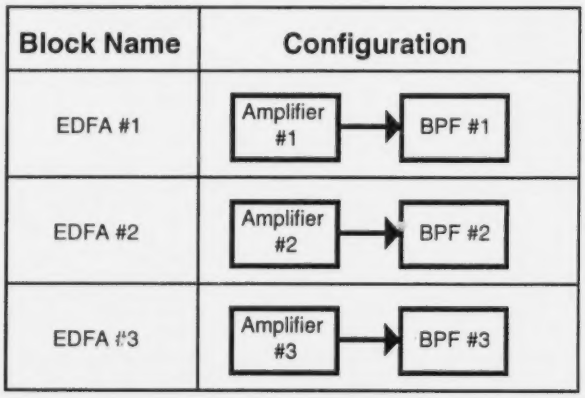

Figure 5A.1 : Optical Amplifier Configurations

Filter	Model #	Tuning Range (nm)	Insertion Loss (dB) at 1551 nm	Filter Bandwidth (nm) at 1551 nm
BPF #1	TB1570	1520-1570	2.0	2.9
BPF #2	TB1550B	1530-1560	2.9	1.4
BPF #3	TB1550B	1530-1560	2.5	1.4

Table 5A.1 : Optical Bandpass Filter Parameters

Amplifier	Fiber Type/ Length	Pump Current (mA)	Pump Power (mW)	Small Signal Gain (dB) at 1551nm	Gain (dB) Including BPF Loss
#1	NOI-3 / 22m	185	15	14.1	12.1
#2	NOI-4 / 66m	185	15	12.2	9.3
#3	NOI-4 / 60m	160	40	21.5	19.0

Table 5A.2 : EDFA Operating Conditions

Appendix 5B : Polarization Multiplexing Transmission Experiments - Bit Error Rate Curves

This appendix includes the bit error rate curves measured during the polarization multiplexing transmission experiments. Figures 5B.1 to 5B.5 compare the 1 channel and 3 channel polarization multiplexing bit error rate curves measured at the 0, 25, 50, 75, and 100 km transmission distances.

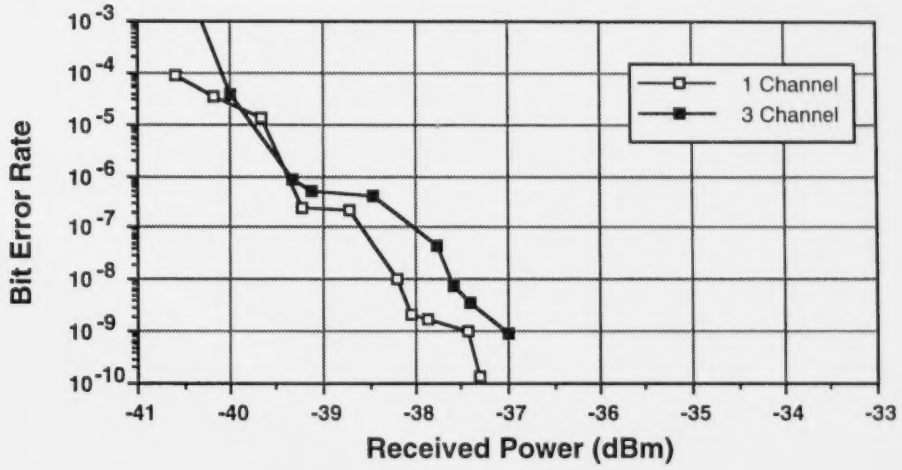

Figure 5B.1 : Bit Error Rates for 0 km Transmission

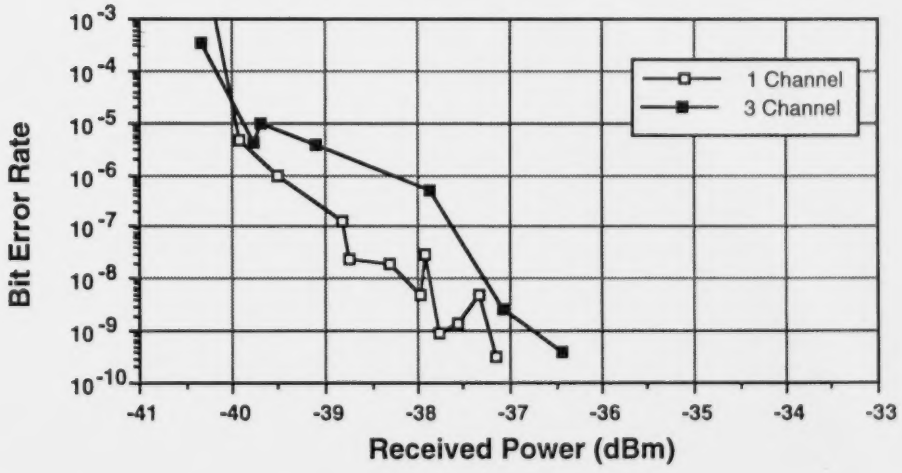

Figure 5B.2 : Bit Error Rates for 25 km Transmission

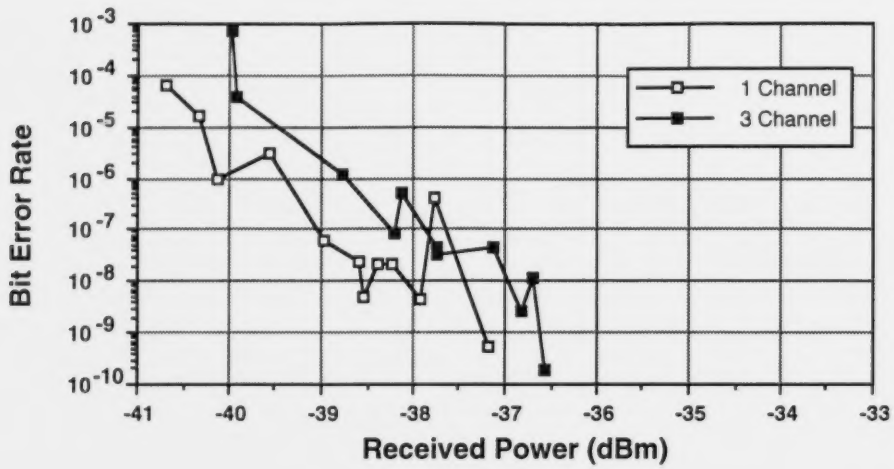

Figure 5B.3 : Bit Error Rates for 50 km Transmission

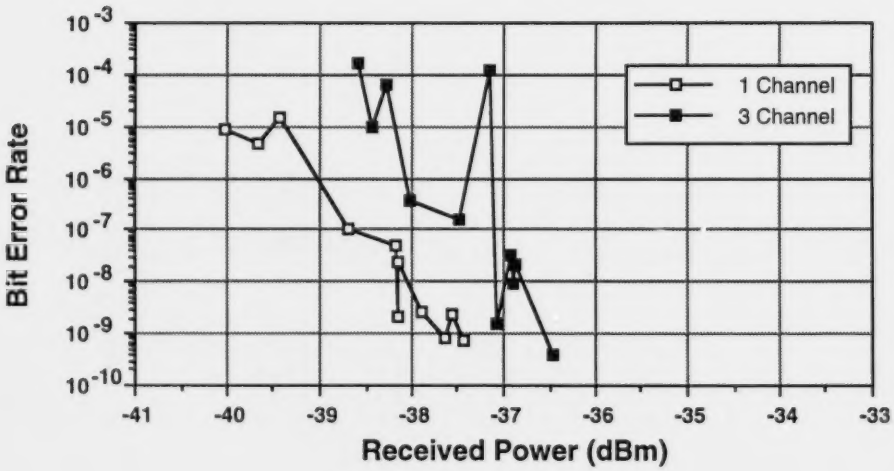

Figure 5B.4 : Bit Error Rates for 75 km Transmission

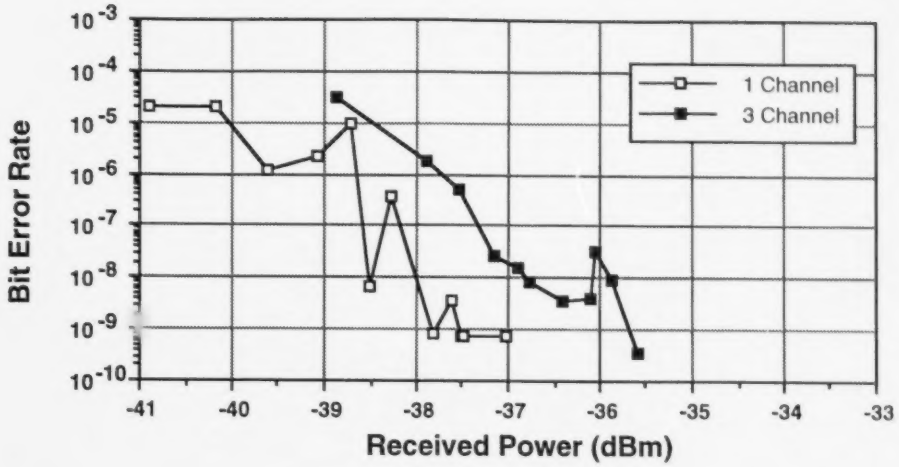

Figure 5B.5 : Bit Error Rates for 100 km Transmission